EGG-TMI-6853-PT I
~~Part 1~~
DRAFT

Copy 2

DRAFT REPORT: TMI-2 CORE DEBRIS GRAB SAMPLES--EXAMINATION AND ANALYSIS

INL Technical Library
401288

Douglas W. Akers
Eric R. Carlson
Beverly A. Cook
Scott A. Ploger
Johan O. Carlson

Idaho National Engineering Laboratory
Operated by the U.S. Department of Energy

Informal Report

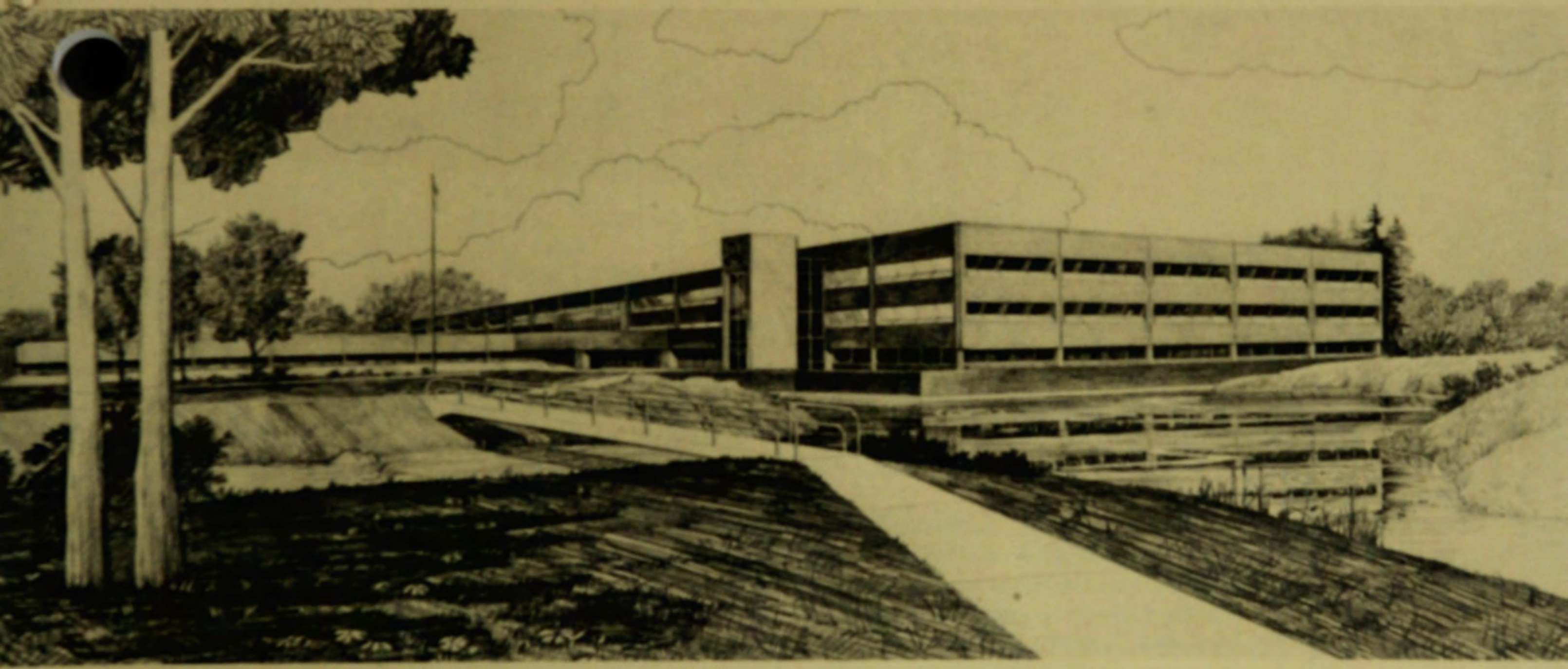

Prepared for the
U.S. DEPARTMENT OF ENERGY
Under DOE Contract No. DE-AC07-76ID01570

EG&G Idaho

DISCLAIMER

This book was prepared as an account of work sponsored by an agency of the United States Government. Neither the United States Government nor any agency thereof, nor any of their employees, makes any warranty, express or implied, or assumes any legal liability or responsibility for the accuracy, completeness, or usefulness of any information, apparatus, product or process disclosed, or represents that its use would not infringe privately owned rights. References herein to any specific commercial product, process, or service by trade name, trademark, manufacturer, or otherwise, does not necessarily constitute or imply its endorsement, recommendation, or favoring by the United States Government or any agency thereof. The views and opinions of authors expressed herein do not necessarily state or reflect those of the United States Government or any agency thereof.

4c1288

EGG-TMI-6853
DRAFT

DRAFT REPORT: TMI-2 CORE DEBRIS GRAB SAMPLES--EXAMINATION AND ANALYSIS

PART 1

Douglas W. Akers
Eric R. Carlson
Beverly A. Cook
Scott A. Ploger
Johan O. Carlson

Published July 1985

EG&G Idaho, Inc.
Idaho Falls, Idaho 83415

Prepared for the
U.S. Department of Energy
Idaho Operations Office
Under DOE Contract No. DE-AC07-76ID01570

ABSTRACT

Six samples of particulate debris were removed from the TMI-2 core rubble bed during September and October 1983, and five more samples were obtained in March 1984. The samples (up to 33 cm^3 each) were obtained at two locations in the core: H8 (center) and E9 (mid-radius). Ten of the eleven samples were examined at the Idaho National Engineering Laboratory to obtain data on the physical and chemical nature of the debris and the postaccident condition of the core. Portions of the samples also were subjected to differential thermal analysis at Rockwell Hanford Operations and metallurgical and chemical examinations at Argonne National Laboratories. This report presents results of the examination of the core debris grab samples, including physical, metallurgical, chemical, and radiochemical analyses. The results indicate that temperatures in the core reached at least 3100 K during the TMI-2 accident, fuel melting and significant mixing of core structural material occurred, and large fractions of some radionuclides (e.g., >90% of the ^{144}Ce) were retained in the core.

SUMMARY

Examinations are being performed to acquire data on the extent and nature of damage to the Three Mile Island Unit 2 (TMI-2) reactor, which underwent a loss-of-coolant accident in March 1979. One of the examination tasks is to analyze samples of debris obtained from the rubble bed.

Figure S-1 shows the current condition of the core, as determined from closed-circuit television, core topography, and rubble bed probing examinations. It is estimated that the debris bed consists of approximately 20% of the original core mass, and is supported by a hard crust. Approximately 65% of the core is located between the debris bed and the elliptical flow distributor, and approximately 10 to 20% has relocated to below the flow distributor.

Eleven core debris grab samples were obtained from two fuel assembly locations, H8 (center) and E9 (mid-radius). One sample was examined at the Babcock & Wilcox Lynchburg Research Center, and ten samples were examined at the Idaho National Engineering Laboratory (INEL). Of the ten samples examined at INEL, fragmented chips from seven particles were examined by Rockwell Hanford Operations using differential thermal analysis and 22 particles were shipped to Argonne National Laboratories (West and East) for metallurgical and chemical analyses.

The primary objectives of examining the core debris grab samples include the following:

- Supporting the plant recovery effort being performed by GPU Nuclear

- Determining the physical, chemical, and radiochemical condition of the core debris bed

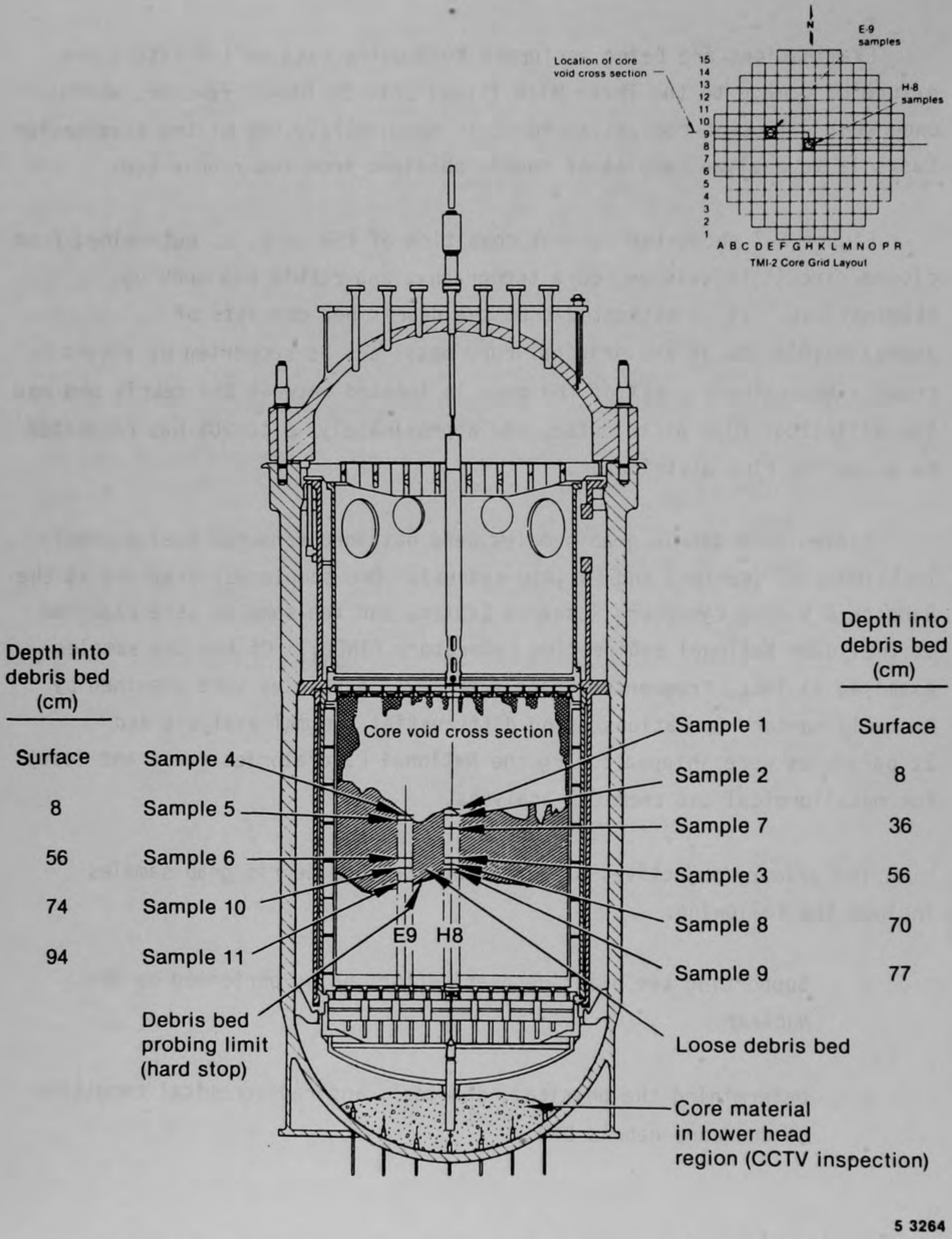
N
E-9 samples
Location of core void cross section
H-8 samples
15
14
13
12
11
10
9
8
7
6
5
4
3
2
1
A B C D E F G H K L M N O P R
TMI-2 Core Grid Layout
Depth into debris bed (cm)
Surface
8
56
74
94
Sample 4
Sample 5
Sample 6
Sample 10
Sample 11
Debris bed probing limit (hard stop)
Core void cross section
E9
H8
Sample 1
Sample 2
Sample 7
Sample 3
Sample 8
Sample 9
Loose debris bed
Core material in lower head region (CCTV inspection)
Depth into debris bed (cm)
Surface
8
36
56
70
77
5 3264

Figure S-1. Schematic showing the current known condition of the TMI-2 core and the locations of the core debris grab samples.

- Providing data to support assessment of severe fuel damage codes, primarily with regard to core damage progression and fission product behavior.

This report presents the results and conclusions of analysis of the core debris grab samples, including: (a) the sample acquisition, examination plan, and analytical methods; (b) examination results (physical, metallurgical, chemical, and radiochemical); (c) an evaluation of the overall core condition and radionuclide behavior, using information from the core debris and other available examination results; and (d) principal observations and conclusions obtained from these examinations.

Sample Acquisition, Examination Plan, and Analytical Methods

The core debris grab samples were removed from the debris bed at depths ranging from the surface to 77 cm at the H8 location, and from the surface to 94 cm at the E9 location. A hard stop was encountered at 77 cm at the H8 location, and friction prevented penetration of the debris bed beyond 94 cm at E9 . Sample weights obtained ranged from 17 g (Sample 4) to 174 g (Sample 10).

Figure S-2 is a flow diagram showing the examinations performed on the core debris grab samples. There were four general types of materials examined: (a) bulk samples, as received from TMI-2; (b) particle size fractions--subgroupings of the bulk samples by size, obtained by sieving the bulk samples, (c) recombined bulk samples--approximately one-third of each particle size fraction, recombined to approximate the original bulk sample; and (d) particles and aliquots--individual particles from the larger (>1000 μm) particle size fractions and aliquots [representative portions from the smaller (<1000 μm) particle size fractions]. Analytical methods used for the examinations are standard examination techniques, with some modifications necessitated by the high radiation fields and insoluble nature of the core debris.

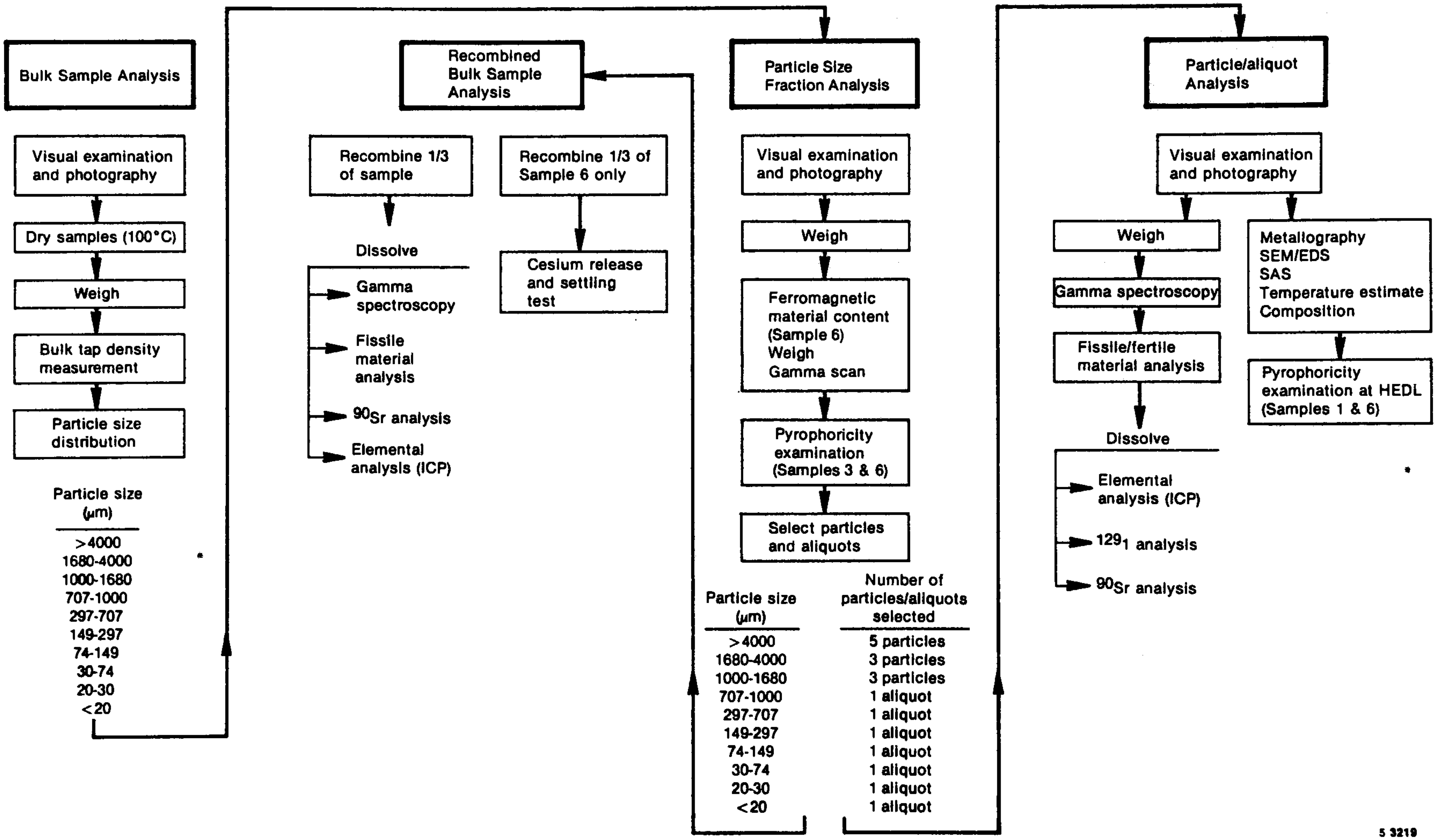
Bulk Sample Analysis
Visual examination and photography
Dry samples (100°C)
Weigh
Bulk tap density measurement
Particle size distribution
Particle size (μm)
>4000
1680-4000
1000-1680
707-1000
297-707
149-297
74-149
30-74
20-30
<20
Recombined Bulk Sample Analysis
Recombine 1/3 of sample
Dissolve
Gamma spectroscopy
Fissile material analysis
90Sr analysis
Elemental analysis (ICP)
Recombine 1/3 of Sample 6 only
Cesium release and settling test
Particle Size Fraction Analysis
Visual examination and photography
Weigh
Ferromagnetic material content (Sample 6)
Weigh
Gamma scan
Pyrophoricity examination (Samples 3 & 6)
Select particles and aliquots
Particle size (μm)
Number of particles/aliquots selected
>4000 5 particles
1680-4000 3 particles
1000-1680 3 particles
707-1000 1 aliquot
297-707 1 aliquot
149-297 1 aliquot
74-149 1 aliquot
30-74 1 aliquot
20-30 1 aliquot
<20 1 aliquot
Particle/aliquot Analysis
Visual examination and photography
Weigh
Gamma spectroscopy
Fissile/fertile material analysis
Dissolve
Elemental analysis (ICP)
129I analysis
90Sr analysis
Metallography
SEM/EDS
SAS
Temperature estimate
Composition
Pyrophoricity examination at HEDL (Samples 1 & 6)
5 3219

Figure S-2. Flow diagram showing the examinations performed on the TMI-2 core debris grab samples (typical for each sample).

Physical Examinations

The physical examinations included visual and photographic examinations, weighing, bulk tap density measurements, particle size distribution analysis, and ferromagnetic and pyrophoricity tests. In general, the core debris was composed of particulate material that was not identifiable as core components. Five (types) categories of particles were identified based on visual appearance: (a) obvious fuel pieces; (b) cladding chunks, (c) foamy/porous, prior molten material; (d) particles that are a composite of fuel and prior molten material; and (e) metallic appearing, prior molten particles.

Bulk tap density measurements indicate that there are two density ranges for the samples. Samples 1, 3, and 6 have densities ranging from 3.5 to 3.8 g/cm^3 whereas Samples 9, 10, and 11 have densities ranging from 5.0 to 5.5 g/cm^3. The particle size distribution analysis indicated that Samples 1 and 3 have the largest fraction of material in the 1680 to 4000-μm particle size range, whereas Samples 9, 10, and 11 show a bimodal distribution, with peaks at the 1680 to 4000-μm and 297 to 707-μm sizes. The biomodal distribution probably resulted in more efficient packing of the debris material and may explain the higher densities of Samples 9, 10, and 11. The particle size distribution analysis indicates the presence of mostly (>80%) larger particles (>1000 μm). Stratification of the debris bed into two layers also is indicated by the particle size distribution: a surface layer, and another beginning between 36 cm and 56 cm below the debris bed surface. The lower layer contains larger quantities of smaller sized particles. The measurable ferromagnetic material content of Sample 6, the only sample analyzed for ferromagnetic content, was 0.9% of the total sample weight.

Metallurgical Examinations

Twenty-nine particles were selected from the ten core debris grab samples for detailed metallurgical analysis, which included optical and scanning electron microscopy for microstructural information and energy dispersive x-ray spectroscopy and scanning Auger spectroscopy for information on elemental composition.

Most of the particles examined contained regions of prior molten U-Zr-O, indicating peak temperatures of greater than 2200 K. Of these, many are prior molten $(U,Zr)O_2$, indicating peak temperatures greater than 2800 K. There are a few examples of prior molten material that are almost pure UO_2, indicating temperatures up to 3100 K (the effect of small amounts of impurities on the melting point of UO_2 is not well known). However, much of the fuel probably remained at fairly low temperatures (<2000 K) relative to the peak temperature or was exposed to high temperatures for only a short time. This conclusion is based on the relatively unrestructured appearance observed for much of the fuel, even though there are attached regions of prior molten ceramics.

The regions of prior molten U-Zr-O usually contain at least some traces of non-fuel rod materials (Al, Cr, Fe, and Ni). These elements often were observed at grain boundaries or in voids. For some particles, they are a significant portion of the total particle weight. Control rod materials (Ag, In, and Cd) were not as commonly found as structural materials. There are only a few instances of control rod materials mixed in with fuel rod materials. However, major portions of three particles are metallic Ag containing Ni-SN inclusions, indicating that control rod materials (or at least Ag) apparently had less of a tendency to mix or interact with fuel rod materials than did the structural materials.

Chemical Examinations

Elemental analysis of the core debris grab samples was performed by inductively coupled plasma spectroscopy (ICP) on the recombined bulk samples and the individual particles and aliquots. Elements for which analyses were performed were selected to characterize five groups of core components: (a) uranium fuel and zircaloy cladding, (b) Ag-In-Cd control rod materials, (c) poison rod materials (B, Gd, and Al), (d) structural materials (stainless steel and Inconel) and (e) elemental Te.

Most elemental constituents of the core components were present in all recombined bulk samples, particles, and aliquots, suggesting that significant disruption, mixing, and relocation of these components has occurred. The analyses for U and Zr indicate that significant depletion ($\leq$50%) of Zr from the debris bed has occurred. Analyses for control rod materials with emphasis on Ag indicate that as much as 90% of the Ag has relocated from the debris bed. There appears to be a general increase in Ag concentration associated with a decrease in particle size. The burnable poison materials, Al and Gd, were measured in most of the samples. The wide distribution of Gd is of particular interest, because only four fuel assemblies in the core contained Gd control material (13 kg). These fuel assemblies were located at four quadrants, about mid-radius in the core.

Al, a relatively volatile core constituent, is concentrated at the surface of the debris bed, suggesting that the debris bed may have functioned as a trap or retention zone for some core materials. Structural materials are well mixed in the debris bed in concentrations similar to their original concentrations in the fueled portion of a fuel assembly. Elemental Te, which may originate from natural or fission product sources is concentrated near the surface of the debris bed similar to aluminum.

Radiochemical Examinations

Radiochemical examinations were performed on the recombined bulk samples, particles and aliquots from all samples, and the ferromagnetic components of Sample 6. The examinations included gamma spectroscopy, fissile/fertile material (^{235}U/^{238}U) content, and, ^{129}I and ^{90}Sr analyses. Examinations were performed to characterize radionuclides of expected high volatility (^{129}I and ^{137}Cs), intermediate volatility (^{106}Ru and ^{125}Sb) and low volatility (^{90}Sr and ^{144}Ce).

Comparison of the measured to predicted retention/release of these radionuclides in the core debris is shown in Table S-1 and approximately follows the expected volatility of the radionuclides (i.e., the most volatile materials, ^{129}I, and ^{137}Cs, were most significantly

TABLE S-1. RADIONUCLIDE RETENTION NORMALIZED TO URANIUM CONTENT (% of core inventory)

Radionuclide	Calculated Core Average Concentration[a] (Ci/g)	H8 Samples Measured Average Retention[b]	H8 Samples Range[c]	E9 Samples Measured Average Retention[b]	E9 Samples Range[c]
^{90}Sr	8.12E-3	94	91-102	92	79-100
^{106}Ru	1.41E-3	49	35-74	63	52-86
^{125}Sb	4.53E-4	28	19-37	28	18-38
^{129}I	2.81E-9	24[d]	19-28	19[d]	10-25
^{137}Cs	9.32E-3	19	18-21	24	6-32
^{144}Ce	3.37E-3	121	114-128	107	90-130
$^{235}U/U$[e]	--	2.5	2.3-2.7	2.7	2.5-2.8

---

a. Calculated based on ORIGEN-2 analyses.

b. Average measured retention for all samples.

c. Range of retention for recombined bulk samples.

d. Calculated based on particle and aliquot analyses. Uncertainty is ∿100%.

e. Uranium enrichment calculated from fissile and total U analyses.

released). The ^{144}Ce concentrations in the samples are greater than would be expected based on U content. The high concentrations may be due to either the presence of a localized zone of high burnup fuel or volatility of cerium. The debris bed may be a zone where this radionuclide has accumulated. The ^{129}I content of the samples tends to correlate with surface area for the small particle sizes and may indicate transport by a vaporization/condensation mechanism. Also, a correlation was observed between the concentrations of Ni and the ^{125}Sb and ^{106}Ru concentrations, suggesting that Ni functioned as a scavenging material for these radionuclides in the debris.

Contributions to Understanding the TMI Accident

This section describes how the results from the examination of the core debris grab samples contribute to understanding the condition of the TMI-2 core and accident scenario.

Metallurgical analysis of the large particles from the core debris grab samples indicate that peak temperatures up to the melting point of the UO_2 fuel were achieved, with an estimated average debris peak temperature of about 2200 K. There are indications of either a prolonged candling sequence or multiple temperature excursions. Evidence of movement of molten material down the fuel-cladding gap was observed, and there is some evidence of strong interaction of the fuel materials.

Evaluations were performed to estimate the degree of mixing, physical relocation, and segregation of core materials. The examination results suggest that the molten core debris was mixed vigorously for a significant period of time to produce the degree of mixing and homogenity observed. The mixing probably occurred during the formation of the debris bed, which probably resulted from the quench upon reflooding with the 'B' pump between 174 and 180 min.

Evidence of physical relocation and mixing of the fuel assembly materials was obtained by comparing the original U enrichments of the H8 and E9 fuel assemblies with the measured enrichments of samples removed from these locations. No correlation exists between the original and measured enrichments, indicating significant physical relocation of fuel at the H8 and E9 locations occurred.

There is evidence of significant relocation and segregation of some nonfuel core materials (Zr, Ag, In, Cd, Gd, and Al). The contributions of these material movements on understanding the core condition and accident scenario are:

- The unexamined portion of the core may have zones of heterogeneous material composition with significantly different compositions than the debris bed samples.
- Accumulations of Al and Te at the surface of the debris bed the suggest that the surface of the debris bed functioned as a trap for some of the highly volatile structural materials. The results also suggest that the debris bed has been stationary since the accident.
- The concentrations of Ag tend to be higher for the smaller (<1000 μm) particle size fractions, possibly because of the increased surface area for condensation on the particles with decreasing particle size. These data suggest either a vaporization/condensation or a vaporization/chemical reaction transport mechanism.

Figure S-3 shows the average retention of radionuclides in the debris samples as percentages of the predicted concentrations contained in a gram of U. Also shown is the transport of radionuclides from the fuel to other core components (cladding, structural material, etc.) and to the exvessel portion of the reactor coolant system. Release of radionuclides from the fuel is in the order of expected volatilities of the radionuclides (^{129}I,

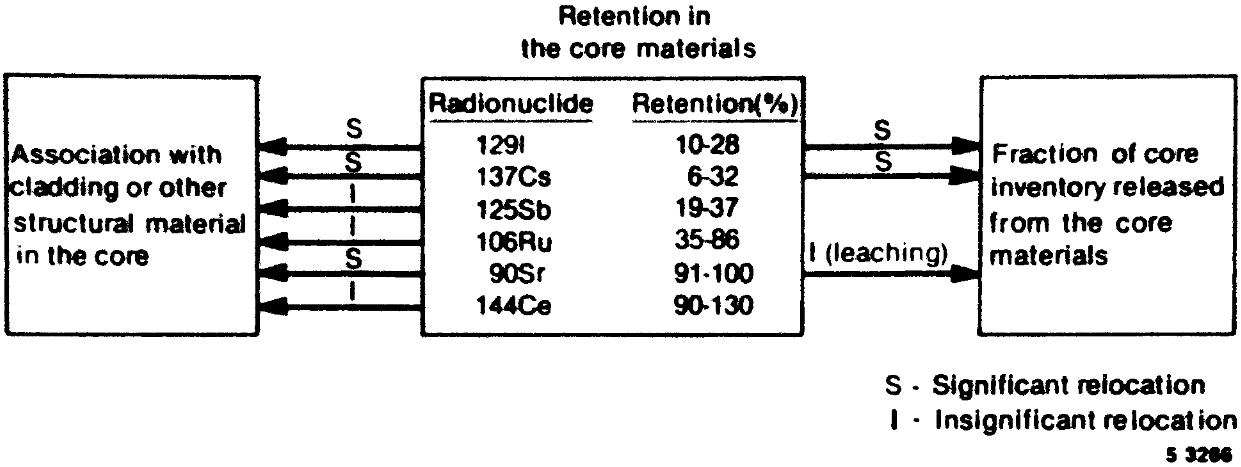
Retention in
the core materials
Radionuclide
Retention(%)
129I
10-28
137Cs
6-32
125Sb
19-37
106Ru
35-86
90Sr
91-100
144Ce
90-130
Association with cladding or other structural material in the core
S
S
I
I
S
I
S
S
I (leaching)
Fraction of core inventory released from the core materials
S - Significant relocation
I - Insignificant relocation
5 3286

Figure S-3. Schematic showing the behavior (retention/relocation) of various radionuclides in the TMI-2 core.

^{137}Cs, ^{125}Sb, ^{90}Sr, ^{106}Ru, and ^{144}Ce), with the exceptions of ^{125}Sb, ^{90}Sr, and ^{106}Ru. The retention of ^{125}Sb in the core debris grab samples is less than expected and is similar to ^{137}Cs. No significant fraction of the core inventory of ^{125}Sb has been measured outside the core region and these data suggest that a large fraction of the core inventory of this radionuclide may have been transported to lower regions in the core. The suggested mechanism for this transport is by reaction with structural materials which were transported out of the debris bed. Significant scavenging of ^{125}Sb by structural Ni was observed for several particles.

^{90}Sr was retained to a greater extent and ^{106}Ru to a lesser extent than was expected, based on the volatility of the elements. The greater ^{90}Sr retention in the samples may be attributable to the formation of SrO, a highly involatile oxide of Sr. The greater release of ^{106}Ru may be attributed to the formation of highly volatile and quite unstable oxides, RuO_2 and RuO_4.

As shown in Figure S-3, some radionuclides exhibit mobility from the fuel to other core materials and to the remainder of the reactor coolant system. Significant fractions of the core inventories of ^{137}Cs and ^{129}I have been measured outside the reactor core. Transport or retention mechanisms for ^{125}Sb, ^{90}Sr, and ^{106}Ru are discussed above. The transport of ^{144}Ce from the fuel to structural materials is important, because this radionuclide is expected to be strongly retained in the fuel. A suggested mechanism for the transport of this radionuclide from the fuel is the formation of CeO, a relatively volatile oxide of Ce. However, formation of this compound requires that Ce_2O_3 is reduced and would suggest that periods of oxidizing and reducing atmospheres occurred during the accident. Reducing atmospheres may have occurred during periods of no coolant or in isolated portions of the core during secondary temperature ramps.

The data obtained from analysis of the core debris grab samples suggest that the condition of the lower regions of the core might be significantly different than that observed in the debris bed. The data also suggest that radionuclides might be present as accumulations or that there may be depleted regions lower in the core.

ACKNOWLEDGMENTS

Many people contributed to the analysis of the core debris grab samples. Special thanks go to the following individuals: Roger H. Wilhelmsen and Alan W. Marley for assisting in the analysis work; Robert J. Gehrke and the staff at the Radiation Measurement Laboratory for their timely gamma spectroscopy analysis of the samples; Yale D. Harker and Paul R. Napper for developing the fast neutron flux measurement facility and performing the fissile/fertile material analysis; Joseph E. Stoyack and Michael Benton for their assistance in conducting the metallography; Daniel A. Pavlica and Theodore R. Lyon of Westinghouse Idaho Nuclear Company, Inc. for performing inductively coupled plasma, Auger, and energy dispersive x-ray spectroscopy measurements and scanning electron microscopy (SEM) examinations on particles from the first group of grab samples; Bertil G. Carlson of Argonne National Laboratory-West for performing optical metallography and John Sanecki of Argonne National Laboratory-East (ANL-E) for performing SEM/EDS and SAS examinations on 22 particles from the two groups of grab samples; Greg R. Eidam of GPU Nuclear for his contribution to the particle size evaluations; Dr. Peter Hofmann of KfK in the Federal Republic of Germany, Bob Strain and Larry Neimark of ANL-E, George Hayner of B&W, and M. L. Picklesimer for their invaluable, indepth review and analysis of the metallography results; Richard R. Hobbins for his assistance in analyzing the data and reviewing the manuscript; Yoshiaki Izumoji for Appendix G; Takeshi Yamahara for technical review; and Angela K. Richardson for assistance in organizing Appendix C.

CONTENTS

ABSTRACT ii

SUMMARY iii

ACKNOWLEDGMENTS xv

NOMENCLATURE, ACRONYMS, AND ABBREVIATIONS xxiii

1. INTRODUCTION 1

2. SAMPLE ACQUISITION, EXAMINATION PLAN, AND ANALYTICAL METHODS 5

  2.1 Sample Acquisition 5

  2.2 Examination Plan 11

    2.2.1 Objectives 11
    2.2.2 Examination Plan 12

  2.3 Analytical Methods 13

    2.3.1 Physical Examinations 16
    2.3.2 Metallurgical Examinations 17
    2.3.3 Chemical and Radiochemical Examinations 18

3. EXAMINATION RESULTS 22

  3.1 Physical Analyses 23

    3.1.1 Visual and Photographic Examinations and Weights of Bulk Samples 24
    3.1.2 Bulk Tap Density 24
    3.1.3 Particle Size Distribution 27
    3.1.4 Weight Frequency Distribution 32
    3.1.5 Particle Types 36
    3.1.6 Ferromagnetic Material Content 42
    3.1.7 Pyrophoricity Study 42

  3.2 Metallurgical Analyses 44

    3.2.1 Summary of Examinations 45
    3.2.2 Temperature Estimates 45
    3.2.3 Interactions of Fuel Rod and Non-Fuel Rod Materials 76

  3.3 Chemical Analyses 80

    3.3.1 Summary of Examinations 82
    3.3.2 Chemical Composition of the Core Debris 85

3.4 Radiochemical Analyses 98

3.4.1 Summary of Results 99
3.4.2 Radionuclide Composition of the Core Debris 103
3.4.3 Comparison with ORIGEN-2 Predicted Radionuclide Concentrations 109
3.4.4 Fission Product Association with Zr and Structural Materials 115
3.4.5 Evidence of Core Material Mixing 132
3.4.6 Summary of the Cesium Release and Settling Tests 132

4. CONTRIBUTIONS TO UNDERSTANDING THE TMI-2 ACCIDENT 134

4.1 Current Best Estimate of the TMI-2 Accident 134

4.2 Impact of Metallurgical Findings on Understanding the Accident Scenario 138

4.2.1 Temperature Estimates 138
4.2.2 Fuel Behavior 139

4.3 Evaluation of Core Relocation 140

4.3.1 Mixing of Core Materials 141
4.3.2 Bulk Relocaion of Fuel 142
4.3.3 Segregation of Core Materials 143

4.4 Behavior of Fission Products in the Core 146

4.4.1 Cesium and Iodine 147
4.4.2 Ruthenium 149
4.4.3 Antimony 150
4.4.4 Strontium 151
4.4.5 Cerium 152

5. OBSERVATIONS/CONCLUSIONS 153

6. REFERENCES 157

NOTE: See Part 2 of this report for Appendixes A through H.

FIGURES

S-1. Schematic showing the current known condition of the TMI-2 core and the locations of the core debris grab samples iv

S-2. Flow diagram showing the examinations performed on the TMI-2 core debris grab samples (typical for each sample) vi

S-3. Schematic showing the behavior (retention/relocation) of various radionuclides in the TMI-2 core xiii

1. Schematic showing the current known condition of the TMI-2 core, as determined by CCTV and core topography examinations and debris bed probing 2

2. Schematic showing the pre-accident fuel assembly and instrumentation arrangement of the TMI-2 reactor 6

3. Schematic showing the sampling method used to obtain the TMI-2 core debris grab samples 8

4. Locations of core debris grab samples in the TMI-2 core 9

5. Flow diagram showing the examinations performed on the TMI-2 core debris grab samples (typical for each sample) 14

6. Schematic of the pyrosulfate fusion technique used to dissolve particles and aliquots from the core debris grab samples 20

7. Plots showing the cumulative weight distribution of various core debris grab samples 29

8. Plots showing the cumulative weight distribution of various core debris grab samples and of the combined samples 30

9. Plot showing the cumulative weight distribution of each core debris grab sample as a function of depth into the debris bed at the H8 and E9 core locations 31

10. Weight frequency distributions of samples from the H8 core location 33

11. Weight frequency distributions of samples from the E9 core location 34

12. Photograph of Particle 1B (H8, surface) showing an example of a fuel piece 37

13. Photograph of Particle 6E (E9, 56 cm) showing an example of a cladding piece 38

14. Photograph of Particle 1H (H8, surface) showing an example of a foamy piece 39

15. Photograph of Particle 8C (H8, 70 cm) showing an example of a composite piece 40

16. Photograph of Particle 9G (H8, 77 cm) showing an example of a metallic piece 41

17. Plot showing the relationship between fuel pellet grain size and times at temperature 49

18. Zirconium-oxygen equilibrium phase diagram 52

19. U-Zr-O ternary phase diagrams for temperatures of 1773 and 2273 K 55

20. UO_2-ZrO_2 binary phase diagram (solidus and liquidus curves represent preliminary data) 56

21. Chemical interactions and formations of liquid phases in the UO_2-Zr system with increasing temperature 63

22. Photomacrograph of Particle 1A (H8, surface) showing melt flow between UO_2 fuel and ballooned cladding 65

23. Photomacrograph of Particle 6C (E9, 56 cm) showing interaction of fuel rod materials with Al_2O_3 66

24. Photomacrograph of Particle 7A (H8, 36 cm) showing foamy U,Zr,O melt 68

25. Photographs of Particle 10F (E9, 74 cm) showing the presence of two distinct regions: Region 1 is dense U,Zr,O melt and Region 2 is foamy U,Zr,O melt 69

26. SEM back scattered electron image of Particle 3L (H8, 56 cm) showing dendritic freezing 70

27. Photomicrographs of Particle 10A (E9, 74 cm) showing prior molten fuel 71

28. Quasi-binary α-Zr(O)/UO_2 phase diagram 72

29. Particle 6F (E9, 56 cm) shows where solidified $(U,Zr)O_2$ was contacted by a porous melt that solidified before contact by a Ni-rich melt 74

30. Particle 6D (E9, 56 cm) shows where the oxidized fuel mixture of U_4O_9 and U_5O_{13} have been reduced to UO_2 at one corner by contact with an initially metallic (U,Zr,O) melt 75

31. Uranium-oxygen phase diagram 77

32. $^{137}Cs/U$ content correlation for all particles and aliquots analyzed 120

33. $^{129}I/U$ content correlation for all particles and aliquots analyzed 121

34. Relationship between ^{129}I concentration and surface area for Samples 1, 3, and 6 122

35. $^{137}Cs/^{129}I$ content correlation for all particles and aliquots analyzed 123

36. Correlation between Ni content and ^{106}Ru for all particles and aliquots analyzed 124

37. Correlation between Ni content and ^{125}Sb for all particles and aliquots analyzed 125

38. $^{90}Sr/U$ content correlation for all particles and aliquots analyzed 126

39. $^{125}Sb/U$ content correlation for all particles and aliquots analyzed 127

40. Correlation between ^{125}Sb and ^{129}I for all particles and aliquots analyzed 128

41. $^{144}Ce/U$ content correlation for all particles and aliquots analyzed 129

42. Schematic showing the known and best estimated end-state condition of the TMI-2 core 135

43. Comparison of Al concentrations with normalized surface area 145

44. Schematic showing the behavior (retention/relocation) of various radionuclides in the TMI-2 core 148

TABLES

S-1. Radionuclide retention normalized to uranium content x

1. Sampling locations of core debris grab samples in the TMI-2 core 10

2. Examinations performed on the TMI-2 core debris grab samples 15

3. Results of visual and photographic examinations, weighing, and gross radiation survey of the ten bulk samples 25

4. Bulk tap densities of the TMI-2 core debris grab samples 26

5. Results of the particle size analysis of the TMI-2 core debris grab samples 28

6. Particle type distribution of the TMI-2 core debris grab samples 43

7. Summary of metallurgical analysis of the TMI-2 core debris grab samples 46

8. Core material composition 58

9. Peak temperature estimates for particles from the TMI-2 core debris grab samples 59

10. TMI-2 core composition by elemental weight percent 78

11. TMI-2 reactor core and control rod fuel assembly composition 81

12. Elemental content of the recombined bulk samples from the H8 core location 83

13. Elemental content of the recombined bulk samples from the E9 core location 84

14. Uranium and zirconium concentrations and ZR/U ratios for the recombined bulk samples 86

15. Uranium content of particles and aliquots from the H8 core location 88

16. Uranium content of particles and aliquots from the E9 core location 89

17. Zr/U concentration ratios of particles and aliquots from the H8 core location 90

18. Zr/U concentration ratios of particles and aliquots from the E9 core location 91

19. Structural material concentrations and ranges of the TMI-2 core debris grab samples 96

20. Tellurium concentrations of particles and aliquots from the TMI-2 core debris grab samples 97

21. Average radionuclide concentrations of the recombined bulk samples from the H8 core location 100

22. Average radionuclide concentrations of the recombined bulk samples from the E9 core location 101

23. Radionuclide concentrations of the ferromagnetic component of Sample 6 102

24. Core material volatility groups 104

25. Radionuclide retention in the TMI-2 core 111

26. Radionuclide retention normalized to uranium content 113

27. Comparison of radionuclide retention calculated by different methods 114

28. Comparison of the ferromagnetic/average radionuclide concentrations of Sample 6 116

29. Comparison of fission product concentrations associated with particles which were principally uranium or zirconium 118

30. Summary of correlations between selected radionuclides, elements, and particle surface area 119

31. Retention of ^{106}Ru and ^{125}Sb by Particles 9D and 9G 130

NOMENCLATURE

Aliquot	A representative portion of a homogeneous particle size fraction.
Bulk tap density	Density of the bulk sample obtained by placing the sample in a graduated beaker, tapping the beaker to compact the material, measuring the volume, and dividing the sample weight (g) by the volume (cm^3).
Fuel bundle	Fuel assembly without end fittings.
Particle	A piece of debris. Analysis was performed on individual particles greater than 1000 μm in size. For particles smaller than 1000 μm, analysis was performed on aliquots.
Particle size fractions	Subgroupings of the samples by particle size, resulting from the sieving operation. The particle sizes range from less than 20 to greater than 4000 μm.
Recombined bulk sample	After the particle size analysis, approximately one-third of each particle size fraction was weighed, then recombined to approximate the original sample.
Sample	All debris contained in a sampling tool, as-received from GPU Nuclear.

ACRONYMS AND ABBREVIATIONS

BSE	Backscatter electron analysis
CCTV	Closed-circuit television
EDS	Energy dispersive x-ray spectroscopy
ICP	Inductively coupled plasma spectroscopy
SAS	Scanning Auger spectroscopy
SEM	Scanning electron microscopy
Particle 1A	Example of notation used to identify the particles (Particle 1A was the first of several particles selected from Sample 1).

Sample 3 (H8, 56 cm)	Example of notation used to identify the samples and their original location in the debris bed (Sample 3 was obtained from the H8 core location, 56 cm into the debris bed).

DRAFT REPORT: TMI-2 CORE DEBRIS GRAB SAMPLES EXAMINATION AND ANALYSIS

PART 1

1. INTRODUCTION

The Unit 2 pressurized water reactor at Three Mile Island (TMI-2) underwent a prolonged loss-of-coolant accident on 28 March 1979, that resulted in severe damage to the core. As a consequence of the TMI-2 accident, numerous aspects of light water reactor safety have been questioned, and the U.S. Nuclear Regulatory Commission (NRC) has embarked on a thorough review of reactor safety issues, particularly the causes and effects of severe core damage accidents. The nuclear community acknowledges the importance of examining TMI-2 in order to understand the nature of the core damage. Immediately after the accident, four organizations with interests in both plant recovery and acquisition of accident data formally agreed to cooperate in these areas. These organizations, General Public Utilities Nuclear Corporation (GPU Nuclear--owner/operator of TMI), Electric Power Research Institute (EPRI), NRC, and the U.S. Department of Energy (DOE), collectively known as GEND, are presently involved in postaccident evaluation of TMI-2. DOE is providing a portion of the funds for reactor recovery (in those areas where accident recovery knowledge will be of generic benefit to the light water reactor industry of the United States). In addition, DOE is funding acquisition and analysis of severe accident data obtained from examining the damaged core.

The present condition of the TMI-2 core, as determined by closed-circuit television (CCTV) examination and probing of the debris bed, is illustrated in Figure 1.[1,2] Current estimates indicate that approximately 20% of the total core mass is an upper layer of rubblized debris supported by a hard crust. Approximately 65% is located between the debris bed and the elliptical flow distributor, and approximately 10 to 20% has relocated to below the flow distributor.

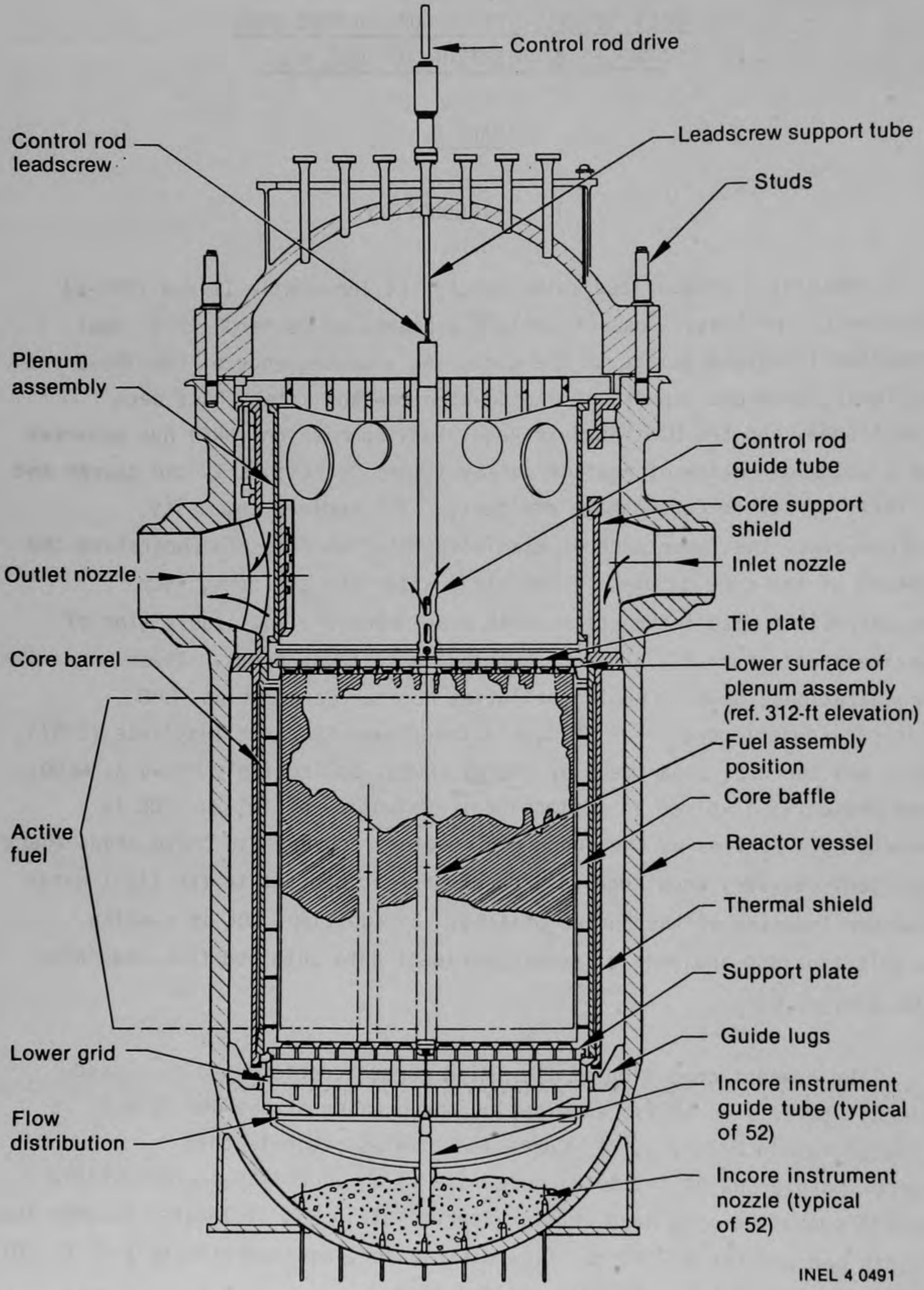
Control rod drive
Control rod leadscrew
Leadscrew support tube
Studs
Plenum assembly
Control rod guide tube
Core support shield
Outlet nozzle
Inlet nozzle
Tie plate
Core barrel
Lower surface of plenum assembly (ref. 312-ft elevation)
Fuel assembly position
Core baffle
Active fuel
Reactor vessel
Thermal shield
Support plate
Guide lugs
Lower grid
Incore instrument guide tube (typical of 52)
Flow distribution
Incore instrument nozzle (typical of 52)
INEL 4 0491

Figure 1. Schematic showing the current known condition of the TMI-2 core, as determined by CCTV and core topography examinations and debris bed probing.

The first materials obtained from the TMI-2 active fuel region were samples from the debris bed, referred to as "core debris grab samples." Six samples were obtained during September and October 1983, and five additional samples were acquired in March 1984. The eleven samples were shipped to the Idaho National Engineering Laboratory (INEL) for examination and/or distribution to other laboratories. Ten samples were retained at INEL for examination and analysis, and one sample was shipped to the Babcock & Wilcox (B&W) Lynchburg Research Center.[3] Of the ten samples retained at INEL, fragmented chips from seven particles were examined by Rockwell Hanford Operations (RHO) using differential thermal analysis and 22 particles were shipped to Argonne National Laboratories (East and West) for metallurgical and chemical analysis.[4,5]

The primary objectives of examining the core debris grab samples include the following:

- Supporting the plant recovery effort being performed by GPU Nuclear
- Determining the physical, chemical, and radiochemical condition of the core
- Providing data to support assessment of severe fuel damage codes, primarily concerning core damage progression and fission product behavior.

Results from the examination and analysis of the ten core debris grab samples retained at INEL are presented in this report. Acquisition of the samples, the examination plan, and analytical methods used in the examination are discussed in Section 2. Section 3 contains the results of the examinations, grouped into the following general categories:

- Physical Analyses - Results of the visual and photographic examinations, bulk tap density measurements, particle size distribution analysis, pyrophoricity tests, and ferromagnetic material content determination.

- Metallurgical Analyses - Analyses performed to determine visual appearance and elemental composition (on a microscale) of selected particles from the core debris materials. Estimates were made of maximum temperatures experienced during the accident. Discrete particles of debris were examined using optical metallography, scanning electron microscopy with energy dispersive x-ray spectroscopy (SEM/EDS), and scanning Auger spectroscopy (SAS).

- Chemical Analyses - Chemical analysis [e.g., inductively coupled plasma spectroscopy (ICP)] was used to measure quantitatively the elemental composition of the core debris grab samples.

- Radiochemical Analyses - Radiochemical analysis techniques, including gamma spectroscopy, neutron activation analysis, and beta emitter analysis (^{90}Sr), were used to measure the radionuclide concentrations of the core debris grab samples and provide information on fission product behavior. In addition, a leaching analysis (cesium release and settling test) was performed to determine radionuclide release caused by crushing the core materials.

Section 4 contains an fuel behavior, evaluation of the condition of the TMI-2 core with regard to temperatures, core relocation, and radionuclide behavior, based on the information presented in this study and information available from other examination activities conducted to date. Conclusions and observations resulting from the examinations are presented in Section 5.

Due to its large volume, this report has been divided into two parts. Part 1 contains the main body of the report, and Part 2 contains Appendixes A through H.

2. SAMPLE ACQUISITION, EXAMINATION PLAN, AND ANALYTICAL METHODS

This section discusses acquisition of the core debris grab samples, and describes the examination plan and analytical methods used in the examination.

2.1 Sample Acquisition

A series of CCTV inspections were made of the TMI-2 core in 1982 by inserting a miniature television camera into the upper portion of the active fuel region through leadscrew support tube and control rod guide tube openings (References 1 and 2). Three core locations (H8, E9, and B8) were chosen for initial inspection. The inspections indicated the presence of a void extending axially approximately 160 cm into the active fuel region and radially, in some areas, to the core former wall. The void space comprised approximately 25% of the original core region. Fuel assemblies were not visible in the central region of the core. Instead, there existed a bed of rubblized core material.

After the third CCTV inspection on 12 August 1982, the debris bed was probed by lowering a 1.3-cm-diameter stainless steel rod through the H8 and E9 leadscrew support tube and control rod guide tube openings. The point at which the rod touched the debris was measured. Then, the rod was rotated and allowed to penetrate the debris under its own weight (~13.5 kg). The rod penetrated easily to a depth of approximately 36 cm at both the H8 and E9 locations. The results of the probing prompted GPU Nuclear and EG&G Idaho, Inc. to obtain samples of the particulate debris from various depths. Three sampling depths were chosen: surface of the debris bed, and 8 cm and 56 cm into the bed. The H8 and E9 core locations and pre-accident locations of the control assemblies, burnable poison assemblies, and in-core instrumentation are shown in Figure 2.

Two different sampling devices were designed and fabricated to extract material from the debris bed. A clamshell type tool was used to obtain samples from the surface of the debris bed, and a rotating tube device was

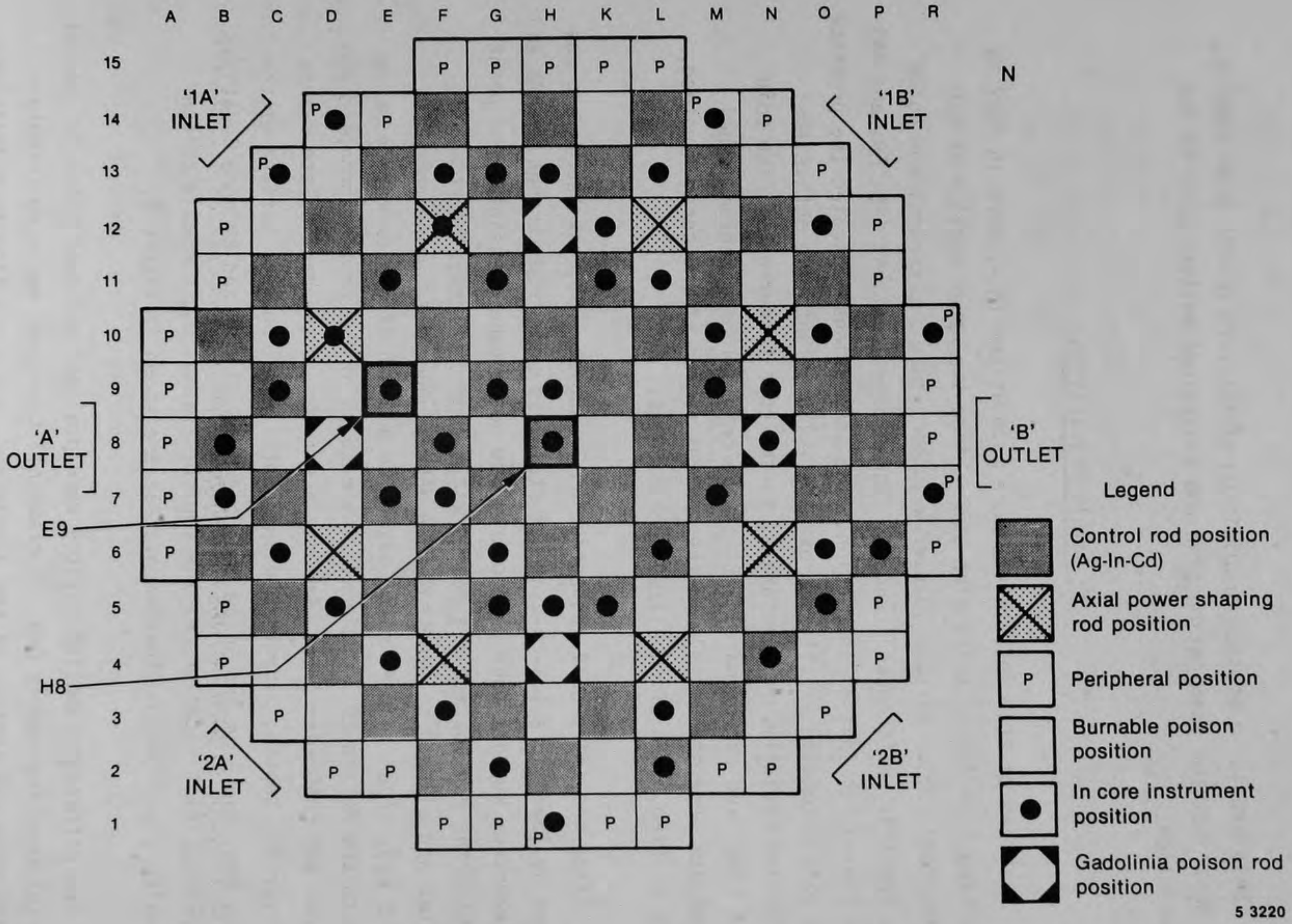
A B C D E F G H K L M N O P R
15 14 13 12 11 10 9 8 7 6 5 4 3 2 1
N
'1A' INLET
'1B' INLET
'A' OUTLET
'B' OUTLET
'2A' INLET
'2B' INLET
E9
H8
Legend
Control rod position (Ag-In-Cd)
Axial power shaping rod position
Peripheral position
Burnable poison position
In core instrument position
Gadolinia poison rod position
5 3220

Figure 2. Schematic showing the pre-accident fuel assembly and instrumentation arrangement of the TMI-2 reactor.

used to obtain the subsurface samples. Each device was designed to hold approximately 33 cm^3 of particulate debris. The sampling method and devices are illustrated in Figure 3.

The first group of six samples of particulate debris (identified as Samples 1 through 6) were obtained from the debris bed at the H8 and E9 core locations during September and October 1983. During initial probing with the sampling device, a hard stop (crust) was encountered approximately 36 cm into the debris bed at both the H8 and E9 locations. The crust was penetrated using manual force on the sampling device. [Note: A similar crust was encountered during subsequent debris bed probing at 15 other locations.] After removal, the six samples were shipped to EG&G Idaho at INEL. Subsequently, Sample 2 was shipped to the B&W Lynchburg Research Center for examination and analysis.

After acquisition of the first group of six samples, plans were made to obtain additional samples from deeper into the debris bed at the two previously sampled locations (H8 and E9). The sampling apparatus was modified to allow deeper penetration into the bed, and five samples (identified as Samples 7 through 11) were obtained in late March 1984. The maximum depth the sampling device would penetrate into the debris bed was 77 cm at the H8 location and 94 cm at E9. At the H8 (77 cm) depth, a hard stop was encountered. At the E9 (94 cm) depth, there was a friction stop encountered rather than a hard stop. The second group of five samples also was shipped to INEL for examination.

The locations of the eleven samples in the TMI-2 core[a] are shown in Figure 4. The locations of the samples, both as depth into the debris bed and distance from the bottom of the plenum assembly, given in both inches and centimeters, are listed in Table 1.

---

[a] Throughout this report, where the original location of the sample in the debris bed is pertinent to the discussion, the core location and depth of the sample in the debris bed are listed in parenthesis after the sample number [e.g., Sample 3 (H8, 56 cm)].

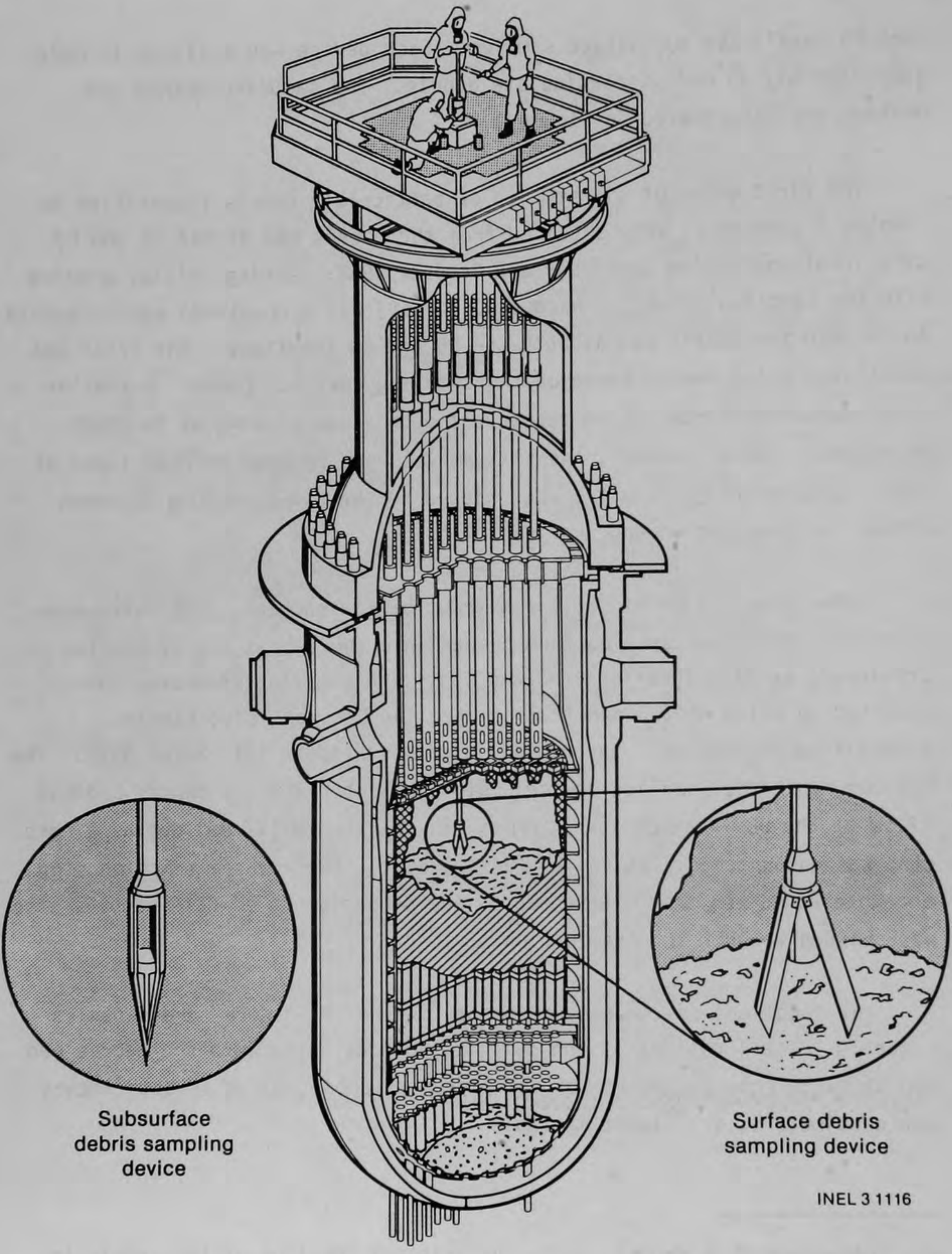
Subsurface debris sampling device
Surface debris sampling device
INEL 3 1116

Figure 3. Schematic showing the sampling method used to obtain the TMI-2 core debris grab samples.

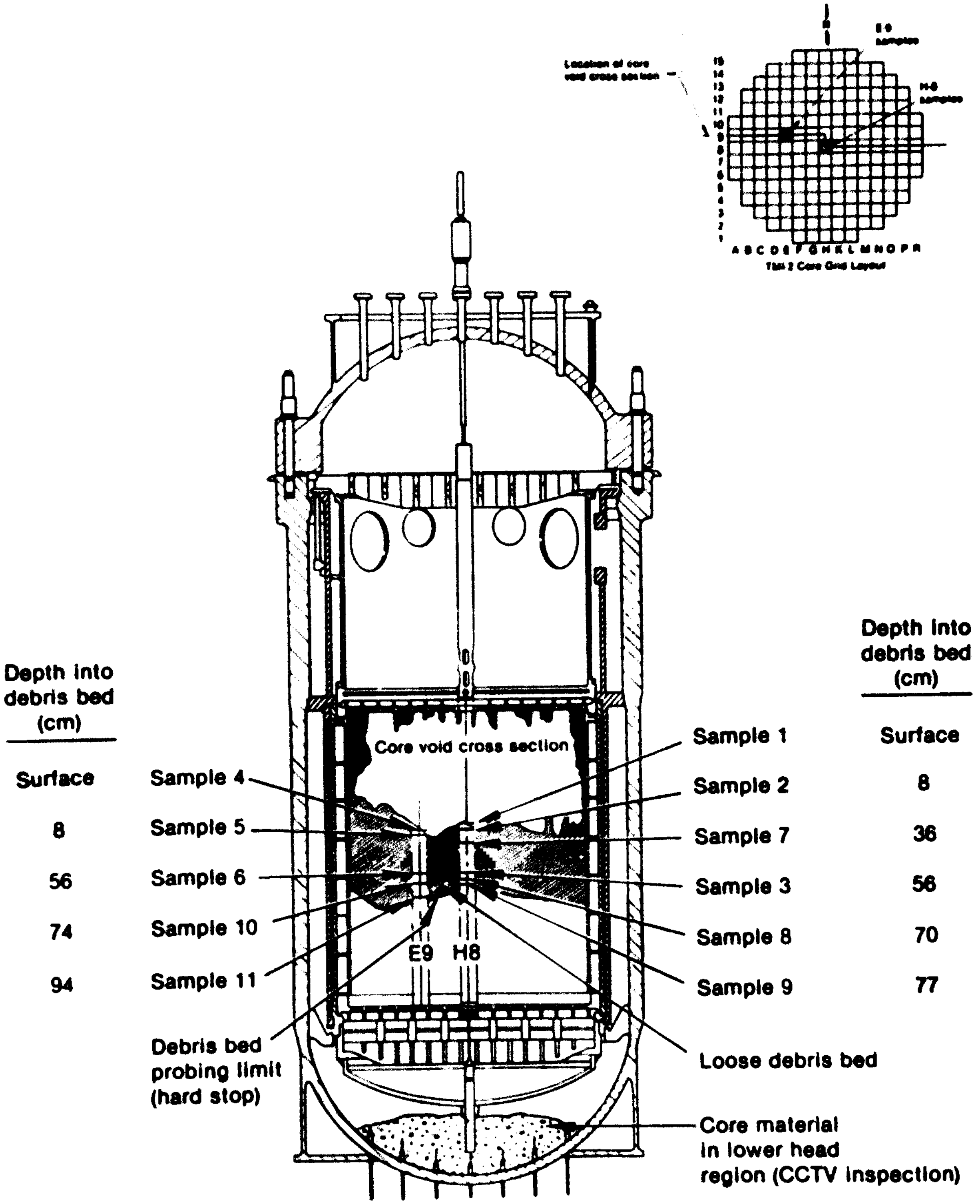
Location of core void cross section
E9 samples
H8 samples
15
14
13
12
11
10
9
8
7
6
5
4
3
2
1
A B C D E F G H K L M N O P R
TMI 2 Core Grid Layout
Depth into debris bed (cm)
Surface
8
56
74
94
Sample 4
Sample 5
Sample 6
Sample 10
Sample 11
Debris bed probing limit (hard stop)
Core void cross section
E9
H8
Sample 1
Sample 2
Sample 7
Sample 3
Sample 8
Sample 9
Loose debris bed
Core material in lower head region (CCTV inspection)
Depth into debris bed (cm)
Surface
8
36
56
70
77
5 3264

Figure 4. Locations of core debris grab samples in the TMI-2 core.

TABLE 1. SAMPLING LOCATIONS OF CORE DEBRIS GRAB SAMPLES IN THE TMI-2 CORE

Sample	Core Location	Depth into Debris Bed (in.)	Depth into Debris Bed (cm)	Distance from Bottom of Plenum Assembly[a] (in.)	Distance from Bottom of Plenum Assembly (cm)
1	H8	Surface	Surface	60	152
2	H8	3	8	63	160
3	H8	22	56	82	208
4	E9	Surface	Surface	63	160
5	E9	3	8	66	168
6	E9	22	56	85	216
7	H8	14	36	74	188
8	H8	27.5	70	87.5	222
9	H8	30.5	77	90.5	230
10	E9	29	74	92	234
11	E9	37	94	100	254

---

a. The bottom of the plenum assembly is the 312-ft reference elevation in the reactor vessel design.

2.2 Examination Plan

2.2.1 Objectives

Acquisition and examination of the core debris grab samples is one of the tasks outlined in the TMI-2 Core Examination Plan[6] which describes the technical/scientific data that should be acquired from examining the TMI-2 core. The general objectives of the examination include (a) supporting the plant recovery, (b) determining the condition of the debris bed, and (c) providing data to support assessment of severe fuel damage computer codes. Using the general objectives as a guide, an examination plan was developed which would produce data to address the following specific informational needs:

- The physical form of the core debris (particle size, shape, morphology, origin, etc.)
- Pyrophoric potential of materials present in the debris
- Chemical form and composition of the various types of particles and peak temperatures to which those materials were exposed
- Chemical form of the debris (fuel, cladding, control material, structural material, reaction product, etc.)
- Identity and quantity of fission products retained in the debris
- Present location of core materials
- Leaching rates of radionuclides from existing and freshly created surfaces
- Unanticipated defueling concerns (filtration properties, settling rates, etc.).

The information is important in planning the defueling of TMI-2. The physical form of the debris (particle size and structure) is important because small sized particles may be suspended during defueling and cause cloudiness of the water, thus obstructing operator vision. Particle size distribution data will help determine the types of filters, cyclones, etc., needed to clean the water and remove the debris during defueling. The presence of pyrophoric materials may indicate that even larger concentrations of those materials exist below the loose debris, which must be considered during defueling and shipping of the TMI-2 core debris. Characteristics of the physical state of the debris particles (e.g., presence of prior molten materials) may provide a clue as to the nature of the core material underneath the loose debris layer. The physical and mechanical properties of the core debris materials will influence the design of tools and methods for defueling. The retained fission product content of the debris also is important because it represents a potential radiological hazard that must be controlled. The rate at which radioisotopes leach from the debris will affect the level of radioactivity in the water during defueling.

Assessment of severe fuel damage codes is important in predicting overall reactor safety. Data obtained from the damaged TMI-2 core will be the most extensive full-scale data available for code benchmarking. Information on peak temperatures, fission product transport and retention, and final physical state can be compared directly with code predictions. The TMI-2 accident scenario was inferred from a combination of code calculations, analysis of core materials, evaluation of data from on-line instrumentation, and results from other severe accident research.

2.2.2 Examination Plan

The high radiation fields (up to 100 rad/h) associated with the samples necessitated analyzing only portions of the samples in some cases. Most chemical and radiochemical analysis techniques are limited to relatively low radiation fields (<400 mrad/h). It was realized that by reducing the quantity of material analyzed to attain acceptable radiation levels, the small portions might not be representative of the entire sample. Therefore, a sampling and analysis plan was developed which included analyzing entire samples, as well as small portions.

A flow diagram of the plan developed for examining the core debris grab samples is shown in Figure 5. The same information is presented in Table 2, except the examinations are organized according to the general category of examination (physical, metallurgical, chemical, and radiochemical). Each bulk sample was examined visually, photographed, dried, weighed, measured for bulk tap density, and sieved into particle size fractions (up to ten size fractions with particle diameters ranging from less than 20 to greater than 4000 μm). Individual particles were selected from the larger (>1000 μm) particle size fractions. An aliquot (a representative portion of a homogeneous particle size fraction) was removed from each smaller (<1000 μm) size fraction. The individual particles and aliquots were subjected to a variety of analyses (see Figure 5). Ferromagnetic material content examinations were performed on Sample 6, and pyrophoricity tests were performed on portions of Samples 1, 3, and 6. Approximately one-third of each particle size fraction was recombined to approximate the original bulk sample (called the "recombined bulk sample"). The recombined bulk samples were dissolved in acid solutions and analyzed to determine their average elemental and radiochemical compositions. The remainder of the particle size fractions for Sample 6 were subdivided, and a second recombined bulk sample was formed. Cesium release and settling tests were performed on this second recombined bulk sample.

2.3 Analytical Methods

This subsection summarizes the analytical methods used in examining the core debris grab samples. Brief descriptions of individual examination techniques are contained in Appendix A. The methods used for analyzing the core debris grab samples were, in most instances, standard laboratory techniques, with modifications to adapt them to the physical characteristics of the sample material and high radiation levels.

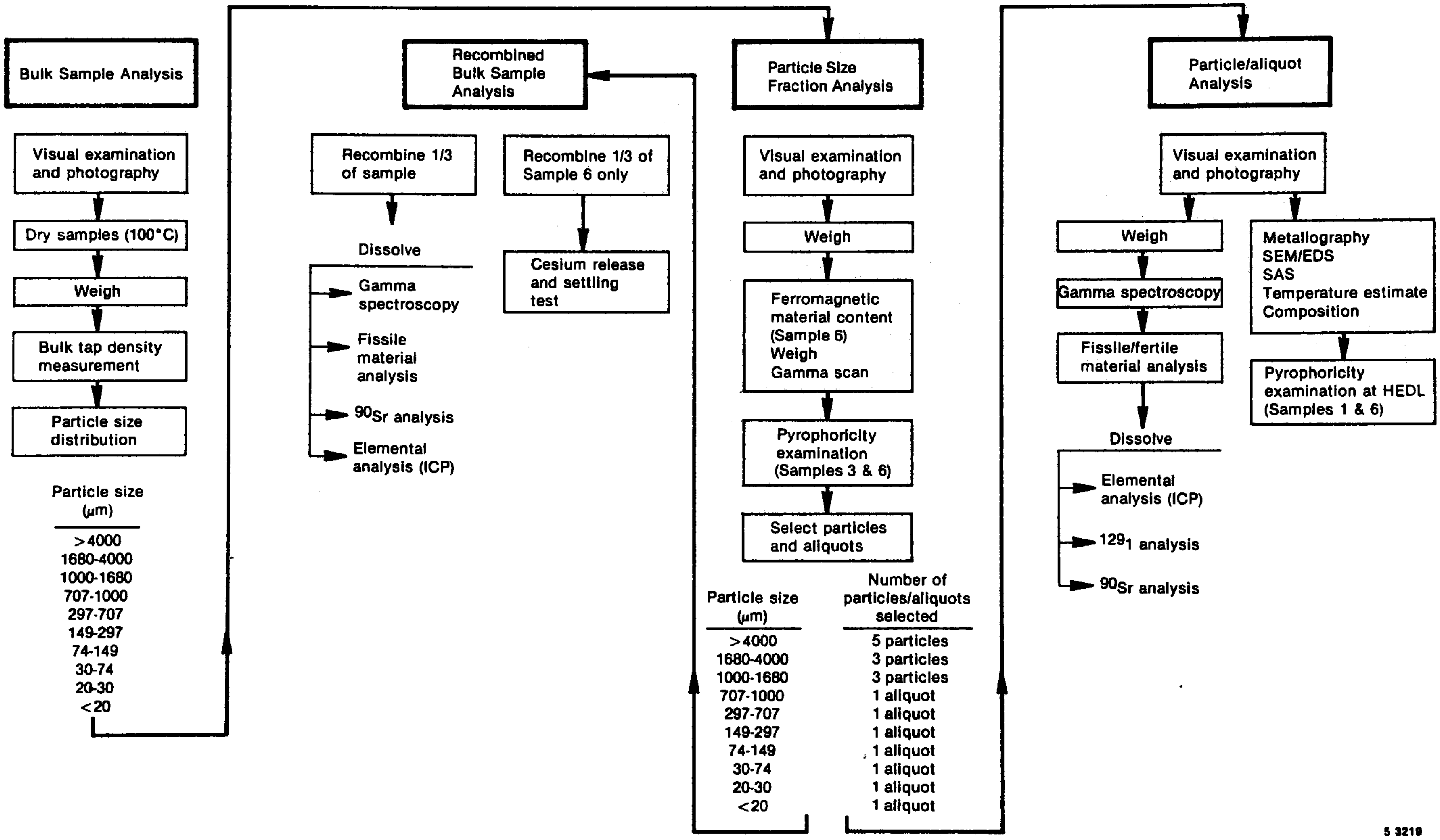
Bulk Sample Analysis
Visual examination and photography
Dry samples (100°C)
Weigh
Bulk tap density measurement
Particle size distribution
Particle size (μm)
>4000
1680-4000
1000-1680
707-1000
297-707
149-297
74-149
30-74
20-30
<20
Recombined Bulk Sample Analysis
Recombine 1/3 of sample
Dissolve
Gamma spectroscopy
Fissile material analysis
90Sr analysis
Elemental analysis (ICP)
Recombine 1/3 of Sample 6 only
Cesium release and settling test
Particle Size Fraction Analysis
Visual examination and photography
Weigh
Ferromagnetic material content (Sample 6) Weigh Gamma scan
Pyrophoricity examination (Samples 3 & 6)
Select particles and aliquots
Particle size (μm)
Number of particles/aliquots selected
>4000 5 particles
1680-4000 3 particles
1000-1680 3 particles
707-1000 1 aliquot
297-707 1 aliquot
149-297 1 aliquot
74-149 1 aliquot
30-74 1 aliquot
20-30 1 aliquot
<20 1 aliquot
Particle/aliquot Analysis
Visual examination and photography
Weigh
Gamma spectroscopy
Fissile/fertile material analysis
Dissolve
Elemental analysis (ICP)
129I analysis
90Sr analysis
Metallography SEM/EDS SAS Temperature estimate Composition
Pyrophoricity examination at HEDL (Samples 1 & 6)
5 3219

Figure 5. Flow diagram showing the examinations performed on the TMI-2 core debris grab samples (typical for each sample).

TABLE 2. EXAMINATIONS PERFORMED ON THE TMI-2 CORE DEBRIS GRAB SAMPLES

Examinations	Bulk Sample	Particles and Aliquots	Recombined[a] Bulk Sample
Physical			
Visual and photographic	X	X	--
Weight	X	X	X
Bulk tap density	X	--	--
Particle size distribution	X	--	--
Ferromagnetic material content	X	--	--
Pyrophoricity	--	X	--
Metallurgical			
Optical metallography	--	X[b]	--
Scanning electron microscopy (SEM)/ energy dispersive x-ray spectroscopy (EDS)	--	X[b]	--
Scanning Auger spectroscopy (SAS)	--	X[b]	--
Chemical			
Inductively coupled plasma spectroscopy (ICP)	--	X	X
Radiochemical			
Gamma spectroscopy	--	X	X
Neutron activation/delayed neutron analysis for fissile fertile material content	--	X	X[c]
^{129}I analysis	--	X	--
^{90}Sr analysis	--	X	X
Cesium release and settling test	--	--	X

---

a. After particle size analysis of each bulk sample, approximately one-third of each particle size fraction was weighed, then recombined to approximate the original sample. Hence the term "recombined bulk sample."

b. Metallurgical examinations were performed only on selected particles larger than 1000 µm.

c. Fertile material content analysis was not performed on the recombined bulk samples.

2.3.1 Physical Examinations

Visual and photographic examinations were performed during unpackaging and throughout the handling operations of the bulk samples and particle size fractions to determine the sizes, shapes, and types of particles in the samples. The samples were dried at 100°C and weighed. The bulk tap density of each sample was measured by placing the sample in a graduated beaker, tapping the beaker to compact the material, measuring the volume, and dividing the sample weight (g) by the volume (cm^3). The bulk tap density measurement has a relatively high (∿40%) uncertainty but is fast and easy to perform. GPU Nuclear requested this examination to obtain an approximation of the debris bed density. The bulk tap density measurements results include all uncertainties resulting from voids, uneven packing, and irregular shapes of particles. A more precise (wet) density measurement was not performed because the degree of accuracy associated with that technique was not required.

The particle size distribution was determined for each bulk sample, using a column of progressively smaller sieves. New sieves were used for each sample to prevent cross contamination. After transferring (dry) the bulk sample to the sieve column, the grab sample was agitated for several minutes to segregate it into particle size fractions according to sieve aperture size. Two of the core debris grab samples (Samples 4 and 5) were not subjected to a complete particle size analysis because they are composed principally of large (>1000 μm) particles. The sieve fractions containing large (>1000 μm) particles were transferred directly to storage containers. The smaller (<1000 μm) particle size fractions were wet sieved (using a freon wash) and transferred to storage containers. Wet sieving was performed to reduce the loss of particles by aerosol transport or adherence to sieve surfaces. Each particle size fraction was examined visually, photographed, and weighed. The ferromagnetic material in each particle size fraction of Sample 6 was removed, weighed, and gamma scanned. Pyrophoricity tests were performed at INEL on material from all particle size fractions from 30 to 4000 μm for Samples 3 and 6. RHO also performed differential thermal analysis tests on fragmented chips from seven particles from Samples 1 and 6. The particle sizing, ferromagnetic determination, and pyrophoricity tests were performed at the request of GPU Nuclear to support the plant recovery effort.

After completing the physical examinations of the bulk samples, discrete particles were removed from the larger (>1000 μm) size fractions for individual examination, and aliquots were obtained from the smaller (<1000 μm) size fractions. The remainder of the sample material was temporarily stored, pending further examinations, should they be required. Selection of discrete particles was not done on a representative basis; that is, particles were chosen based on specific characteristics of interest (shininess, surface characteristics, pieces of cladding, fuel pellets, etc.). The discrete particles and aliquots were examined visually, photographed, and weighed. Portions of each particle or aliquot were removed and encapsulated in preweighed aluminum cylinders in preparation for radiochemical examination.

2.3.2 Metallurgical Examinations

The large particles generally could be visually classified in one of five categories: fuel; cladding; foamy/porous, prior molten; composite fuel/prior molten; or metallic. Particles from each category were examined metallurgically. Prior molten fuel material was identified by its foamy, glazed, or layered appearance; structural material was identified by its metallic (shiny) appearance. The particles selected for examination were not homogeneous; thus portions removed earlier from particles for differential thermal analysis at RHO and radiochemical analyses were not necessarily representative of the portion examined metallurgically.

Initially, seven particles were selected from Samples 1 and 6 for metallurgical analysis at INEL. Subsequently, 22 additional particles were selected from Samples 1 and 3 through 11 for metallurgical analysis at Argonne National Laboratories. The 29 particles were mounted in conductive Bakelite to facilitate later analysis by SEM. They were ground, to expose the surface to be examined, and polished. Photographs were taken at magnifications from 15 to 500X. Most particles were etched using a fuel or zircaloy etchant and rephotographed. After optical metallography, 27 particles were examined by SEM/EDS. Fourteen of those particles were selected because of their unusual microstructural compositions and were further examined by SAS.

Microstructural information was obtained from the optical photomicrographs. The volume fractions and distribution of different phases and transformation structures were identified to obtain information on the thermal histories of the particles. In addition, general compositional information was obtained based on color and reflectivity of the material.

Additional microstructural information was obtained at magnifications up to 2000X, using SEM/EDS analysis. Phase and elemental distributions were obtained from the backscatter electron image, and elemental identification was obtained from EDS for elements with atomic numbers down to 12 (magnesium).

SAS was used to obtain quantitative elemental data for elements with atomic numbers down to 5 (boron). In particular, this analysis was able to quantitatively measure the oxygen content, which is critical in determining the melting temperature of U, Zr, and O mixtures.

2.3.3 Chemical and Radiochemical Examinations

Positions of selected particles from the larger (>1000 μm) particle size fractions and aliquots from the smaller (<1000 μm) particle size fractions from each bulk sample were analyzed by gamma spectroscopy and delayed neutron analysis to determine the radionuclide and fissile/fertile material contents. Those portions then were dissolved for subsequent chemical and radiochemical analyses. The solutions containing the dissolved core debris materials were divided so that portions could be analyzed using both radiochemical and standard chemical techniques. After dissolution, fertile material analysis could not be performed on the liquid samples because of the relatively high hydrogen content in the solutions, which would interfere with the fertile material measurements.

Initial attempts at dissolving the core debris material indicated that much of it was insoluble using normal dissolution methods (HNO_3 + HF). Therefore, a pyrosulfate fusion technique was developed which produced satisfactory results. The dissolution was performed in a closed system to contain the volatile ^{129}I and Te (Figure 6).[a] Stable carrier I and ^{131}I tracer were added to the fusion to determine losses of ^{129}I during the dissolution process. To evaluate the loss of Te in the dissolution, several experiments were performed using ^{125}Te as a tracer. Experiments indicated retention of more than 80% of the ^{125}Te tracer in the nonvolatile portion of the dissolved material. The rest of the ^{125}Te tracer (∿20%) was lost either by plateout on the glassware or volatilization.

The ^{129}I content in the volatile fraction of the dissolved material was determined using neutron activation. Subsequent gamma spectroscopy of the material determined the amount of ^{131}I tracer and ^{130}I (an activation product of ^{129}I).

The ^{90}Sr content was determined by placing the nonvolatile portion of the dissolved material in solution in water and precipitating the ^{90}Sr and Sr carrier out as a carbonate. The ^{90}Sr fraction was filtered and analyzed using the standard analysis method discussed in Appendix A.

---

[a] Volatility, as used in this section of the report, applies to dissolution and subsequent gasification of elemental components for which analyses were performed. Because of the temperature and acidity conditions during the dissolution, the volatile materials of interest would become gaseous and dissociate from the solution.

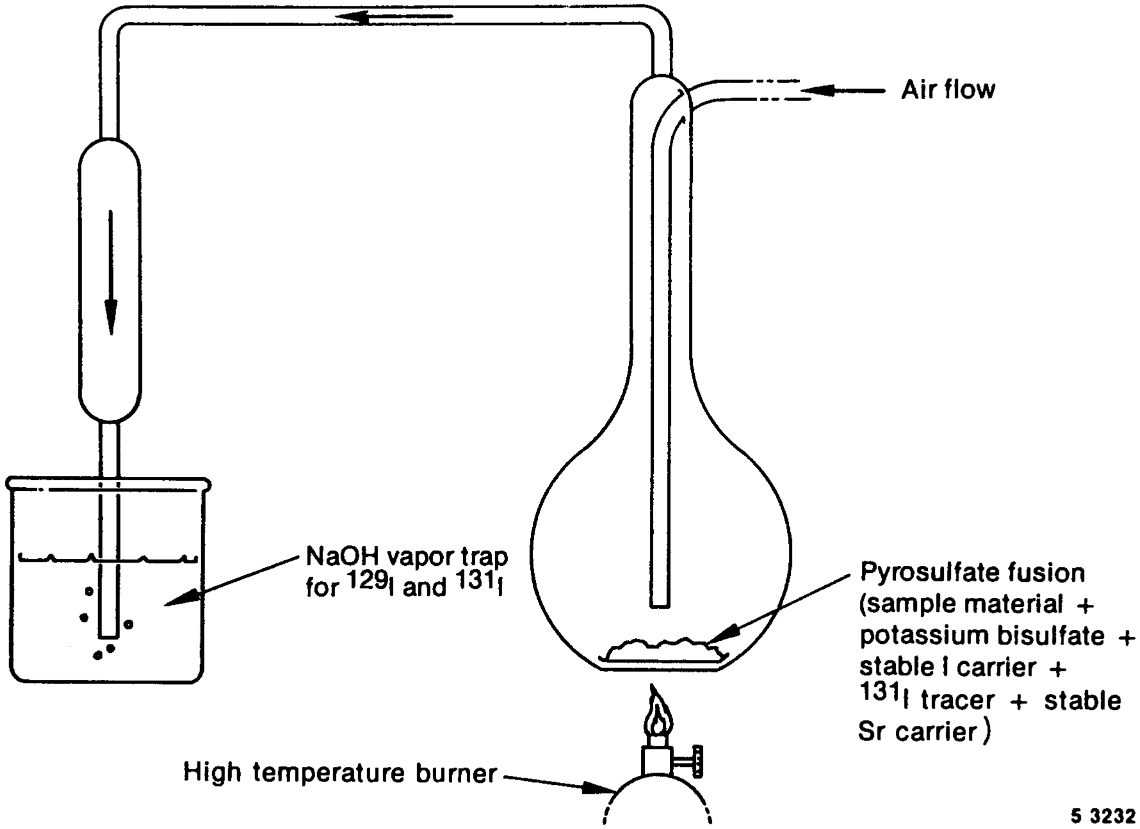
Air flow
NaOH vapor trap for ^{129}I and ^{131}I
Pyrosulfate fusion (sample material + potassium bisulfate + stable I carrier + ^{131}I tracer + stable Sr carrier)
High temperature burner
5 3232

Figure 6. Schematic of the pyrosulfate fusion technique used to dissolve particles and aliquots from the core debris grab samples.

Generally, all other elements remained in the nonvolatile portion. Inductively coupled plasma spectroscopy (ICP) was used to analyze for the following elements: Ag, Al, B, Cd, Cr, Cu, Fe, Gd, In, Mn, Mo, Ni, Nb, Si, Sn, Te, U, and Zr. These elements are the principal elemental constituents present in the core. To evaluate losses of these constituents from the pyrosulfate fusion dissolution and subsequent separations, the U content measured by ICP was compared with the U content measured by delayed neutron analysis of the material before dissolution. Similar results (within 10 to 15%) were obtained, indicating that little material was lost for most samples during the dissolution and separations. The ICP results were used in determining sample compositions and ratios of the elements.

Each recombined bulk sample was dissolved and analyzed to measure its average elemental and radiochemical concentration. Dissolution of the recombined bulk samples was difficult because of the relatively large (up to 50 g) mass of highly insoluble debris. The dissolution was performed in a hot cell because of the high radiation fields (up to 100 rad/h, β/γ). Safety concerns prevented using the pyrosulfate fusion technique in a hot cell because of the potential for fire or explosion. Therefore, a sequential dissolution was performed using acids of lesser strengths. The dissolutions were performed in a closed quartz system similar to Figure 6, but at lower temperatures using a hot plate instead of a high temperature burner. The acids and sequence of use were: (a) $6\underline{M}$ HNO_3, (b) $3\underline{M}$ HNO_3 + $1\underline{M}$ HF, and (c) aqua regia. Dissolution of each recombined bulk sample required 3 to 4 days, with several additions of HCl to the aqua regia solution.

The resulting volume of solutions for each recombined bulk sample ranged from 300 mL to 1 L, with specific activities up to 200 mrad/h per mL of solution. Small (∿10 mL) portions of each solution were removed, diluted, and analyzed using the techniques described previously for the particles and aliquots. No ^{129}I analysis was performed because the sequential dissolution made use of stable carrier I and ^{131}I tracer unfeasible.

3. EXAMINATION RESULTS/DISCUSSION

This section presents results of the physical, metallurgical, chemical, and radiochemical examinations of the TMI-2 core debris grab samples, as described in Section 2. Principal results include the following:

- Most of the particles examined contain regions of prior molten U-Zr-O, indicating that peak temperatures greater than 2800 K were reached in the core. Also, there are a few prior molten particles that are almost pure UO_2, suggesting temperatures up to 3100 K.

- The regions of prior molten U-Zr-O usually contain at least traces of some structural materials (Al, Cr, Fe, and Ni). These elements often are found at grain boundaries or in voids. For some particles, structural materials are a significant fraction of the particle. Control rod materials (Ag, In, and Cd) are not as prevalent as structural materials.

- Ag, a control rod material, apparently had less of a tendency to mix or interact with fuel rod materials (Zr and U) than did structural materials. Significant depletion of Ag ($\sim$90%) from the samples was observed.

- The data suggest the presence of multiple temperature excursions during the accident.

- Evidence was found of the flow of molten metallic U and Zr inside ballooned cladding.

- Significant Zr depletion ($\leq$50%) has occurred from the majority of the samples analyzed, indicating significant relocation of Zr from the debris bed.

- Evidence of significant relocation/mixing of core materials is inferred from the distribution of Gd and the U enrichments.

- Al and Te appear to have concentrated at the surface of the debris bed.

- The radionuclides are retained in the samples in the approximate order of their volatilities.

- Evidence of a correlation between Ni content and ^{125}Sb and ^{106}Ru concentrations was observed, suggesting a possible retention mechanism.

The results are discussed in detail in the following subsections.

3.1 Physical Analyses

This section describes the results of the visual and photographic examinations, weighing, bulk tap density measurements, particle size and weight frequency distribution analyses, categorization of particle types, and ferromagnetic and pyrophoricity tests performed on the 10 samples. These examinations provided the first information on the condition and composition of the core debris material. It was determined through these tests that the particles range from approximately 10 millimeters to a few micrometers in size. The particles were categorized visually by type. There are five general types of particles ranging from basically unaffected segments of fuel pellets and cladding to prior molten material. The smaller (<1000 μm) sized particles contain about 10% ferromagnetic material. There were no pyrophoric materials found in the samples analyzed.

The results of the physical examinations were used to help develop the follow-on examination plan and select the types and quantities of materials for the subsequent metallurgical, chemical, and radiochemical examinations.

3.1.1 Visual and Photographic Examinations and Weights of Bulk Samples

As the sampling tools were opened and the contents removed, visual examination was conducted and photographs were obtained of each sample. Photographs of each bulk sample are presented in Appendix B. Overall description of the ten samples, including their original locations in the reactor, weights, gross gamma radiation levels, and visual characteristics as first examined are presented in Table 3.

As the sampling tools were opened, most of the samples were observed to be stratified according to particle size (the larger particles were at the top and the smaller particles at the bottom of the sampling tool chamber). Because most of the subsurface samples had this type of stratification, it was concluded that the smaller particles settled to the bottom of the sampling tools as a result of the sampling technique and/or handling and shipping operations. The debris bed most probably would not have had a similar stratified distribution at each of the several depths sampled.

3.1.2 Bulk Tap Density

Dry bulk tap density measurements were made for Samples 1, 3, 6, 9, 10, and 11 (Table 4). The average of the densities from the first group of samples (Samples 1, 3, and 6) is 30% less than that from the second group (Samples 9, 10, and 11). The particle size distribution analysis performed subsequently (see Section 3.1.3) revealed that Samples 1, 3, and 6 have the largest particle size fraction of material in the 1680 to 4000-μm size range, whereas Samples 9, 10, and 11 show a bimodal distribution, with peaks at the 1680 to 4000-μm and 297 to 707-μm sizes. The greater weight percent of small particles in Samples 9, 10, and 11 probably allowed more efficient packing and, therefore, caused the higher bulk densities.

TABLE 3. RESULTS OF VISUAL AND PHOTOGRAPHIC EXAMINATIONS, WEIGHING, AND GROSS RADIATION SURVEY OF THE TEN BULK SAMPLES

Sample	Sampling Tool	TMI-2 Core Location	Depth of Sample in Debris Bed (cm)	Sample Weight (g)	Gamma Radiation Level[a] (rad)	Visual Characteristics[b]
1	Clamshell	H8	Surface	70.88	16[c]	A pile of very black, damp debris with a fairly wide range of particle sizes (up to 10 mm); several rounded surfaces; sporadic rust color throughout.
3	Rotating tube	H8	56	152.71	36[c]	Very black, slightly damp debris with wide range of particle sizes (up to 5 mm); small chunks to fine debris; similar to Sample 1.
4	Clamshell	E9	Surface	16.59	3[c]	Thirteen major chunks of black, dry debris with rust colored sides; basically sharp edges with one or two chunks having rounded edges; dimensions range from 5 to 10 mm.
5	Rotating tube	E9	8	90.96	18[c]	Similar to Sample 4 with the following differences: many more pieces, greater size range (1 to 10 mm), some surfaces more reflective; very dry.
6	Rotating tube	E9	56	140.73	36[c]	Very black, slightly damp debris; small chunks to fine debris; some pieces blackish gray; a few pieces resemble metal shards similar to Sample 3.
7	Rotating tube	H8	36	135.86	20[d]	A wide range of particle sizes (up to 10 mm); porous surfaces; sporadic rust areas.
8	Rotating tube	H8	70	152.76	22[d]	A wide range of particle sizes (up to 5 mm); smooth, angular surfaces; pieces of cladding.
9	Rotating tube	H8	77	153.08	25[d]	Very fine, dark debris with only a few larger rounded chunks and metallic particles.
10	Rotating tube	E9	74	173.90	30[d]	A wide range of particle sizes (up to 10 mm); rounded, angular surfaces.
11	Rotating tube	E9	94	148.75	20[d]	Similar to Sample 10 with the following distinctions: a larger fraction of particles resemble fuel pieces, more smaller chunks.

---

[a] Radiation levels measured using a teletector probe on the exposed sample.

[b] All samples appeared to be of a loose granular nature with some sharp or rounded edges.

[c] Reading at 2.5 cm.

[d] Reading at 5 cm.

TABLE 4. BULK TAP DENSITIES OF THE TMI-2 CORE DEBRIS GRAB SAMPLES

Sample	TMI-2 Core Location	Depth of Sample in Debris Bed (cm)	Bulk Tap Density[a] (g/cm^3)
1	H8	Surface	3.5
3	H8	56	3.8
6	E9	56	3.5
			3.6[b]
9	H8	77	5.0
10	E9	74	5.5
11	E9	94	5.0
			5.2[c]

---

a. Bulk tap densities were not measured for Samples 4, 5, 7, and 8.

b. Average of Samples 1, 3, and 6.

c. Average of Samples 9, 10, and 11.

3.1.3 Particle Size Distribution

The particle size distribution of the samples was determined using the method described in Section 2.3.1. The particle size fractions were weighed and photographed (see Appendix B). Results of the particle size distribution analyses are presented in Table 5. Also, the cumulative weight distributions of each sample and the combined samples are shown in Figures 7 and 8. The particle size distribution as a function of depth into the debris bed is shown in Figure 9.

Five samples from the H8 core location (Samples 1, 7, 3, 8, and 9, in order of depth into the debris bed) were examined at INEL. The particle size distributions of Samples 1, 7, and 8 are similar in that 81 to 86 wt% of the sample material is larger than 1000 μm in size, and the 1680 to 4000-μm particle size fraction contains the most material. Sample 3 had 90 wt% of its material larger than 1000 μm in size, however, the largest amount of material was in the greater than 4000-μm fraction. Sample 3 was obtained about 20 cm below where a breakable crust had been contacted during the sampling process, which may account for its greater weight percent of larger sized particles. Sample 9 was the deepest sample obtained from the H8 location. During sampling, a hard stop was encountered by the sampling tool at 77 cm into the debris bed. Only 59 wt% of the material was larger than 1000 μm in size, indicating either some settling of the fine material occurred in the debris bed or washout of the fine material occurred from the upper layers. Sample 9 also showed a bimodal distribution of particles, with the major peak at the 1680 to 4000-μm size fraction and a minor peak at the 300 to 710-μm size fraction. The bimodal distribution indicates a more efficient packing and subsequent higher density for this region of the debris bed.

Five samples (Samples 4, 5, 6, 10, and 11, in order of depth into the debris bed) were removed from the E9 location (about mid-radius in the core). The first two samples (Samples 4 and 5) contain and only large (>1000 μm) particles, which correlated with observations made during the CCTV inspection at this location. Sample 6 (E9, 56 cm) was similar to

TABLE 5. RESULTS OF THE PARTICLE SIZE ANALYSIS OF THE TMI-2 CORE DEBRIS GRAB SAMPLES

Particle Size Fraction	Sample 1		Sample 3		Sample 4[a]	Sample 5[b]		Sample 6		Sample 6[c]
(μm)	(g)	(wt%)	(g)	(wt%)	(g)	(g)	(wt%)	(g)	(wt%)	(g)
>4000	12.62	18.4	63.75	42.9	--	69.57	77.1	57.99	42.0	--[d]
1680 to 4000	27.82	40.6	51.45	34.7	--	13.96	15.5	49.39	35.8	0.39
1000 to 1680	15.64	22.8	19.19	12.9	--	6.25	6.9	13.88	10.1	0.30
>1000	--	81.8	--	90.5	--	--	99.5	--	87.9	--
<1000	--	--	--	--	--	0.44	0.49	--	--	--
707 to 1000	7.80	11.4	5.49	3.7	--	--	--	8.93	6.5	0.25
297 to 707	3.20	4.7	6.34	4.3	--	--	--	5.99	4.3	0.19
149 to 297	0.87	1.3	1.27	0.86	--	--	--	0.97	0.70	0.025
74 to 149	0.44	0.64	0.77	0.52	--	--	--	0.67	0.48	0.024
30 to 74	0.17	0.25	0.18	0.12	--	--	--	0.22	0.16	--[d]
<30	--[d]	--	0.013	0.01	--	--	--	--[d]	--[d]	--[d]
Summed weight	68.56	--	148.45	--	--	90.22	--	138.04	--	1.178
Initial weight	70.88	--	152.71	--	16.59	90.96	--	140.73	--	--
Sample loss[e]	2.32	3.3	4.26	2.8	--	0.74	0.8	2.69	1.9	--

Particle Size Fraction	Sample 7[f]		Sample 7[g]		Sample 8		Sample 9		Sample 10		Sample 11	
	(g)	(wt%)	(g)	(wt%)	(g)	(wt%)	(g)	(wt%)	(g)	(wt%)	(g)	(wt%)
>4000	7.38	5.46	5.48	4.04	28.39	18.61	5.69	3.73	15.93	9.32	30.58	20.59
1680 to 4000	59.44	43.98	54.14	39.89	74.55	48.86	53.81	35.26	88.03	51.49	57.44	38.67
1000 to 1680	43.29	32.03	43.70	32.20	28.91	18.95	30.63	20.07	33.56	19.63	21.20	14.27
>1000	110.11	81.47	103.32	76.13	131.85	86.42	90.40	59.23	137.52	80.44	109.22	73.53
707 to 1000	13.48	9.97	15.70	11.57	9.13	5.98	16.18	10.60	11.59	6.78	10.89	7.33
297 to 707	9.77	7.23	12.11	8.92	7.49	4.90	25.31	16.58	14.76	8.63	16.90	11.38
149 to 297	0.89	0.66	1.61	1.19	1.35	0.88	9.03	5.92	3.96	2.32	6.57	4.42
74 to 149	0.54	0.40	0.93	0.69	0.95	0.62	5.34	3.50	1.78	1.04	2.91	1.96
30 to 74	0.35	0.26	1.77	1.31	1.20	0.79	5.66	3.71	1.36	0.80	2.03	1.36
<30	0.02	0.01	0.27	0.20	0.60	0.39	0.96	0.63	--	--	--	--
Summed weight	135.16	--	135.71	--	152.57	--	152.61	--	170.97	--	148.52	--
Initial weight	135.86	--	135.71	--	152.76	--	153.08	--	173.90	--	148.75	--
Sample loss[e]	0.70	0.52	--	--	0.19	0.12	0.47	0.31	2.93	1.68	0.23	0.16

---

a. Sieving was not done. Sample consisted of only large particles.

b. Sieving was limited to four sizes. Sample consisted of mostly large particles.

c. Ferromagnetic material weights. These values are subsets of their respective particle size fractions for Sample 6.

d. None detected (not measurable).

e. The sample loss defines the quantity of material lost during seiving; however, the particle size distribution of the lost material is not known.

f. After 5-min shake.

g. After 1-h shake.

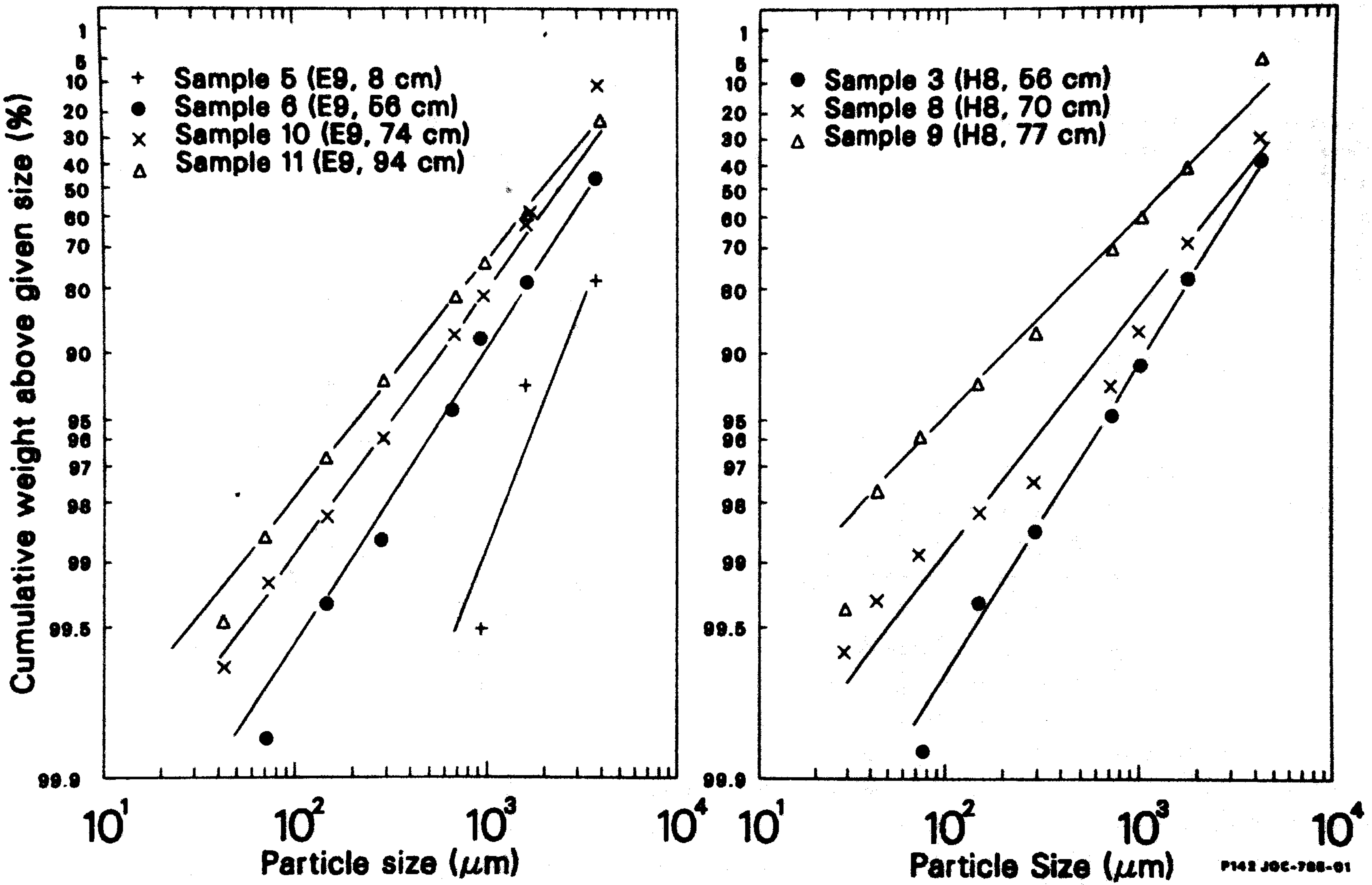

Figure 7. Plots showing the cumulative weight distribution of various core debris grab samples.

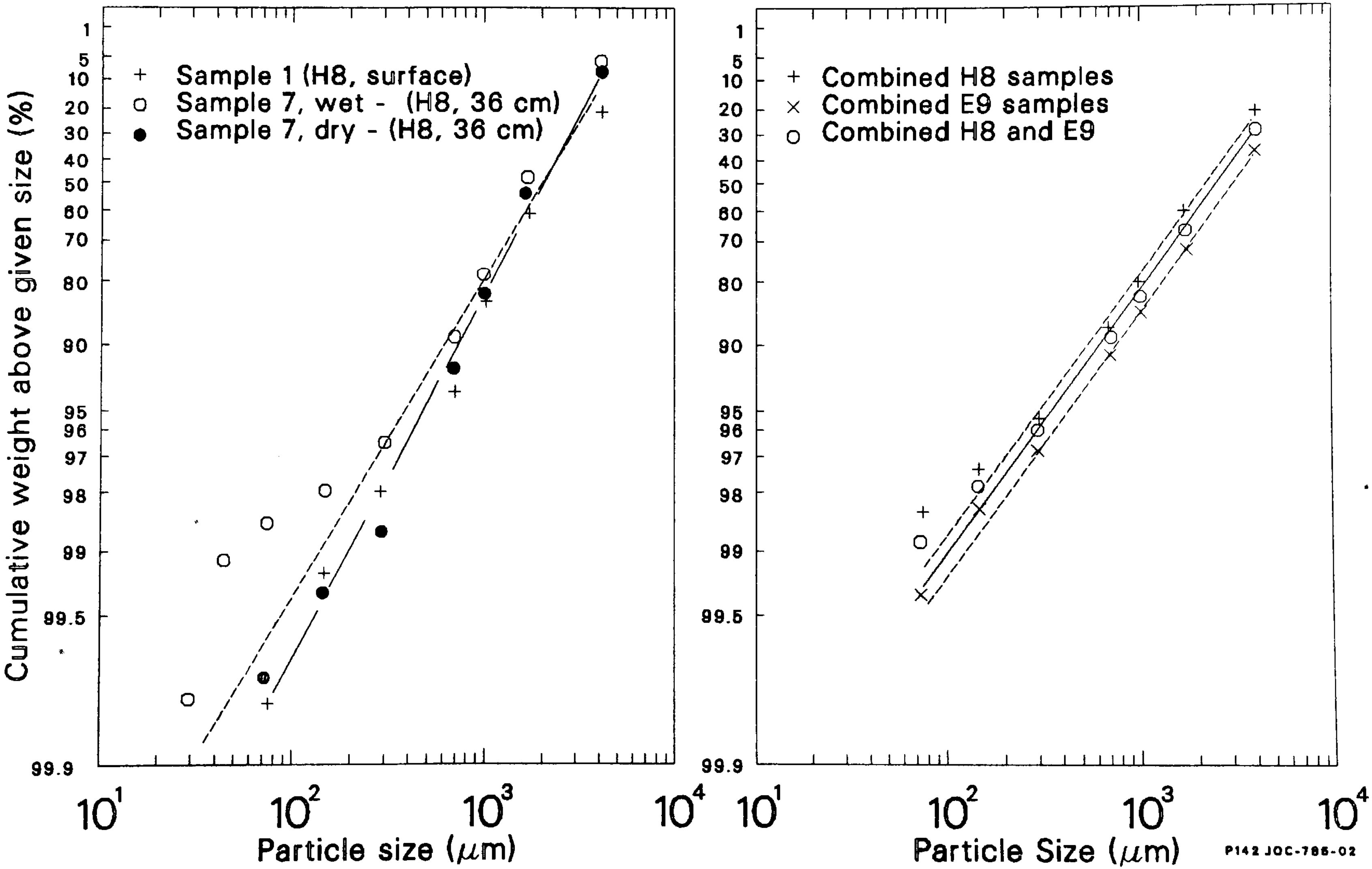

Figure 8. Plots showing the cumulative weight distribution of various core debris grab samples and of the combined samples.

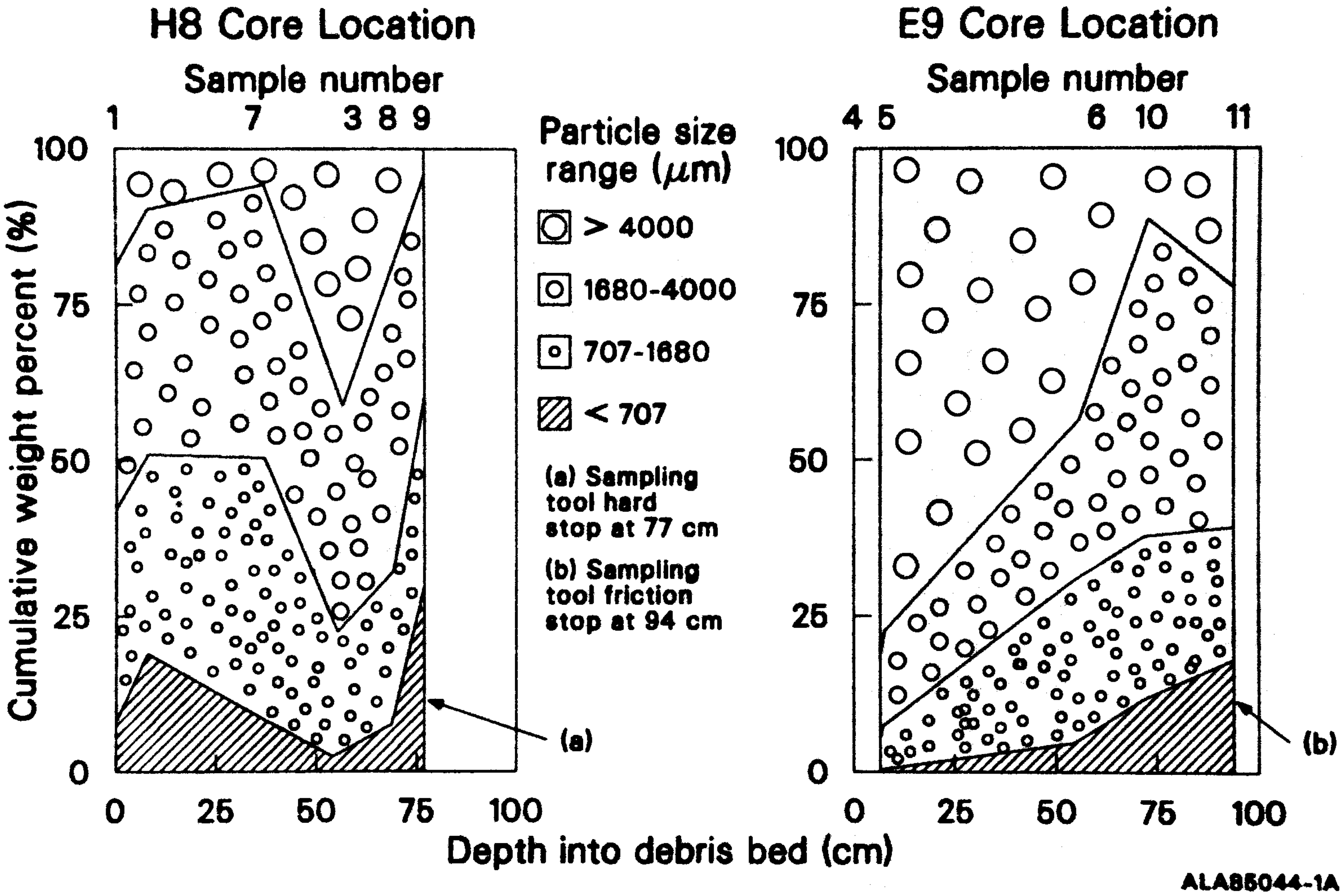

Figure 9. Plot showing the cumulative weight distribution of each core debris grab sample as a function of depth into the debris bed at the H8 and E9 core locations.

Sample 3 (H8, 56 cm) in that about 88 wt% of the material was larger than 1000 μm, of which the largest amount was greater than 4000 μm in size. Samples 3 and 6 were obtained from the same depth (56 cm) into the debris bed, indicating that the effect of the breakable crust may be fairly uniform across the reactor core. Samples 10 and 11 were similar to Sample 9 from the H8 position in that they exhibited a bimodal particle size distribution.

3.1.4 Weight Frequency Distribution

The weight frequency is defined as the distribution of the sample weight as a function of particle size fraction. The following weight frequency distribution information was extracted from GPU Nuclear evaluations of the particle size distribution analyses performed at INEL and B&W. The distribution of weight frequency, for each sample is shown in Figures 10 and 11.

The weight frequency, f, of particle size Dp is calculated as follows:

$$f = \frac{\Delta R}{\Delta Dp} \tag{1}$$

where

f = weight frequency (%/μm)

ΔR = weight percent of particles belonging to the given particle size range (%)

ΔDp = span of the given particle size range (μm).

The weight frequency was calculated with the assumption that all particles were in the 10 to 6000-μm range.

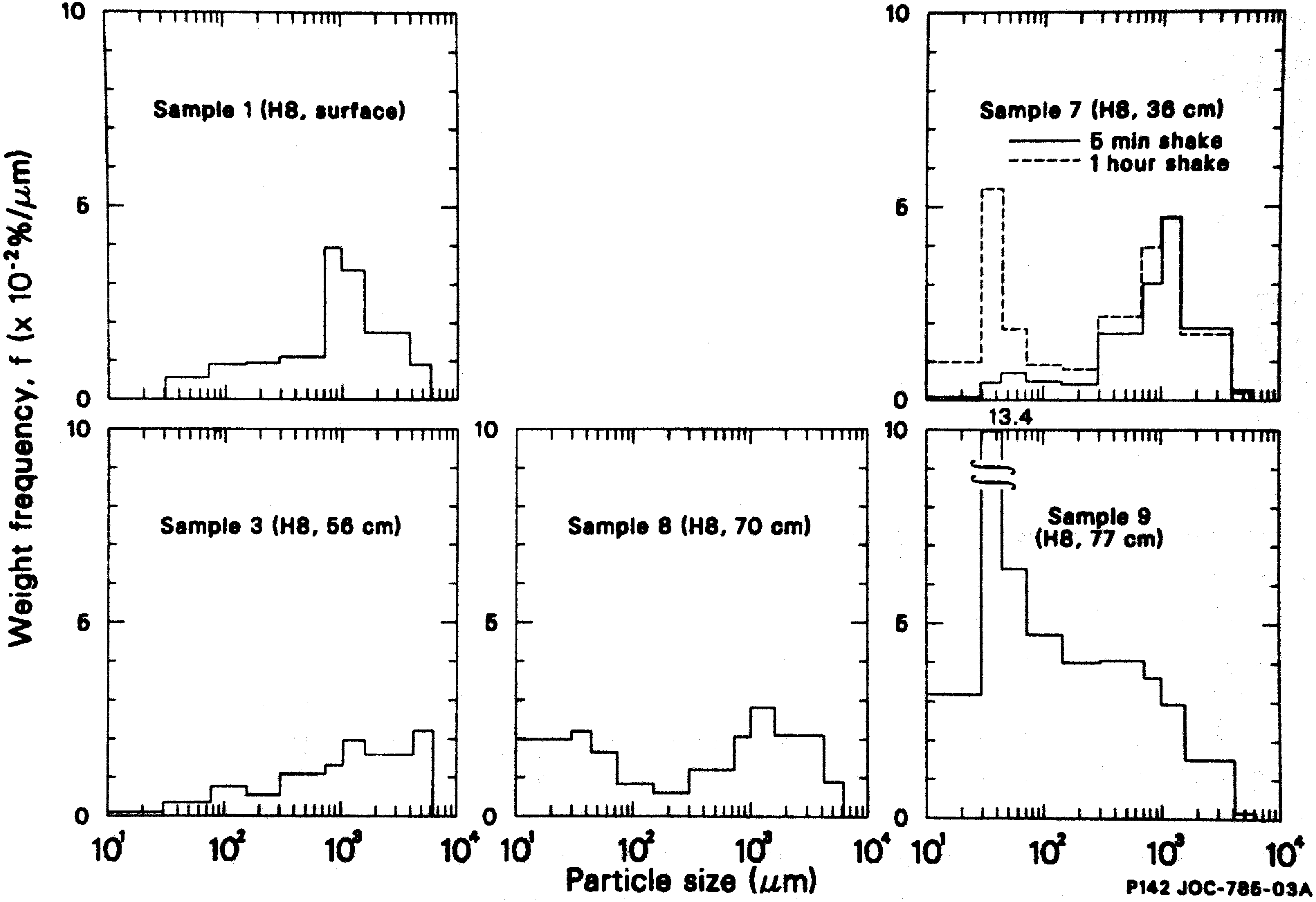

Figure 10. Weight frequency distributions of samples from the H8 core location.

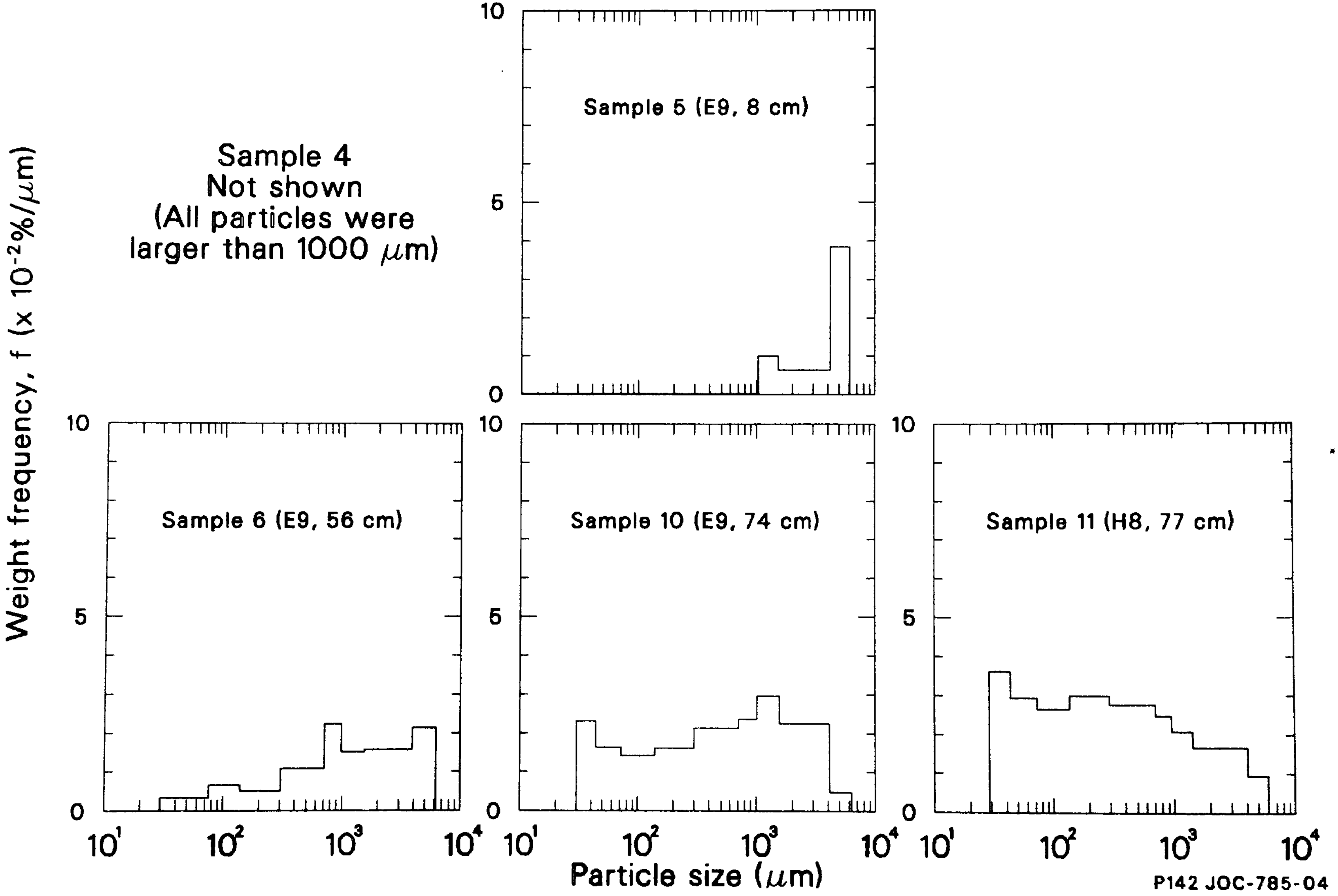

P142 JOC-785-04

Figure 11. Weight frequency distributions of samples from the E9 core location.

The effect of agitation time during sieving for Sample 7 is shown in Figure 10. The 1-h shake caused conversion of portions of the material in the greater than 4000 μm to 1680-μm size ranges to the smaller size ranges, notably the 30 to 74 μm range.

From Figure 10, the following observations were made of samples from the H8 location:

1. The mode sizes (particle size with the highest f value) of Samples 1 and 7 are in the range of 707 to 1680 μm.

2. The mode sizes of Samples 3, 8, and 9 decrease as the depth into the debris bed increases.

3. The weight frequency of the largest particles (i.e., greater than 4000 μm, shown as 4000 to 6000 μm in Figure 10) decreases as the depth increases for the group of Samples 1 and 7 and the group of Samples 3, 8, and 9, but it is discontinuous between Sample 7 (H8, 36 cm) and Sample 3 (H8, 56 cm).

4. For Sample 9 (H8, 77 cm), the 30 to 74 μm particle size range shows a very high weight frequency. This suggests that the small particles were prevented from falling deeper at the H8 location by a blockage which was felt as the hard stop during sample acquisition.

Observations 1, 2, and 3 suggest that the debris particles at the H8 location are stratified into two layers, with the boundary located between 36 cm and 56 cm below the surface of the debris bed. This is supported by the existence of a penetrable "crust-like" layer felt during sample acquisition.

From Figure 11, the following observations were made of samples from the E9 location:

1. The mode sizes of Samples 5, 6, 10, and 11 decreases as the depth into the debris bed increases.

2. No particular discontinuity is apparent between the weight frequency distributions of samples from the E9 location.

3.1.5 Particle Types

The larger particle size fractions for each sample were examined visually after particle sizing, and five general (types) categories of particles were identified based on visual appearance, including (a) obvious fuel pieces; (b) cladding chunks; (c) foamy/porous, prior molten material; (d) particles that are a composite of fuel and prior molten material; and (e) metallic appearing, prior molten particles. Based on subsequent metallography and chemical analysis of several particles from each type, the composite particles generally are assumed to be fuel pellets with a prior molten U-Zr-O material coating the surface or gluing the fuel particles together. The composite particles have rounded edges and corners and sometimes a glazed surface appearance. It is assumed that the metallic appearing, prior molten particles are probably the structural materials with lower melting temperatures. Examples of particles from each of the five types are shown in Figures 12 through 16.

In general, all particle types were found in all samples. However, some trends could be noted. Samples 1, 7, and 8 from the H8 location appeared similar visually. No easily recognizable cladding pieces were found in the largest particle size fractions of those samples, although subsequent examination did reveal some cladding pieces with fuel attached in all three samples. About 15% of the larger sized particles were recognized as fuel pieces, and the remaining material consisted of foamy, highly porous particles and composite particles. Sample 7 had a higher fraction of foamy particles than did Samples 1 and 8. Sample 3 was similar to Samples 1, 7, and 8 in that the fuel pieces comprised about 15% of the large particles, however, the sample contained mostly composite particles

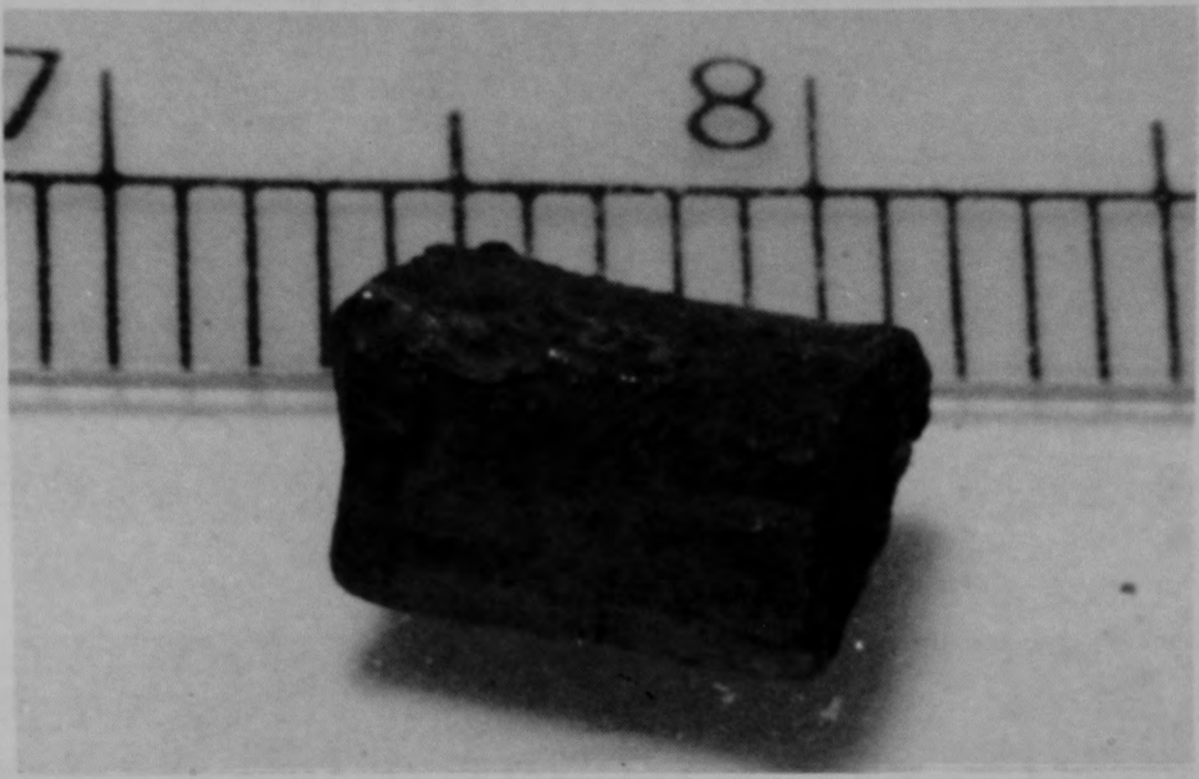

Figure 12. Photograph of Particle 1B (H8, surface) showing an example of a fuel piece.

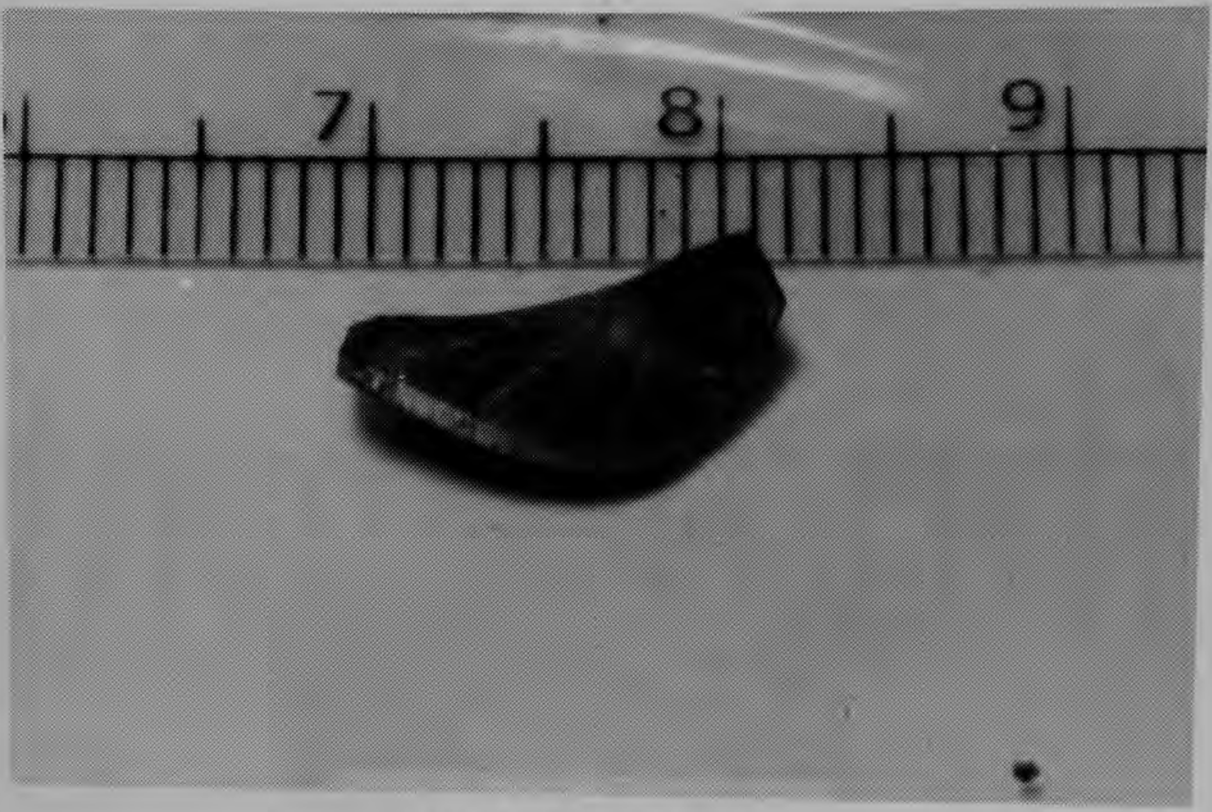

Front view of particle

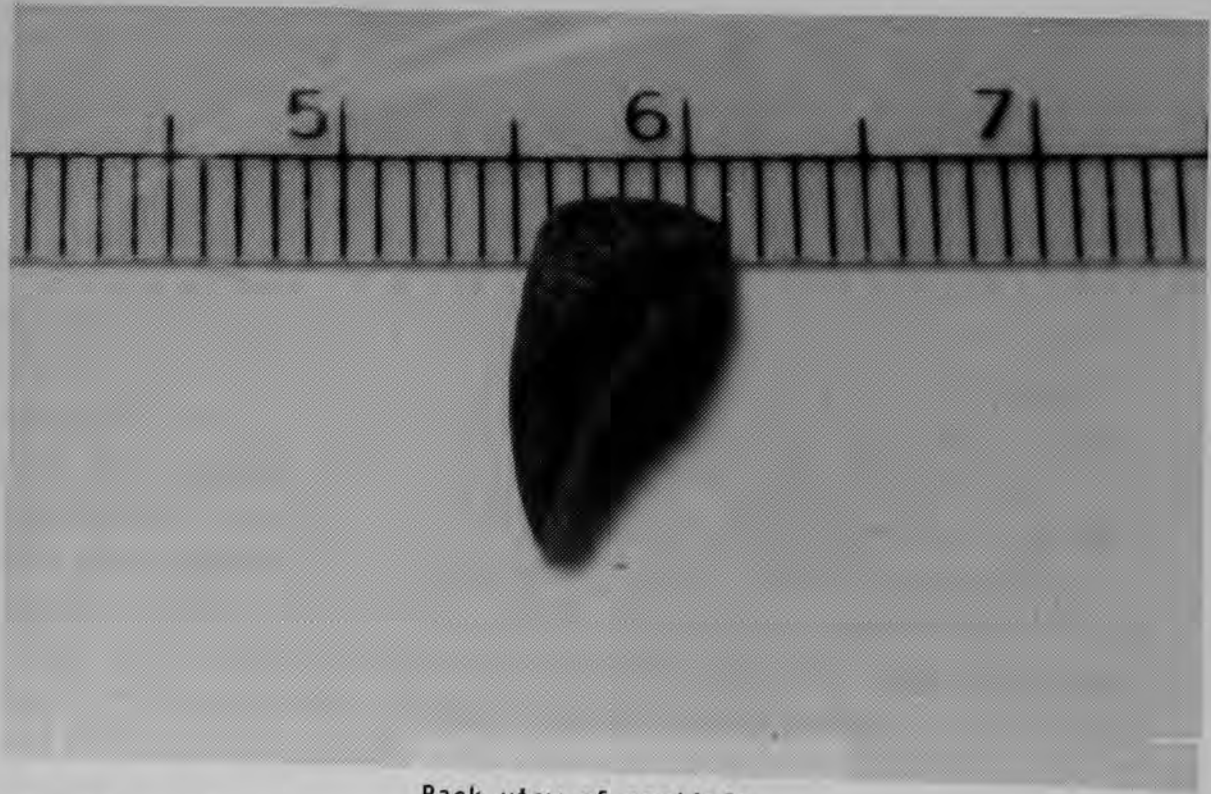

Back view of particle

Figure 13. Photograph of Particle 6E (E9, 56 cm) showing an example of a cladding piece.

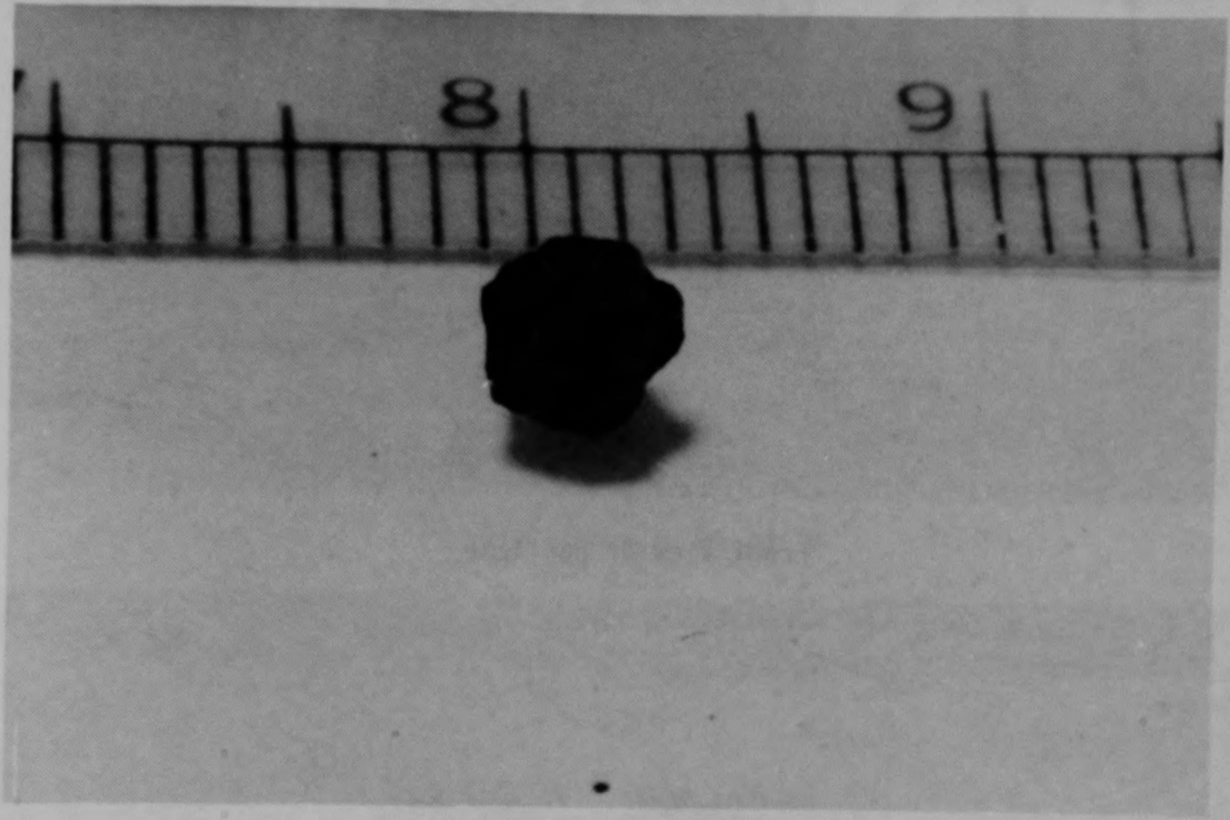

Figure 14. Photograph of Particle 1H (H8, surface) showing an example of a foamy piece.

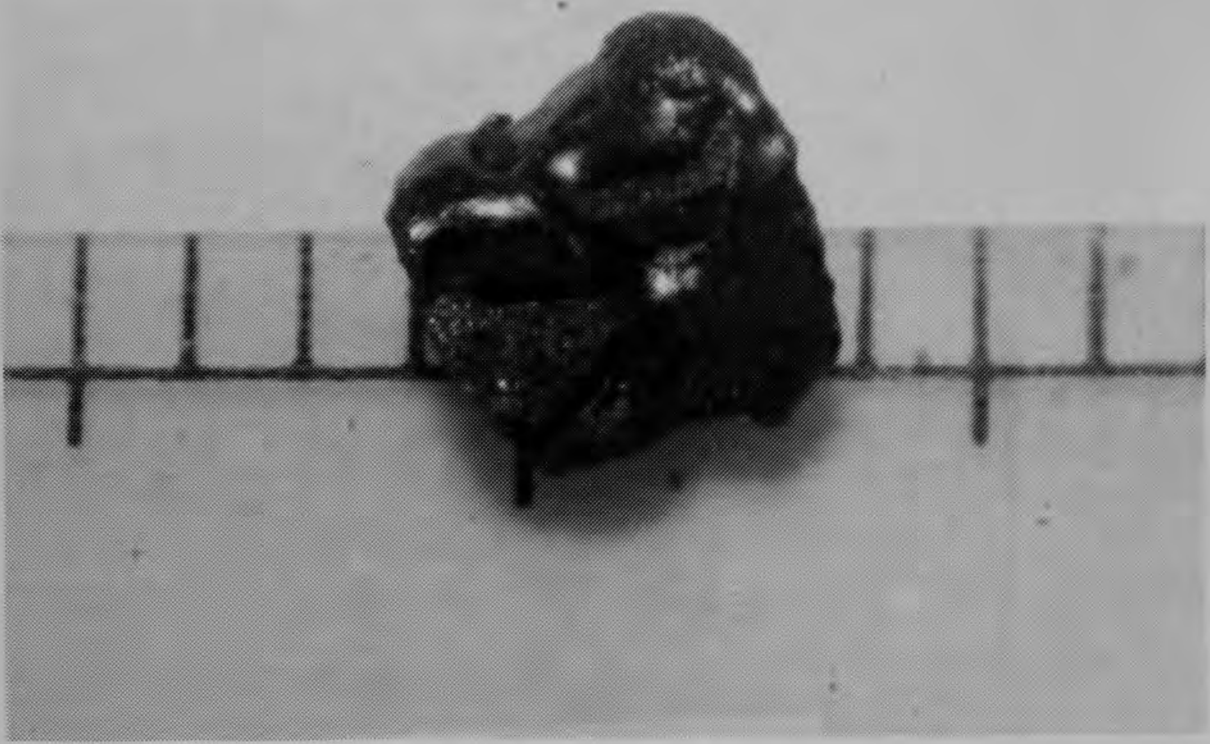

Front view of particle

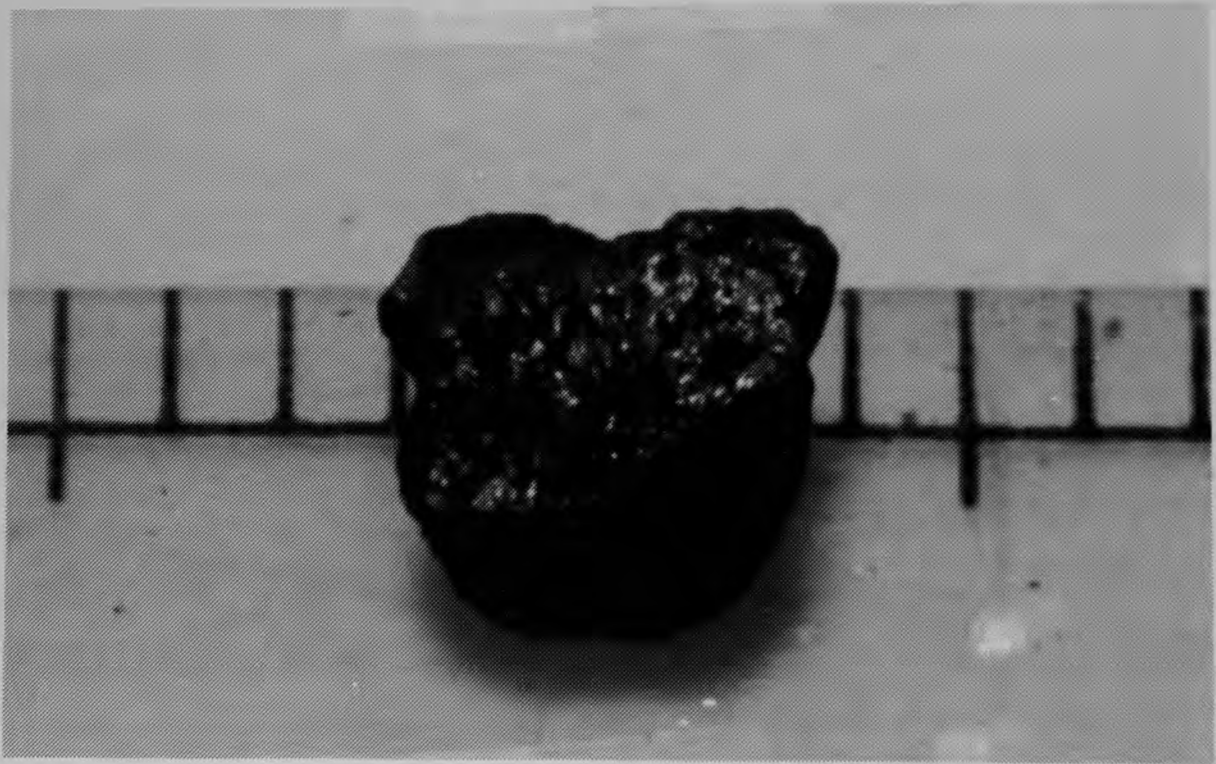

Back view of particle

Figure 15. Photograph of Particle 8C (H8, 70 cm) showing an example of a composite piece.

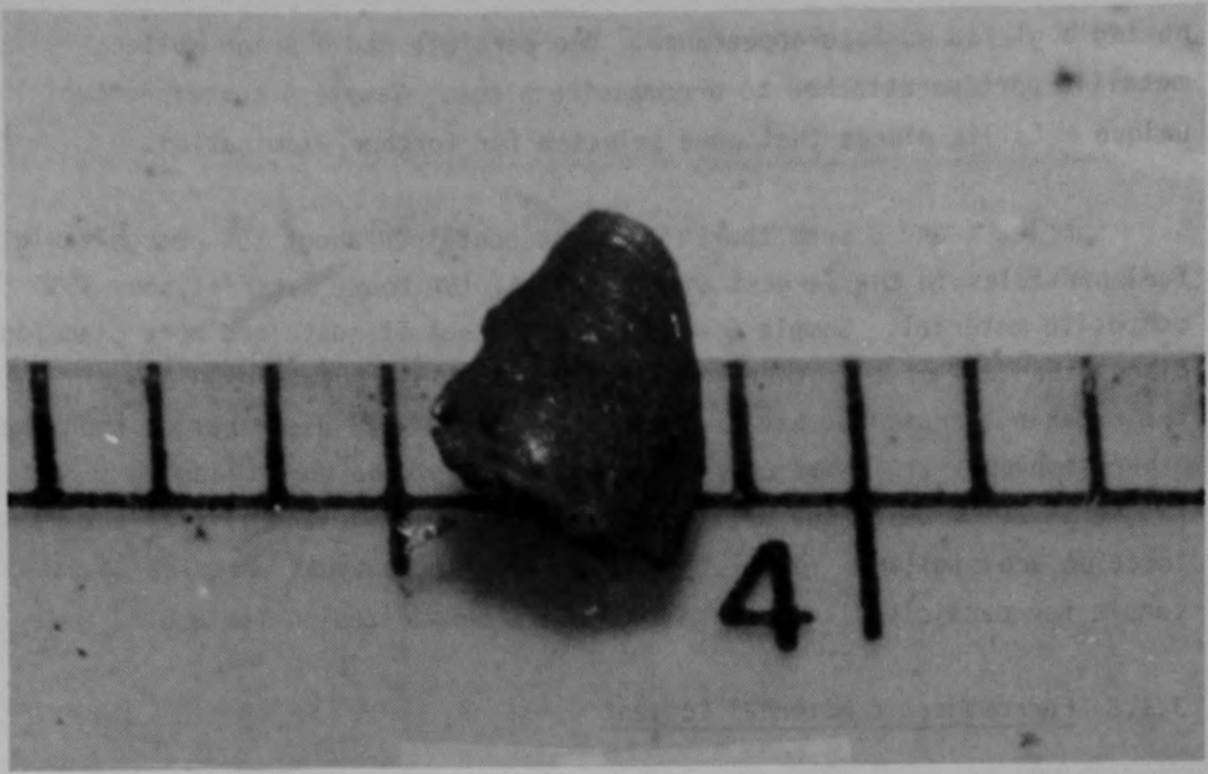

Front view of particle

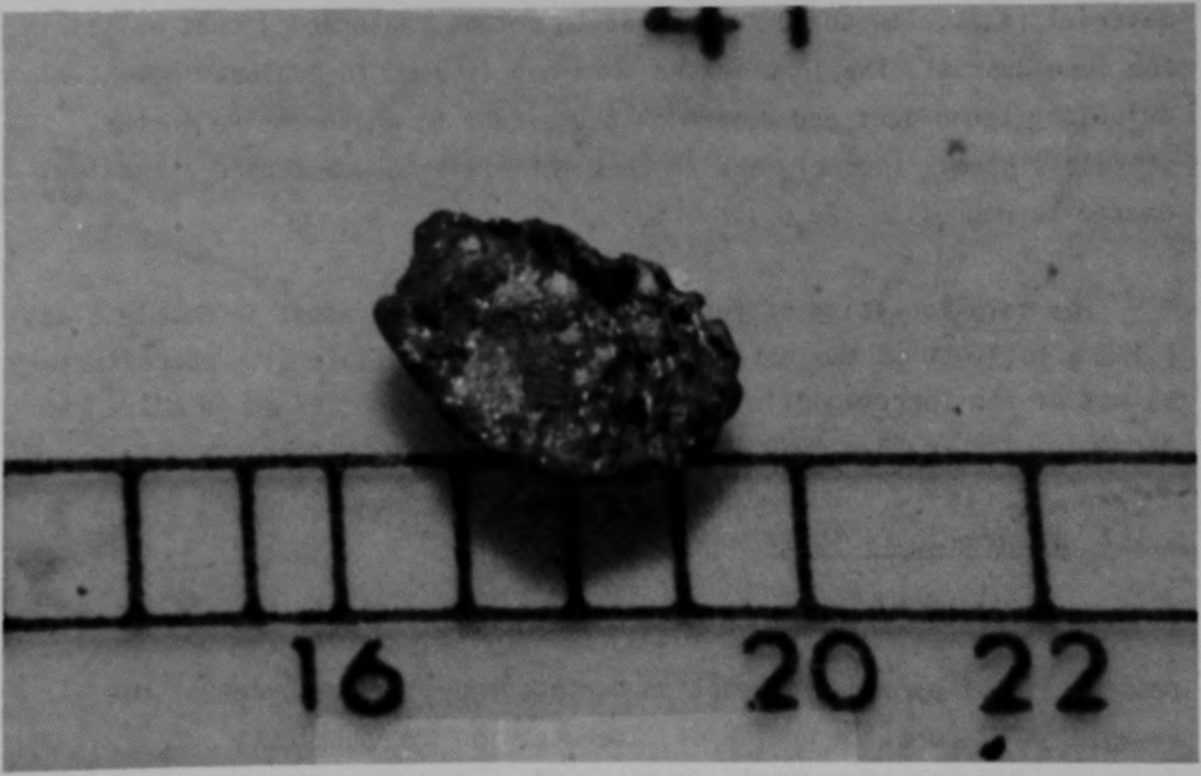

Back view of particle

Figure 16. Photograph of Particle 9G (H8, 77 cm) showing an example of a metallic piece.

having a glazed surface appearance. One particle had a prior molten, metallic portion attached to a composite piece. Sample 9 contained two unique metallic pieces that were selected for further examination.

Samples 4 and 5 from the E9 location contained about 30% recognizable fuel particles in the largest size fraction, 15% foamy material, and 55% composite material. Sample 6 was unique in that it contained more cladding pieces than all of the other samples. Sample 6 was obtained 20 cm below the breakable crust and had a different particle size distribution than the other samples. It is not apparent why there would be more cladding fragments 20 cm below the breakable crust. Samples 10 and 11 from the E9 location are similar. The distribution of particle types observed in each sample for particles larger than 1000μm are summarized in Table 6.

3.1.6 Ferromagnetic Material Content

The ferromagnetic material content test was performed at the request of GPU Nuclear to determine the quantity of demonstratably magnetic material (i.e., low concentration would not be measurable) that exists in the core debris. The information obtained is used to evaluate potential defueling techniques and determine the extent to which the Fe in the stainless steel, Inconel, and Zr core materials has undergone a chemical change to magnetite (Fe_3O_4).

The total quantity of ferromagnetic material present in Sample 6 was 1.178 g (0.9 wt% of the total sample weight) (see Table 5). Approximately 95 wt% of the ferromagnetic material was larger than 297 μm in size. No particles larger than 4000 μm were found to be ferromagnetic.

3.1.7 Pyrophoricity Study

The phenomenon of pyrophoricity was investigated to evaluate the possibility of pyrophoric reaction during removal and storage of the damaged TMI-2 core. A review of literature on pyrophoricity[7] (concentrating on experiences of the nuclear industry with Zr metal)

TABLE 6. PARTICLE TYPE DISTRIBUTION OF THE TMI-2 CORE DEBRIS GRAB SAMPLES[a]

	Particle Types[b]				
Sample	Fuel	Cladding	Foamy/Porous	Composite	Metallic
1	15	0	20	65	0
3	15	0	10	75	0
4	30	0	15	55	0
5	30	0	15	55	0
6	50	20	10	10	10
7	15	0	64	21	0
8	12	2	27	59	0
9	18	0	0	73	9
10	54	0	0	46	0
11	48	0	7	45	0

---

a. Given as approximate percent of larger (>1000 μm) sized particles. Less than 1% was rounded off to zero.

b. There are five general types of particles found in the core debris grab samples. See Section 3.1.5 for descriptions of each type.

combined with evaluation of core material reactions at high temperature that occurred during the TMI-2 accident, indicate that pyrophoric reactions during defueling would be unlikely.

A series of ignition tests were performed at INEL on samples of core materials removed from all size fractions between 30 and 4000 µm of Samples 3 and 6. The samples were tested under both wet and dry conditions, and ignition of the material was attempted using both a Tesla Coil and a propane torch. In no case did ignition of the materials occur.[8]

Differential thermal analyses were conducted by Rockwell Hanford Operations on fragmented chips from seven particles (Appendix H). The particles generally showed little thermal activity, although one particle produced a large, broad release of energy (exotherm) of 761 cal/g, spanning nearly 500 degrees, starting at about 550°C. This exotherm occurred at much higher temperatures than those observed for samples of Zr powder and partially oxidized Zr powder. If the exotherm is due to the oxidation of Zr, the Zr in the sample must have been coated with a thick non-combustible, possibly oxide, layer which protected it at lower temperatures. The results of this test are contained in Appendix H.

3.2 Metallurgical Analyses

Twenty-nine particles from the ten core debris grab samples retained at INEL were selected for metallurgical analyses. Twenty-two particles were studied jointly by EG&G Idaho and Argonne National Laboratories (East and West), while the remaining seven were characterized by EG&G Idaho and Westinghouse Idaho Nuclear Co. This section presents results of the optical metallography, scanning electron microscopy with energy dispersive x-ray spectroscopy (SEM/EDS), and scanning Auger spectroscopy (SAS). From these analyses, the microstructural appearances and elemental compositions of the particles were determined, estimates were made of maximum temperatures experienced during the accident, and interactions between fuel rod and non-fuel rod materials were investigated.

3.2.1 Summary of Examinations

The metallurgical analyses provided data in the form of optical photographs, SEM backscatter and secondary electron images, x-ray spectra from the SEM/EDS examinations, and quantitative elemental compositions from the SAS analyses. The area fractions of the major components, grain sizes, and peak temperature estimates are summarized in Table 7. Element identification is based on the SEM/EDS data, except for oxygen content which is based on the SAS data, (note that not all particles were analyzed by SAS). The oxygen contents listed in Table 7 represent the ranges found in the base material (not inclusions or grain boundary phases). Area fractions of the various components were determined from visual examination of optical photographs and SEM images. Fuel grain size was determined using the line intercept method with a 3-D to 2-D conversion factor of 1.57. The grain size listed for Particle 4A was from the minimum grain size region of that particle. The peak temperature estimates shown in Table 7 are discussed in Section 3.2.2. The "other phases" referred to in Table 7 are the various materials found in grain boundaries and voids, along with the trace amounts of Fe that were sometimes found in the base material, and are discussed in Section 3.2.3. The composition of inclusions represents the average or typical inclusion (see Section 3.2.3).

Details of the metallurgical data are presented in Appendix C, including representative optical photographs and SEM images, and detailed qualitative SEM/EDS and quantiative SAS data. Appendix C also contains brief descriptions of each particle, and summarizes elemental compositions of each particle.

3.2.2 Temperature Estimates

Estimation of the temperature history is important for many aspects of the analysis of the TMI-2 accident and is required for defining the accident scenario. For example, estimates of fission product release are extremely temperature dependent, with highly volatile fission products released at lower fuel temperatures (<2100 K) and less volatile fission

TABLE 7. SUMMARY OF METALLURGICAL ANALYSIS OF THE TMI-2 CORE DEBRIS GRAB SAMPLES

Particle	Area Fraction[a] of UO_x	Grain Size (mm)	Area Fraction[a] of $(U,Zr)O_x$	Area Fraction[a] of ZrO_x	Area Fraction[a] of Other Phases	Composition of Inclusions	Area Fraction[a] of Unoxidized Metallic Regions (not inclusions)	Traces of Iron Found in Base Material	Oxygen Content Range of Base Material From Auger Analysis (at%)	Peak Temperature (K)
1A	0.5	10	0.3 (U,Zr) metallic	Tr	--	--	0.2 Zr	--	--	2170-2245
1B	1	12	Tr	Tr	--	--	--	--	--	2170-2600
1E	0.1	--	0.1	0.2	--	--	0.6 Zr	--	~67*	2810-2960
1H	--	--	0.8	--	0.2^d	--	--	--	--	>2810
3L	--	--	1	--	--	--	--	--	65-72	>2850
3M	0.4	11	0.6	--	--	--	--	--	--	>2850
4A	0.3	>18	0.5	--	0.2^d	Ni-Sn, Ru-Ti	--	Y	--	~2810
4B	0.3	>18	0.7	--	Tr^d	Ni-Sn, Ru-Tc	--	--	64-70	~2810
4D	--	--	1	--	--	Cr-Fe-Ni-Sn	--	--	--	>2850
5E	0.1	$\sim 12^b$	0.9	--	Tr^c	Ru-Ni-Tc-Rh	--	Y	68-74	~2810
6B	--	--	--	--	--	--	1.0 Zr	--	--	<2245
6C	--	--	0.5	0.3	0.2^e	Ni-Sn-Zr-Al-Zr-U	--	--	63-69	2170-2960
6D	0.9	10	0.1	--	--	--	--	--	~70	2170-2810
6E	--	--	--	0.2	--	--	0.8 Zr	--	--	~2000
6F	--	--	0.8	--	Tr^d	--	0.2 Ni (Fe)	--	--	2170-2810
7A	--	--	0.6	--	0.4^d	Ni-Fe	--	Y	--	~2810
7B	0.3	$\sim 10^b$	0.2 (U,Zr) metallic	0.2	--	--	0.3 Zr	--	--	2170-2245
7E	0.3	28	0.6	--	Tr^g, Tr^d	Ni-Sn-Fe	0.1 Ni (Fe)	--	65-70	~2810
8A	--	--	1	--	Tr^d	Mo-Sn	--	--	66-70	~2810
8C	--	--	0.6	-- 0.2^c	0.2^d,	Ag	--	Y	62-66	>2170

TABLE 7. (continued)

Particle	Area Fraction[a] of UO_x	Grain Size (μm)	Area Fraction[a] of $(U,Zr)O_x$	Area Fraction[a] of ZrO_x	Area Fraction[a] of Other Phases	Composition of Inclusions	Area Fraction[a] of Unoxidized Metallic Regions (not inclusions)	Traces of Iron Found in Base Material	Oxygen Content Range of Base Material From Auger Analysis (at%)	Peak Temperature (K)
8E	--	--	0.7	--	0.1^c 0.2^f	Ni-Sn	--	Y	70-72	~2810
8H	--	--	0.8	--	Tr^c	Ni-Sn	0.2 Ag	Y	--	>2850
9D	--	--	0.1	--	0.2^h	Ni-Sn	0.7 Ag	Y	--	~2810
9G	--	--	--	--	0.2^h	Ni-Sn	0.8 Ag	--	--	>1233
10A	0.2	28	0.8	--	--	Ni-Sn-Tc-Ru	--	--	65-69	~3100
10E	0.9	10	0.1	Tr	Tr^c	Ni-Sn	--	--	63-71	>2810
10F	--	--	0.9	--	0.1^c	Ni-Ru-Fe	--	Y	68-71	>2850
11B	--	--	0.5	--	0.1^g 0.1^b	Ni-Fe-Sn-Ag-Mo	0.3 Ni (Fe)	--	--	~2810
11C	1	10*	Tr	Tr	--	--	--	--	--	2170-3120

a. Area fractions were estimated by visual examination.

b. Problems were encountered in measuring these grain sizes.

Other phase compositions:

c = Cr-Fe-Ni with varying amounts of U+Zr

d = Al-Cr-Fe-Ni with varying amounts of U+Zr

e = high Al with Zr,U some Fe,Cr

f = different (from base) U/Zr compositions

g = separate Cr-Fe and Ni-Fe bearing phases

h = Ni-Sn with some Ag,Fe (metallic phase)

Tr = trace

Y = yes

* = refers to attached $(U,Zr)O_2$ only.

products released as temperatures approach UO_2 melting. While it is not possible to determine temperature history from examining the core debris grab samples, peak temperatures experienced by the material can be estimated in many cases. These peak temperatures and other TMI system response data can be used in conjunction with accident analysis codes to establish a temperature history.

Peak temperatures can be estimated by several methods: (a) from the appearance of the UO_2 fuel (fuel grain growth and evidence of melting), (b) relating the temperatures at which phase changes occur in zircaloy cladding to the observed structures, (c) correlating the overall composition of the material examined, the number and appearance of the phases present, and the composition of the individual phases to existing phase diagrams, and (d) determining the presence of prior molten structural and control rod materials. The methods for determining peak temperatures are discussed in Sections 3.2.2.1 through 3.2.2.4, and the temperature estimates are discussed in Section 3.2.2.5.

3.2.2.1 Fuel Grain Growth and Melting. Fuel grain growth is highly time-temperature dependent and can be calculated using correlations of time at temperature for a given fuel burnup.[9] These calculations are based on an integrated total time at a given temperature, however, and are difficult to use for transient conditions and multiple temperature excursions. Figure 17 shows the relationships between grain size and temperature for times at temperature of 20 and 40 min. The relationships shown in this figure are for initial grain size and burnup at the time of the accident, and for a range of times at temperatures that have been predicted for the accident. Therefore, an indication of what the temperatures were can be made by comparing measured grain size with the figure.

Other indications that fuel was exposed to high temperatures (>2000 K) are the rearrangement of pores and grain structure. As the melting point of the UO_2 fuel (3120 K) is approached, the fuel grains become almost pore-free, sharp corners on the equiaxed grains become rounded, and the grains separate. When the fuel melts it takes on a foamy appearance, having few small pores and many large, rounded voids.

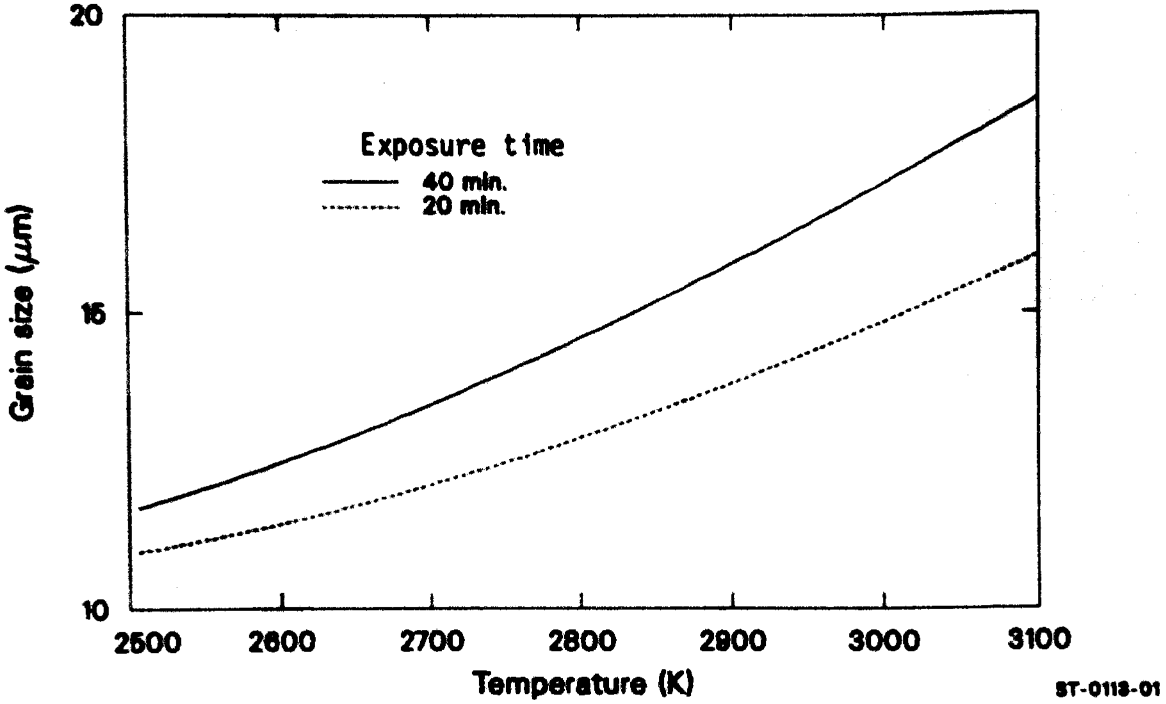

Figure 17. Plot showing the relationship between fuel pellet grain size and times at temperature.

3.2.2.2 Zircaloy Phase Changes with Temperature. Zircaloy cladding progresses through several distinct microstructural changes with increasing temperature. The original (as-fabricated) zircaloy microstructure consists of alpha-zircaloy (α-Zr) grains elongated in the circumferential direction (referred to as a stress-relieved microstructure). This structure is observed with peak temperatures of less than 920 K. With increasing temperature, the α-Zr grains recrystallize and become equiaxed ($920 < T < 1105$ K). At about 1105 K, the transformation from α-Zr to the β-Zr phase begins. The temperature at which this transformation occurs increases with increasing oxygen content in the Zr. The β-Zr transforms back to α-Zr as temperatures are reduced below 1105 K; however, the microstructural appearance of the transformed β-Zr grains (referred to as "prior β-Zr") is distinctly different from the α-Zr grains that were not exposed to temperatures greater than 1105 K. The two-phase α + prior β-Zr mixture is observed in materials exposed to $1105 < T < 1245$ K.

Several phenomena occur between $1245 < T < 2030$ K. As the temperature increases above 1245 K, the α-Zr transforms completely to β-Zr and then transforms back to α-Zr on cooling (prior β-Zr). The prior β-Zr structure appears as large, equiaxed grains with α-Zr platelets within each grain. Interaction of the zircaloy cladding with steam on its outside surface and UO_2 fuel on its inside surface becomes significant above 1245 K, and oxidation of the cladding occurs. Two layers are formed on the outside surface: first, a layer of α-Zr is formed that has been stabilized at high temperatures because of oxygen uptake [denoted α-Zr(O)], and then a layer of ZrO_2 is formed outside the α-Zr(O) layer. The longer the cladding is exposed to temperatures greater than 1245 K, the thicker these two layers can become. The entire wall thickness can eventually transform to ZrO_2 and α-Zr(O). Frequently, there are two layers in the ZrO_2 phase. The inside layer [closest to the α-Zr(O)] contains a metallic α-Zr(O) phase. This indicates that the ZrO_2 was slightly hypostoichiometric at temperature and underwent eutectoid decomposition into stoichiometric $ZrO_{2.00}$ + α-Zr(O) during cooling. This decomposition only takes place if significant amounts (enough to be visible) of the ZrO_2 have been at temperatures above about 1760 K (Figure 18).

If fuel-cladding contact exists, interaction of the cladding with the UO_2 fuel also occurs, resulting in oxidation of the cladding from the inside surface. The internal UO_2/Zr interaction results in the formation of the following reaction layer sequence:

$$[UO_2 + U] \rightarrow [\alpha\text{-}Zr(O)_a + (U,Zr)]$$

$$\rightarrow (U,Zr)\ \text{alloy} \rightarrow \alpha\text{-}Zr(O)_b$$

where

a = the α-Zr(O) next to the fuel

b = the α-Zr(O) near the center of the cladding.

These layers will then be followed by prior β-Zr → α-Zr(O) → ZrO_2 or only α-Zr(O) → ZrO_2, depending on the amount of oxidation from the outside by the steam. The fuel is reduced by the Zr to form metallic α-Zr(O) and elemental uranium. ZrO_2 cannot form as a result of the UO_2/Zr reaction alone. The metallic uranium does not remain at the $UO_2/\alpha\text{-}Zr(O)_a$ interface, because it tends to interact with Zr low in oxygen and diffuses into the cladding to form a (U,Zr) alloy rich in uranium. The (U,Zr) alloy lies between two α-Zr(O) layers and is liquid above about 1425 K, depending on the Zr content. This small quantity of liquid is a product of the solid state diffusion couple. The α-Zr(O) layer adjacent to the fuel contains small amounts of the (U,Zr) alloy, primarily along grain boundaries, but also as small globules within the $\alpha\text{-}Zr(O)_a$ grains. The $\alpha\text{-}Zr(O)_b$ layer adjacent to the prior β-Zr contains no (U,Zr) alloy. During cooldown, the hypostoichiometric UO_{2-x} decomposes into stoichiometric $UO_{2.00}$ and additional metallic uranium.

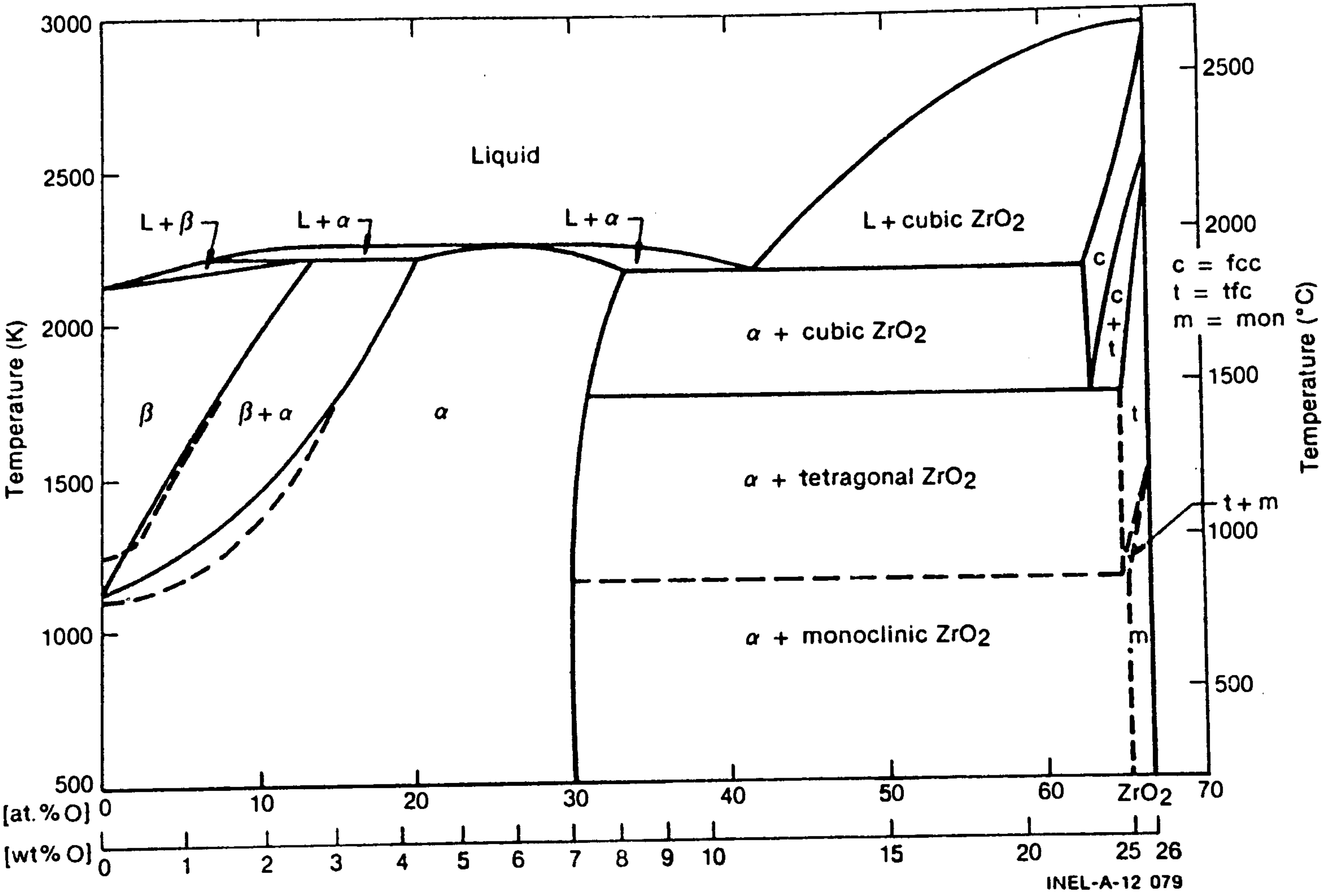

Figure 18. Zirconium-oxygen equilibrium phase diagram.

The two-phase [α-Zr(O)$_a$ + (U,Zr)] layer is made up of relatively small, radially elongated α-Zr(O) grains compared to the α-Zr(O)$_b$ layer [and α-Zr(O) in general] which is made up of large grains.[11-17]

The boundary between the [α-Zr(O)$_a$ + (U,Zr)] and (U,Zr) layers is distinct, but the interface between the (U,Zr) and α-Zr(O)$_b$ layers can be very irregular. The formation of large (U,Zr) globules within the α-Zr(O)$_b$ layers occurs only at temperatures greater than or equal to 1775 K; at lower temperatures, small spherical particles form.[12,13]

3.2.2.3 Interaction of UO_2 and Zircaloy. The UO_2 fuel and the zircaloy cladding comprise about 92% of the reactor core materials. Therefore, the interaction of these two materials with each other and with the steam is the most important phenomenon to be considered in evaluating the behavior of the core materials. The zircaloy cladding can begin to melt at 2030 K, while the UO_2 fuel does not melt until 3120 K; however, interaction of the Zr, UO_2, and steam results in materials with intermediate melting temperatures. The melting point of Zr increases with increasing oxygen content; the melting temperature of oxygen-saturated α-Zr(O) is about 2245 K. A eutectic interaction takes place between oxygen-saturated α-Zr(O) and UO_2 at about 2170 K (20 mole% UO_2), and a monotectic interaction at about 2670 K (85 mole% UO_2).[12] The UO_2 and ZrO_2 form a solid solution at high temperatures, and a 50/50 mole% composition melts at about 2809 K. Therefore, melting of the cladding and dissolution of the UO_2 fuel (liquefaction) can begin at temperatures as low as 2030 K. Other low- temperature eutectics may form between the fuel rod materials (Zr and UO_2) and other core structural materials (Inconel, stainless steel, and control rod materials).

The key to determining the peak temperatures reached and the possible scenario is the number and distribution of phases present in a prior molten material at room temperature. Neglecting effects of alloying elements, the observed phases should agree with the (U,Zr,O) ternary phase diagram. The ternary equilibrium phase diagrams of the (U-Zr-O) system at 1773 and

2273 K are shown in Figure 19. The equilibrium phases shown in the 1773 K diagram also are present at room temperature, because no further decomposition takes place at lower temperatures.

Interaction between UO_2 and Zr at 2273 K results in a single-phase homogeneous liquid or a two-phase (U,Zr,O) melt plus $(U,Zr)O_{2-x}$ solid (at >3.6-wt% oxygen). Upon cooling, the homogeneous melt will decompose into two metallic components: an α-Zr(O) phase containing some uranium and an (U,Zr) alloy containing little or no oxygen.[11,15,18]

The heterogeneous melt also decomposes on cooldown, with the solid $(U,Zr)O_{2-x}$ particles having low Zr content decomposing into stoichiometric $(U,Zr)O_2$ and a (U,Zr) alloy, and the (U,Zr,O) melt decomposing into α-Zr(O) and (U,Zr) alloy.

Because of the transient conditions, oxidation of the heterogeneous and homogeneous melts must be considered, as this affects the final microstructural appearance. If oxidation occurs after solidification, the α-Zr(O) will transform to ZrO_2 and the (U,Zr) alloy will transform to $(U,Zr)O_2$. Therefore, the homogeneous melt will transform from α-Zr(O) + (U,Zr) to ZrO_2 + $(U,Zr)O_2$, and the two phases should be distinguishable.

The molten material also may absorb oxygen while in the liquid state. As the oxygen content of the melt increases, the temperature must increase for the material to remain molten, or a $(U,Zr)O_2$ solid solution forms. Oxidation of the melt will result in a single-phase $(U,Zr)O_2$ solid solution. This material will no longer have the appearance of having been molten. Elongated grains will tend to form along the oxygen concentration and temperature gradients, and the material will generally contain few pores and be dense in appearance.

The ZrO_2 and UO_2 also can form a solid solution by diffusion at temperatures up to 2800 K and by mixing of molten oxides at higher temperatures. Figure 20 shows the ZrO_2-UO_2 binary phase diagram. The

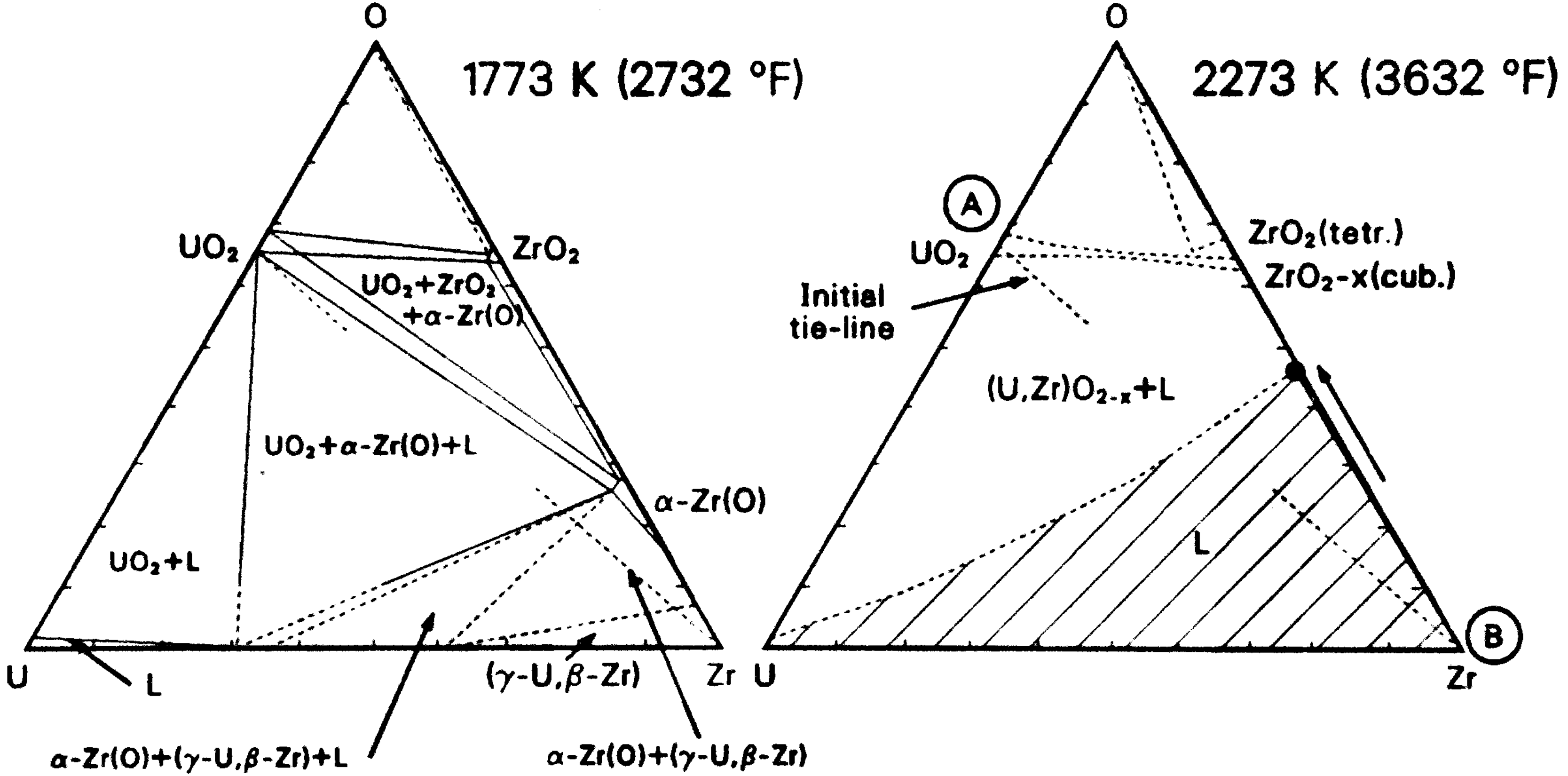
O
1773 K (2732 °F)
UO₂
ZrO₂
UO₂+ZrO₂ +α-Zr(O)
UO₂+α-Zr(O)+L
α-Zr(O)
UO₂+L
U
L
(γ-U,β-Zr)
Zr
α-Zr(O)+(γ-U,β-Zr)+L
α-Zr(O)+(γ-U,β-Zr)
O
2273 K (3632 °F)
A
UO₂
ZrO₂(tetr.)
ZrO₂-x(cub.)
Initial tie-line
(U,Zr)O₂₋ₓ+L
L
U
Zr
B

ALA84084-2B

Figure 19. U-Zr-O ternary phase diagrams for temperatures of 1773 and 2273 K.

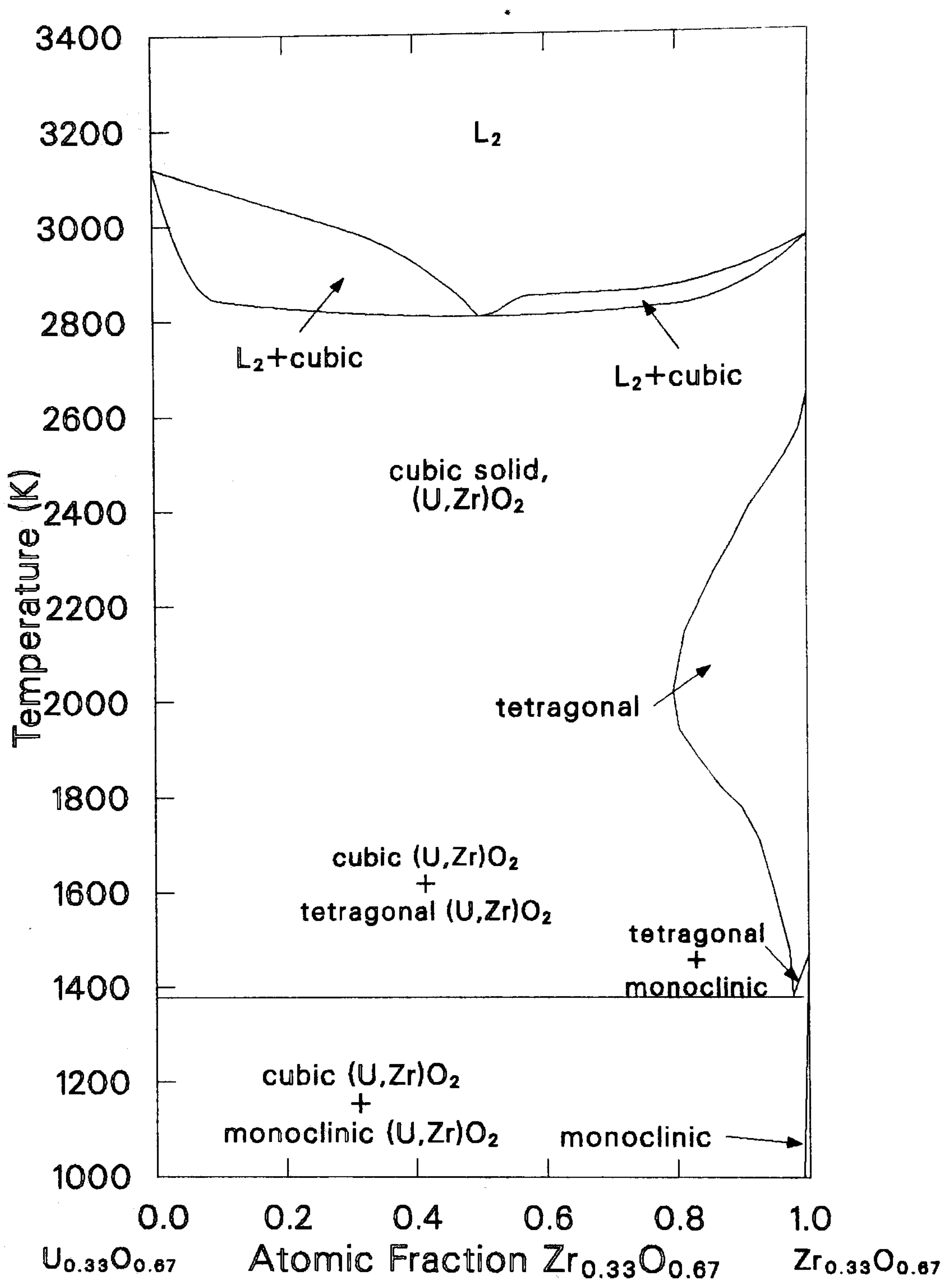

P145-ST-0112-01

Figure 20. UO_2-ZrO_2 binary phase diagram (solidus and liquidus curves represent preliminary data).

minimum melting point of the solid solution occurs at about the 50/50 mole% mixture. Only one phase is apparent on cooling of the $(U,Zr)O_2$ mixture. If this material has been molten, it will generally show structures such as large pores and irregular or nonexistent grain structure, usually associated with molten material.

The amount of interaction with other materials is another indication of whether the post-transient $(U,Zr)O_2$ solid solution is a metallic melt. If the metallic melt contacted a ceramic material (UO_2 or ZrO_2), dissolution of the ceramic should have occurred. A ceramic melt contacting a ceramic solid will show very little interaction.

3.2.2.4 Melting Temperature of Other Reactor Materials. Although the UO_2 fuel and zircaloy cladding comprise the major portion of the reactor core, the other reactor materials could play an important roll in fuel behavior. This is because the other reactor components have lower melting temperatures than the UO_2 fuel and many of these components can form eutectics with the fuel rod materials, thus, lowering fuel melting temperatures and changing physical properties. Table 8 presents the core material compositions along with the melting temperatures of the major constituents. The presence of prior molten control rod and structural materials in a particle would indicate peak temperatures of at least the melting point of that material. Unfortunately, phase diagrams do not exist for all possible combinations of the various reactor materials, and the effect of adding trace amounts of alloying elements on melting temperatures is not always quantified.

3.2.2.5 Temperature Estimate Results. The estimated peak temperatures for the 29 particles are listed in Table 7, along with other relevant data about each particle. These estimated temperatures are presented again in Table 9, along with comments about key indicators used for estimating the temperatures. These estimates are for the highest temperatures on the particle and may not represent those for the bulk of the particle. Only three of the particles examined do not contain molten Zr or Zr,U,O mixture. One of these is a prior molten Ag particle, and the

TABLE 8. CORE MATERIAL COMPOSITION

Material	Weight (kg)	Weight (%)	Melt Temperature (K)	Element	Weight Percent	Material	Weight (kg)	Weight (%)	Melt Temperature (K)	Element	Weight Percent
UO_2	93050	74.0	3120	^{235}U	2.265	Inconel-718	1211	1.0	1720	Ni	51.900
				^{238}U	85.882					Cr	19.000
				O	11.853					Fe	18.000
										Nb	5.553
										Mo	3.000
Zircaloy-4	23029	18.3	2030	Zr	97.907					Ti	0.800
				Sn	1.60					Al	0.600
				Fe	0.225					Co	0.470
				Cr	0.125					Si	0.200
				O	0.095					Mn	0.200
				C	0.0120					N	0.130
				N	0.0080					Cu	0.100
				HF	0.0078					C	0.040
				S	0.0035					S	0.007
				Al	0.0024						
				Ti	0.0020						
				V	0.0020						
				Mn	0.0020						
				Ni	0.0020	ZrO_2	331	0.3	2960	Zr	74.0
				Cu	0.0020					O	26.0
				W	0.0020						
				H	0.0013						
				Co	0.0010	Ag-In-Cd	2749	2.2	1050	Ag	80.0
				B	0.000033					In	15.0
				Cd	0.000025					Cd	5.0
				U	0.000020						
						$B_4C-Al_2O_3$	626	0.5		Al	34.33
Type 304 Unidentified stainless steel	3960	3.7	1720	Fe	68.635					O	30.53
				Cr	19.000					B	27.50
				Ni	9.000	Al_2O_3			2320	C	27.50
				Mn	2.000	B_4C			2620		
				Si	1.000						
				N	0.130	$Gd_2O_3-UO_2$	131.5	0.1		Gd	10.27
				C	0.080					U	77.72
				Co	0.080					O	12.01
				P	0.045						
				S	0.030	Gd_2O_3			3000		

Total Inventory = 125.8 metric tons

TABLE 9. PEAK TEMPERATURE ESTIMATES FOR PARTICLES FROM THE TMI-2 CORE DEBRIS GRAB SAMPLES

Particle	Temperature Range (K)	Comments
1A	2170-2245	No melting of UO_2 or ballooned α-Zr(O); eutectic Zr-U interaction.
1B	2170-2600	No melting of UO_2; slight grain growth; eutectic Zr-U interaction.
1E	2810-2960	No melting of ZrO_2; melting of α-Zr(O) cladding; prior molten $(U,Zr)O_2$.
1H	>2810	Dissolution of $(U,Zr)O_2$ by porous heterogeneous (U,Zr,O) melt.
3L	>2850	Above the liquidus temperature for (U,Zr,O) ceramic.
3M	>2850	Areas of $(U,Zr)O_2$ melt; contains trace Cr, Ni, Fe.
4A	∿2810	Foamy (U,Zr,O) molten ceramics contacting UO_2; may be slightly lower due to impurities.
4B	∿2810	Foamy (U,Zr,O) molten ceramic contacting UO_2 fuel; may be slightly lower due to impurities.
4D	>2850	Molten $(U,Zr)O_2$; dense.
5E	∿2810	Foamy (U,Zr,O) molten ceramic contacting fuel.
6B	<2245	No melting of α-Zr(O).
6C	2170-2960	No melting of ZrO_2; UO_2-Al_2O_3 eutectic interaction.

TABLE 9. (continued)

Particle	Temperature Range (K)	Comments
6D	2170-2810	No fuel melting; metallic (U,Zr,O) melt, oxidized to $(U,Zr)O_2$ by reducing oxidized fuel to UO_2.
6E	∿2000	Oxidized cladding fragment; no melting.
6F	2170-2810	Porous heterogeneous (U,Zr,O) melt attached to $(U,Zr)O_2$, ferromagnetic ingots.
7A	∿2810	Foamy (U,Zr,O) molten ceramic; may be lower due to impurities.
7B	2170-2245	No melting of UO_2 or α-Zr(O); eutectic U-Zr interaction.
7E	∿2810	Foamy (U,Zr,O) molten ceramic
8A	∿2810	Foamy (U,Zr,O) molten ceramic.
8C	>2170	Oxidized (U,Zr,O) melt.
8E	∿2810	Foamy (U,Zr,O) melt contacted later by metallic Zr melt.
8H	>2850	Areas of dense $(U,Zr)O_2$ melt containing trace Fe.
9D	∿2810	Foamy (U,Zr,O) ceramic melt.
9G	>1233	Molten Ag.
10A	∿3100	Areas of dense $(U,Zr)O_2$ melt with 5% ZrO_2.
10E	>2810	(U,Zr,O) ceramic melt on UO_2 fuel pellet.
10F	>2850	Regions of dense and foamy (U,Zr,O) melt.

TABLE 9. (continued)

Particle	Temperature Range (K)	Comments
11B	>2810	Foamy (U,Zr,O) melt.
11C	2170-3120	No melting of UO_2; small region of prior molten $(U,Zr)O_x$.

other two are sections of cladding oxidized to α-Zr(O) but not melted; therefore, phase changes occurring at low temperatures (<2030 K) in Zr could not be used as indicators.

Many of the particles examined contain UO_2 fuel, and usually the grain growth is minimal (maximum measured was 29 μm, with the original grain size being 10 μm). This indicates that much of the fuel probably remained at fairly low temperatures (<2000 K) during the accident or was exposed to high temperatures for only a short time. However, most of these particles also have areas of prior molten material, indicating large temperature gradients over very small distances. (The particles all are less than 4 mm in diameter.) The molten material relocated to a large extent and interacted both chemically and mechanically with the cooler materials.

The reader is reminded that the particles selected for detailed metallurgical examination were chosen either because they were representative of a basic particle type or because they were unique. They are not a statistical representation of the number of particles estimated to have experienced a given peak temperature. The particle type distribution shown in Table 6 (see Section 3.1.5) represents all of the larger particles in ten of the core debris grab samples and is more representative of the core debris. Based on this data and data from the detailed metallurgical examinations, it is estimated that about 80% of the debris material remained at fairly low temperature (<2000 K), with the other 20% experiencing temperatures up to fuel melting. This indicates a peak debris average temperature estimate of about 2200 K.

The key indicators used to estimate peak temperatures in the ranges of interest are shown in Figure 21. Most of the temperature estimates range between 2030 and 3120 K. The specific microstructures recognizable for materials exposed to temperatures in this range were discussed in Section 3.2.2.3. With some overlap, the particles examined fall into the following categories:

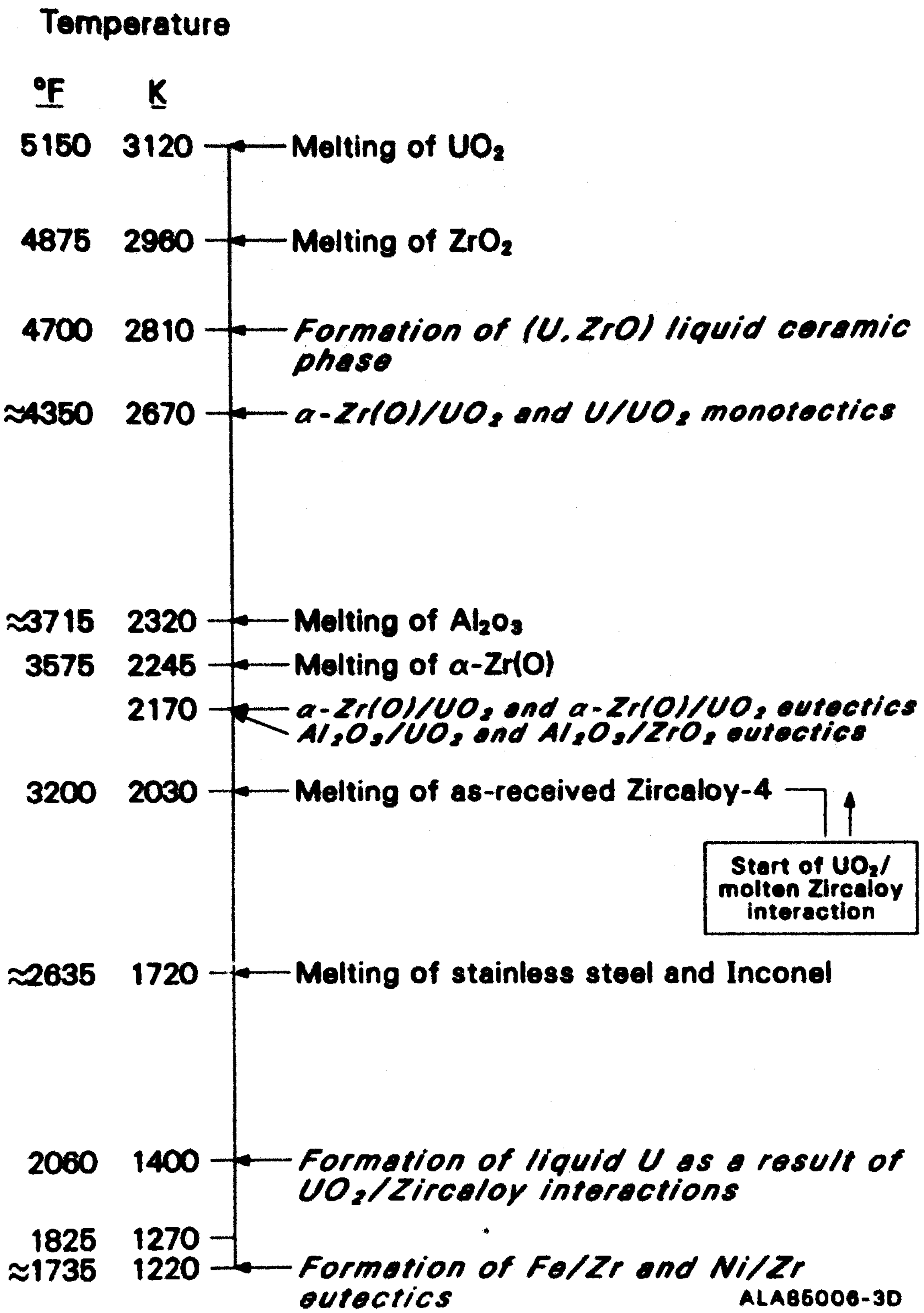
Temperature
°F
K
5150 3120 Melting of UO_2
4875 2960 Melting of ZrO_2
4700 2810 Formation of (U,ZrO) liquid ceramic phase
≈4350 2670 α-Zr(O)/UO_2 and U/UO_2 monotectics
≈3715 2320 Melting of Al_2O_3
3575 2245 Melting of α-Zr(O)
2170 α-Zr(O)/UO_2 and α-Zr(O)/UO_2 eutectics
Al_2O_3/UO_2 and Al_2O_3/ZrO_2 eutectics
3200 2030 Melting of as-received Zircaloy-4
Start of UO_2/ molten Zircaloy interaction
≈2635 1720 Melting of stainless steel and Inconel
2060 1400 Formation of liquid U as a result of UO_2/Zircaloy interactions
1825 1270
≈1735 1220 Formation of Fe/Zr and Ni/Zr eutectics
ALA85006-3D

Figure 21. Chemical interactions and formations of liquid phases in the UO_2-Zr system with increasing temperature.

- Some particles show a prior molten, metallic U-Zr-O mixture in contact with a UO_2 fuel pellet fragment. Therefore, the melt temperature before contact had to have been greater than 2170 K, the α-Zr(O) eutectic temperature. In some cases, an upper melt temperature limit can be determined, depending on behavior of other particle components. If a substantial metallic melt has flowed between ballooned cladding and fuel without melting the α-Zr(O) cladding, then the maximum melt temperature was less than 2245 K (Figure 22). Similarly, if a large metallic melt has surrounded a UO_2 fragment (dissolving a portion by eutectic decomposition) without melting any pure UO_2 by heat conduction, the maximum melt temperature would have been less than 3120 K. However, in many instances, the melt size is much smaller than the substrate material, in which case the large heat sink chilled the melt very quickly and no upper temperature limit can be established.

- One particle (Particle 6C) shows evidence of interaction with the Al_2O_3 poison rod material. A eutectic can form between UO_2-ZrO_2-Al_2O_3 at a temperature as low as 2170 K. This particle contains ZrO_2 which had not melted, indicating a temperature range of 2170 to 2960 K (Figure 23).

- Several particles show evidence of prior molten $(U,Zr)O_2$ ceramic, for which a minimum melting temperature of 2810 K has been established at KfK in the Federal Republic of Germany. At KfK, the melting temperature was found to increase only for compositions near UO_2 (melts at 3120 K) or ZrO_2 (melts at 2973 K). This work also demonstrated that a foamy structure with large voids is formed very near the melting point, but the $(U,Zr)O_2$ displays a much more dense structure upon exposure to temperatures above the liquidus (see Figure 20). Two of the particles in this category show dendritic freezing in the $(U,Zr)O_2$--separation of the UO_2-ZrO_2 homogeneous liquid into U-rich and Zr-rich phases--indicating slow cooling from

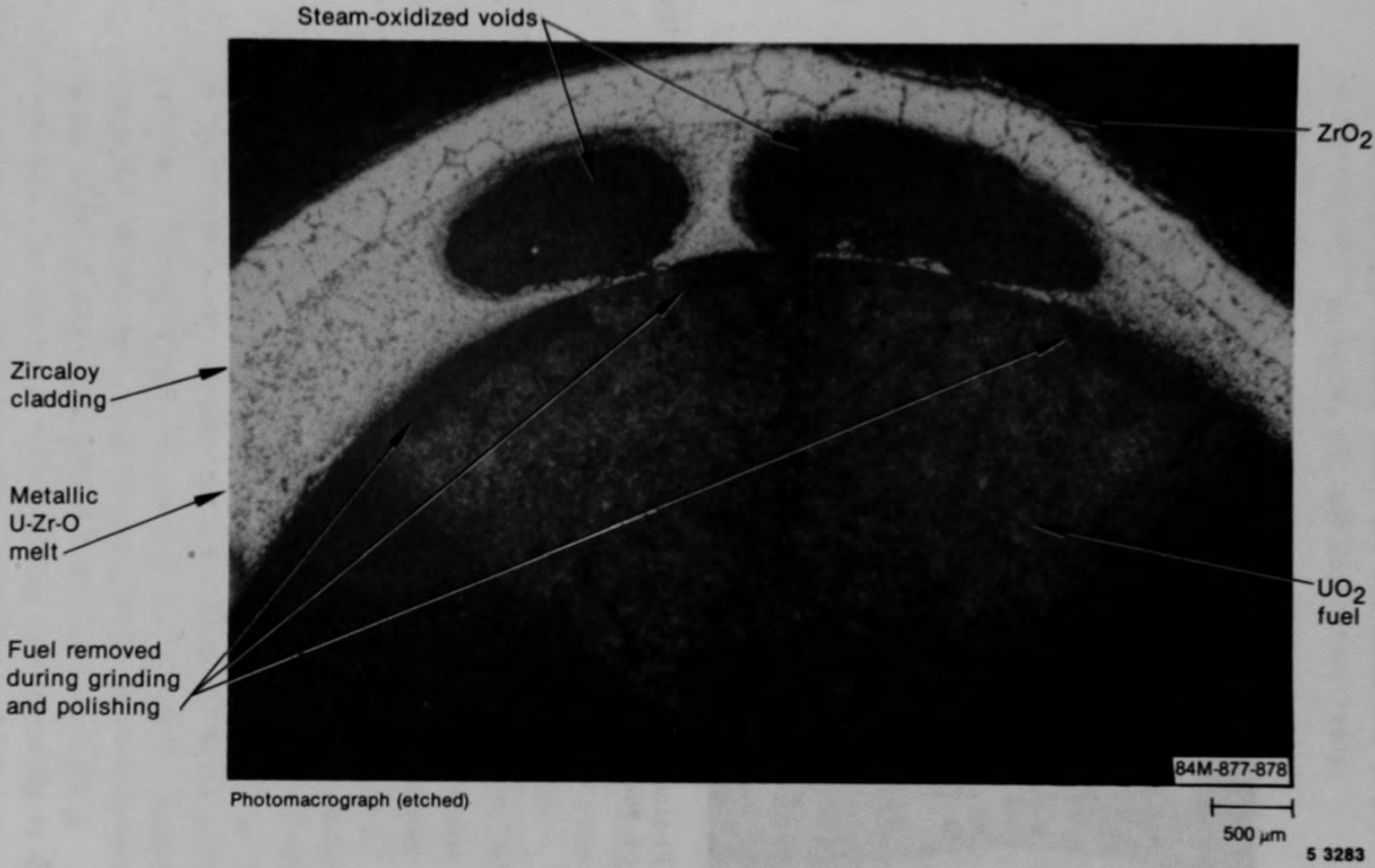
Steam-oxidized voids
ZrO$_2$
Zircaloy cladding
Metallic U-Zr-O melt
UO$_2$ fuel
Fuel removed during grinding and polishing
84M-877-878
Photomacrograph (etched)
500 μm
5 3283

Figure 22. Photomacrograph of Particle 1A (H8, surface) showing melt flow between UO$_2$ fuel and ballooned cladding.

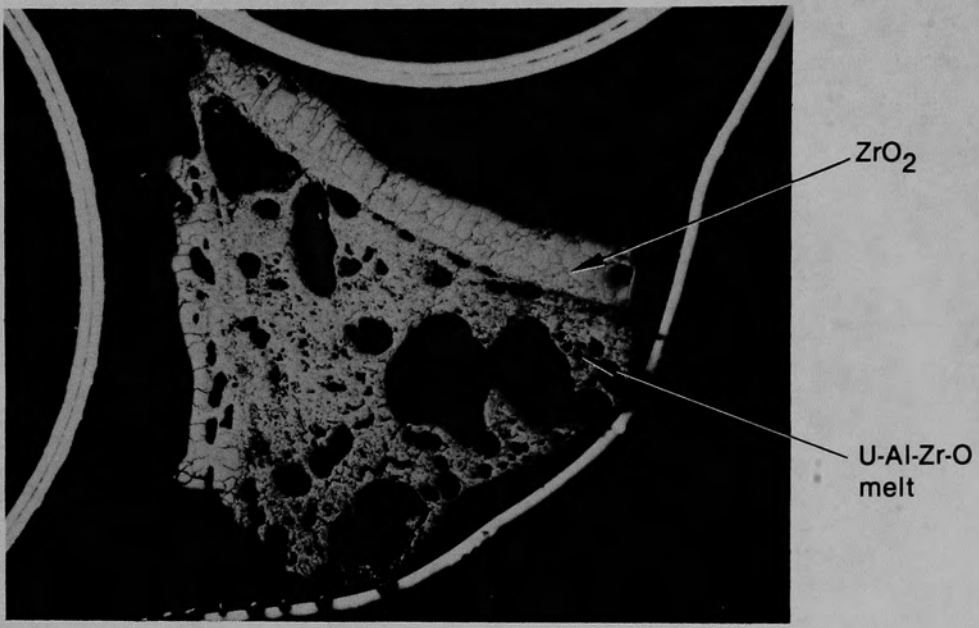
ZrO2
U-Al-Zr-O
melt

Figure 23. Photomacrograph of Particle 6C (E9, 56 cm) showing interaction of fuel rod materials with Al_2O_3.

above the liquidus. Examples of the foamy $(U,Zr)O_2$ structure, the dense, mixed ceramic melt, and the dendritic freezing are presented in Figures 24, 25, and 26, respectively.

- Particle 10A (Figure 27) also contains regions of prior molten $(U,Zr)O_2$, but a large part of this material contains slightly less than 2 atom% Zr (which corresponds to about 5-mole% ZrO_2). The small amount of Zr or other impurities indicates a liquidus or solidus temperature approaching UO_2 melting temperatures. There is a small central region of UO_2 that has been restructured but not melted. This particle appears to have been a piece of fuel that interacted with ZrO_2 near the UO_2 melting point. The prior molten ceramic material has a dense, almost glassy appearance, indicating temperatures somewhat above the liquidus temperature and then rapid cooling. No grain structure could be found outside of the central restructured zone, either during the optical examination using etches or during the SEM examination.

- Other particles contain considerable porosity that is not related to the foamy structure just discussed. As shown in Figure 28, the α-Zr(O)/UO_2 isopleth, when α-Zr(O) has dissolved appreciable amounts of UO_2 and when the melt is above 2673 K, the molten mixture is composed of two partially miscible liquids. Between 2673 and 2173 K, one liquid transforms to $(U,Zr)O_{2-x}$ solids, forming a slurry, while below 2173 K, the other liquid converts to α-Zr(O). Both the liquid mixture and the slurry display a strong tendency to chemically attach to UO_2, $(U,Zr)O_2$, and other solids. This wetting property is so dominant that, upon cooldown or quenching, shrinkage voids are created as the heterogeneous melt is pulled apart. Bubbles of gases and metal vapors also may contribute to void formation, though these pore sources have not yet been positively confirmed. In any case, heterogeneous melt porosity is typically irregular in configuration, with elongations, jagged edges, and

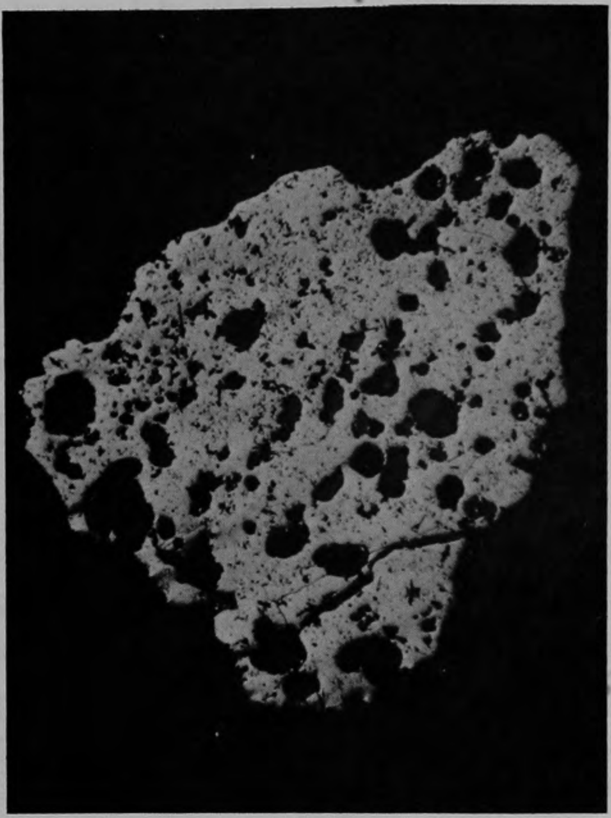

(a) Unetched

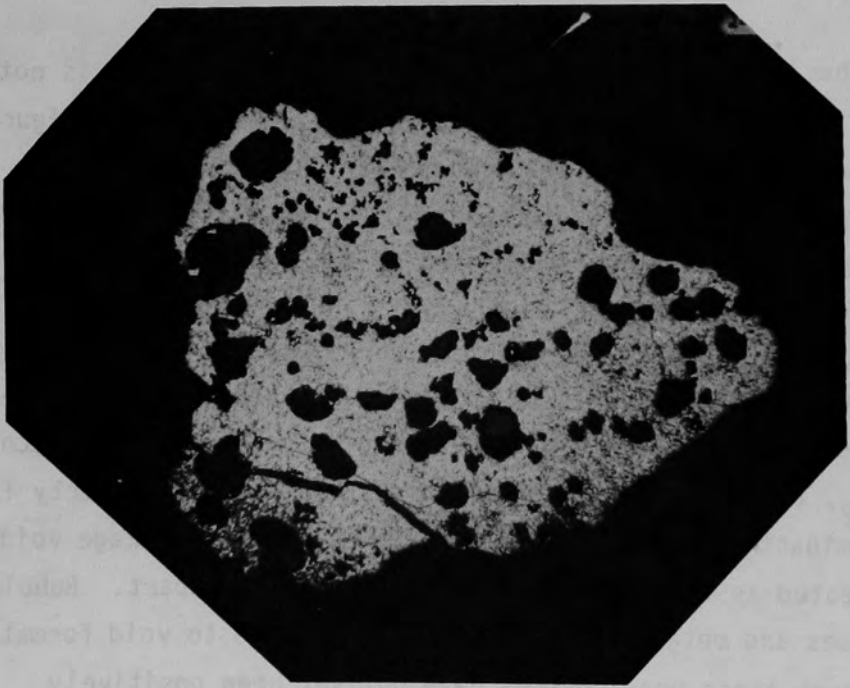

(b) Fuel etch

Figure 24. Photomacrograph of Particle 7A (H8, 36 cm) showing foamy U,Zr,O melt.

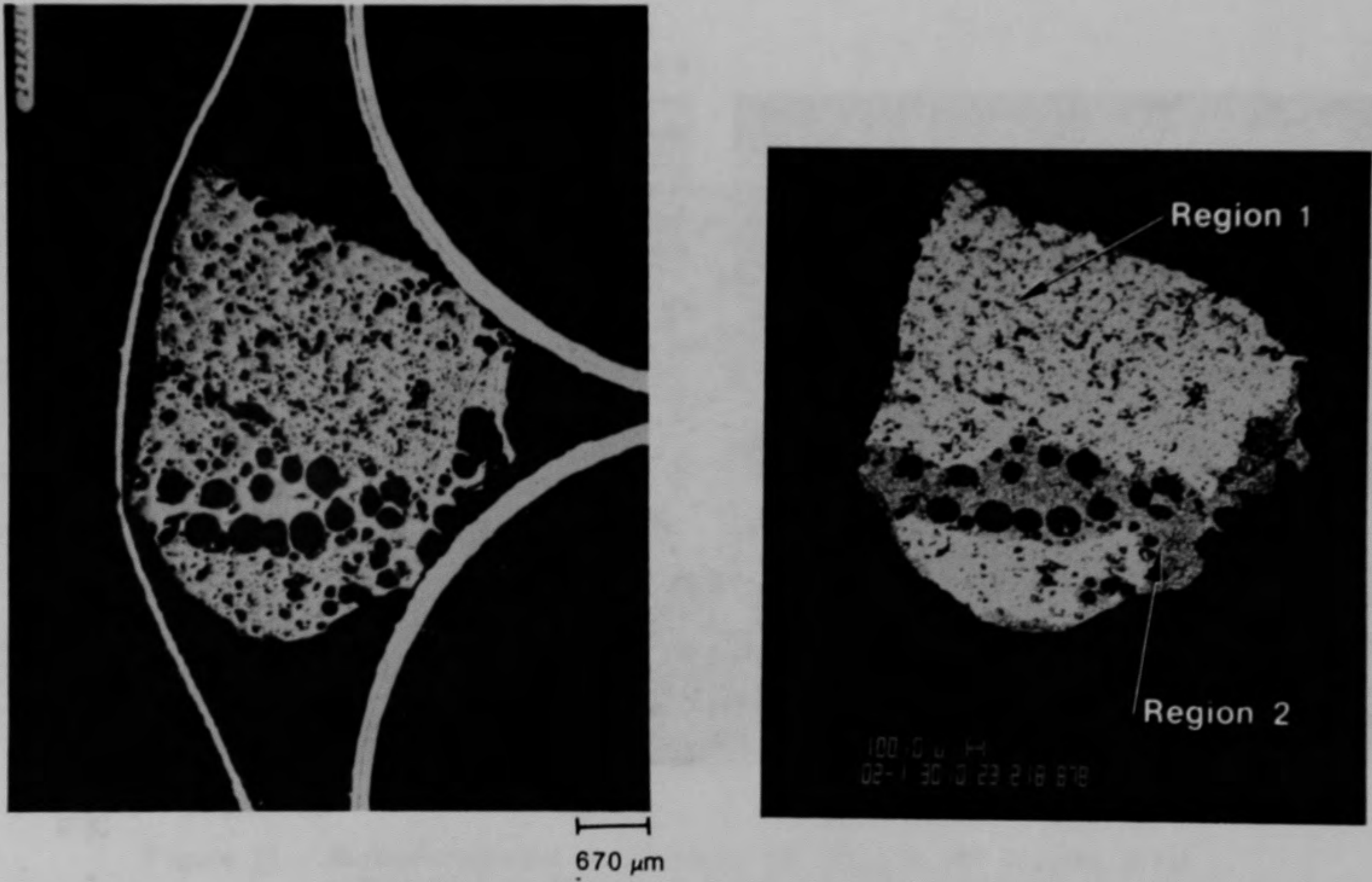
Region 1
Region 2
670 μm

Figure 25. Photographs of Particle 10F (E9, 74 cm) showing the presence of two distinct regions: Region 1 is dense U,Zr,O melt and Region 2 is foamy U,Zr,O melt.

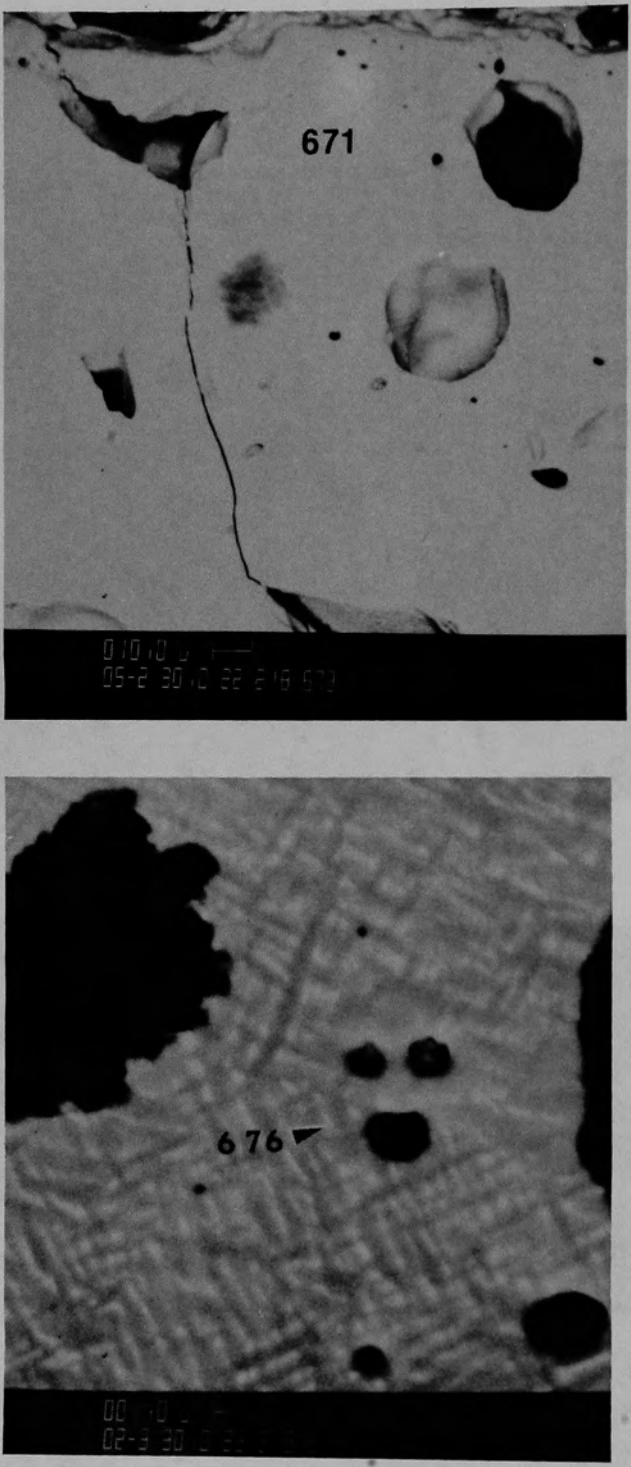

Figure 26. SEM back scattered electron image of Particle 3L (H8, 56 cm) showing dendritic freezing.

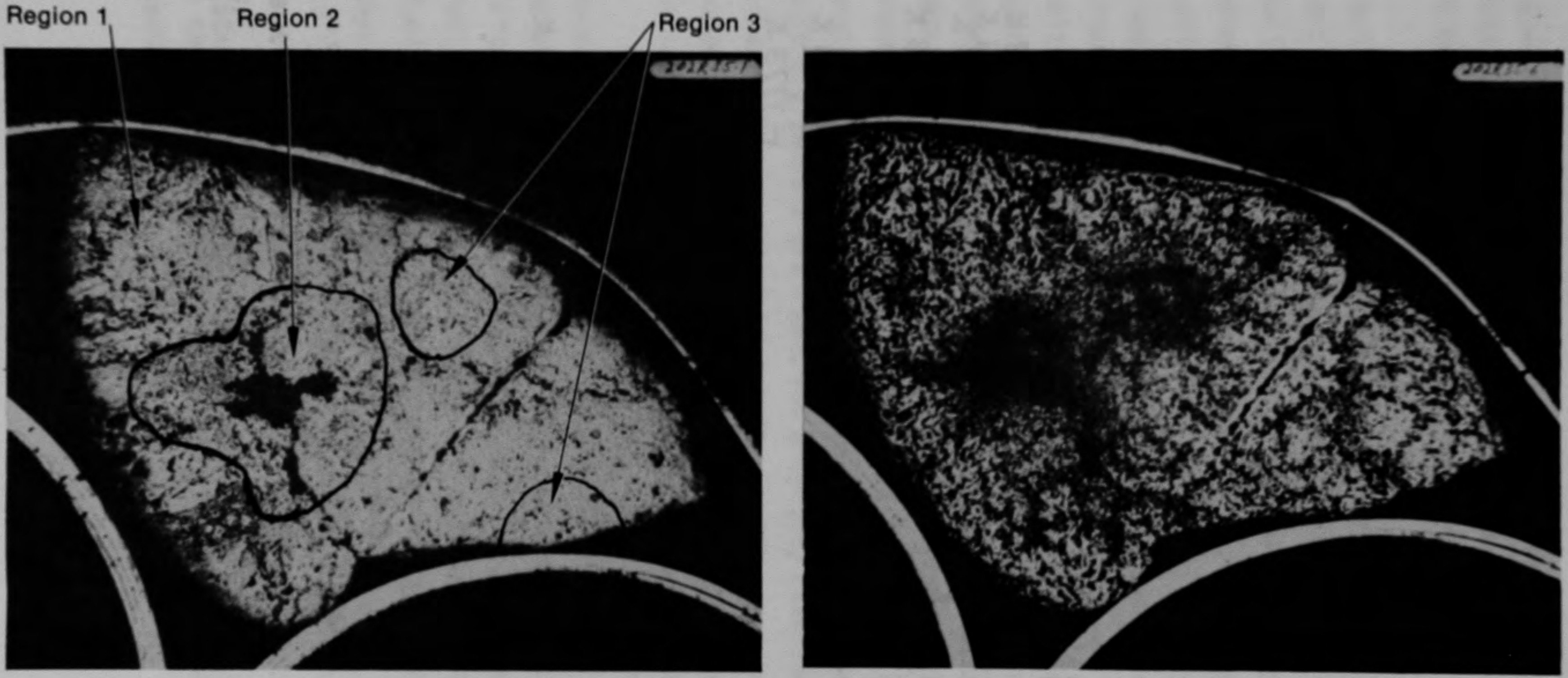
Region 1
Region 2
Region 3

(a) Unetched

(b) Etched

Figure 27. Photomicrographs of Particle 10A (E9, 74 cm) showing prior molten fuel in Regions 1 and 3. Region 2 is restructured, but not melted, UO_2.

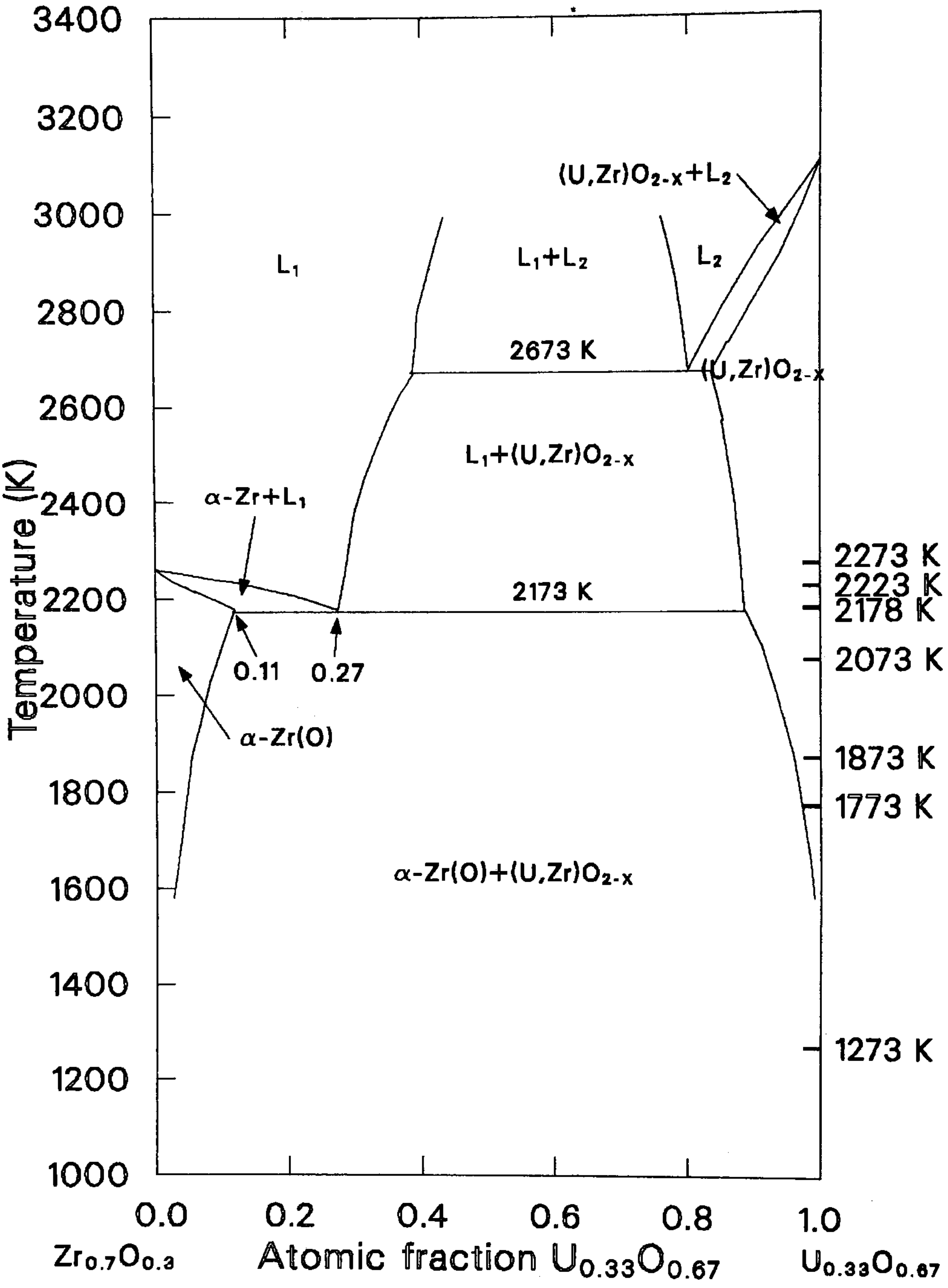

ALA85021-8

Figure 28. Quasi-binary α-Zr(O)/UO_2 phase diagram (Reference 20).

other features unlike the smooth spherical pores inside foamy material. One example of a porous, heterogeneous melt is shown at the base of Particle 6F in Figure 29.

- Particle 6F also, is representative of another broad category of particles that suggest occurrence of either multiple heatups during the TMI-2 transient or prolonged candling of molten material down the outsides of fuel rods, with intermittent solidification and oxidation of relocated droplets. The upper crown of Particle 6F is single-phase $(U,Zr)O_2$ that was formed either by ceramic melting or oxidation of a metallic (U,Zr,O) melt. In either case, the $(U,Zr)O_2$ solidified before being coated by the porous heterogeneous melt. The porous melt, in turn, solidified by cooling before being contacted by a Ni-rich metallic melt that created the three ferromagnetic ingots. On other particles, melt penetration is frequently observed along grain boundaries of previously solidified material. Both multiple temperature ramps and a lengthy candling sequence are plausible explanations, but this particle category definitely establishes that fuel liquefaction, relocation, and solidification did not occur within a single brief interval.

- As mentioned above, $(U,Zr)O_2$ regions can form by oxidation of metallic melts. Particle 6D shows an example of such material (Figure 30). A small amount of metallic melt contacted a large fuel pellet fragment, reducing the adjacent hyperstoichiometric fuel while the melt oxidized to single-phase $(U,Zr)O_2$. Note that $(U,Zr)O_2$ formed by this liquid-state oxidation mechanism is very difficult to distinguish from a rapidly cooled, superheated ceramic melt, unless the melt has coated fuel or ZrO_2. Whereas, a metallic melt must reduce the adjacent oxide, a ceramic melt could not alter the oxygen concentration of the coated substrate.

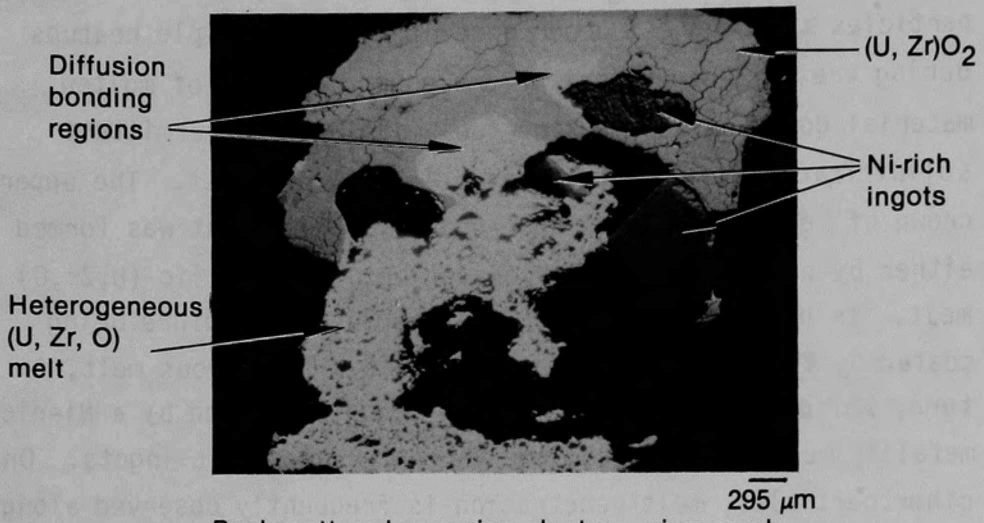
Diffusion bonding regions
(U, Zr)O2
Ni-rich ingots
Heterogeneous (U, Zr, O) melt
295 μm

Backscattered scanning electron micrograph

Figure 29. Particle 6F (E9, 56 cm) shows where solidified $(U,Zr)O_2$ was contacted by a porous melt that solidified before contact by a Ni-rich melt.

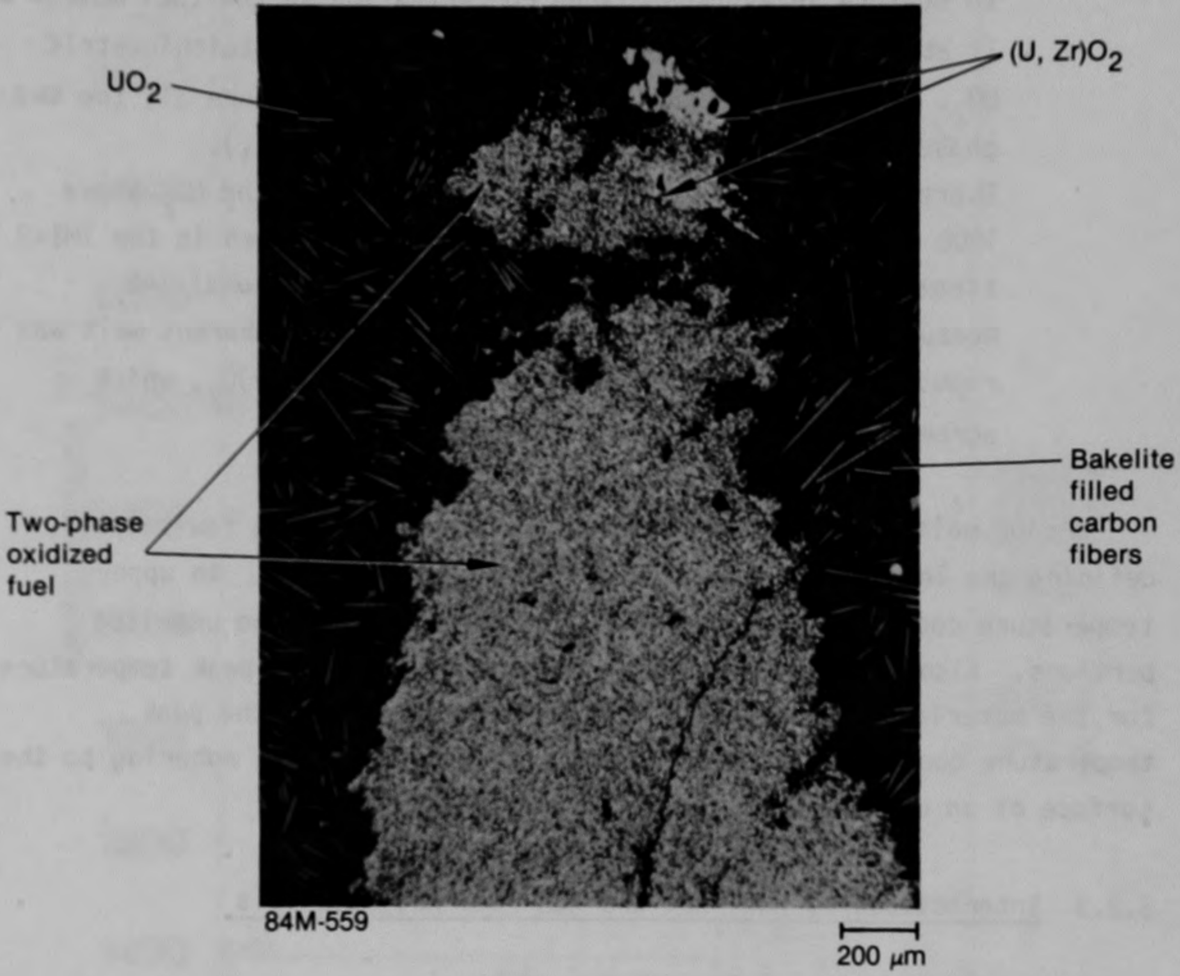
UO2
(U, Zr)O2
Bakelite filled carbon fibers
Two-phase oxidized fuel
84M-559
200 μm

Photomacrograph (unetched)

Figure 30. Particle 6D (E9, 56 cm) shows where the oxidized fuel mixture of U_4O_9 and U_5O_{13} have been reduced to UO_2 at one corner by contact with an initially metallic (U,Zr,O) melt.

- Particle 6D is also representative of those particles containing oxidized fuel. As detailed in Appendix C, a second fuel phase was exposed by etching this particle. Quantitative SAS was used to measure an average oxygen concentration in the fuel matrix of 71 at.%, which converts to $UO_{2.44}$--well above stoichiometric UO_2. According to the U-O phase diagram in Figure 31, the two phases are U_4O_9 and $UO_{2.6}$ (either U_5O_{13} or U_8O_{21}). Therefore, oxygen gas must have diffused into the UO_2 above 1900 K, although a likely source of excess oxygen in the TMI-2 steam flow has not yet been identified. Additional SAS measurements confirmed that fuel next to the adherent melt was reduced back to UO_2 while the melt became $(U,Zr)O_2$, which agrees with the results of the metallography.

Prior molten structural materials were observed in a few samples, defining the lower temperature range for those particles. An upper temperature could not be established for particles with no unmelted portions. Also, the temperatures quoted are the highest peak temperature for the materials that make up a given particle. Thus, the peak temperature quoted could be for a small layer of material adhering to the surface of an otherwise low temperature particle.

3.2.3 Interactions of Fuel Rod and Non-Fuel Rod Materials

The fuel rods, including UO_2 pellets and zircaloy cladding, made up about 92% of the original TMI-2 core inventory. The remaining 8% was structural and control material. Table 10 lists the core materials by elemental weight percent, excluding oxygen.

Most of the particles contain at least some traces of structural materials (Cr, Fe, and Ni), and in some cases structural materials are a significant part of the particle (see Particles 4A, 6C, 7A, or 8C in Appendix C). These materials are commonly found mixed intimately with prior molten fuel rod materials, primarily at grain boundaries or in voids. However, it was also common to find traces of Fe in the base

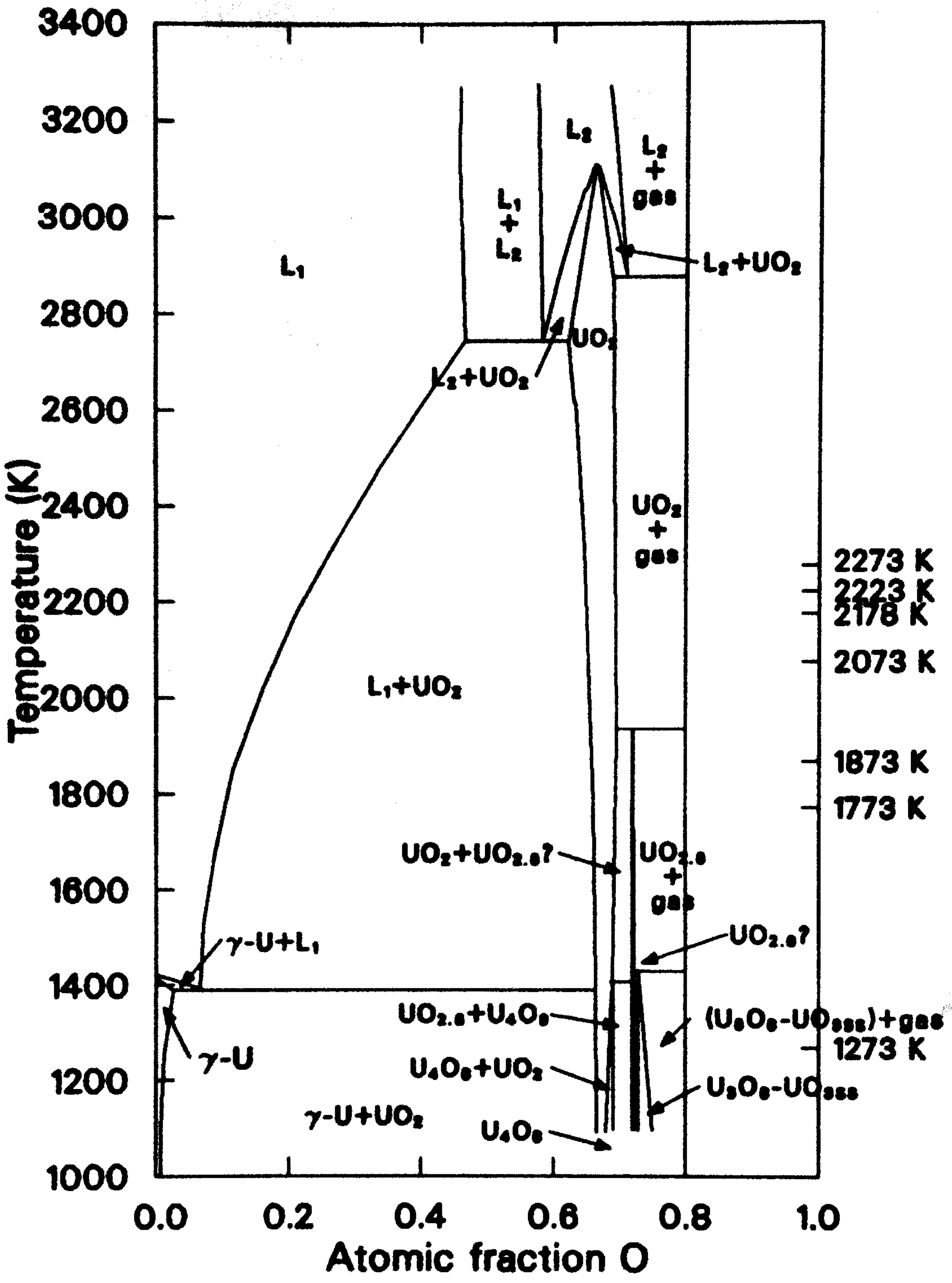

AI.A86021-5

Figure 31. Uranium-oxygen phase diagram (Reference 21).

TABLE 10. TMI-2 CORE COMPOSITION BY ELEMENTAL WEIGHT PERCENT

Element	Weight Percent
U	71.77
Zr	19.89
Fe	3.01
Ag	1.75
Cr	1.00
Ni	0.91
In	0.33
Sn	0.32
Al	0.18
B	0.14
Cd	0.12
Mn	0.09
Nb	0.05
Si	0.04
C	0.04
Mo	0.03
Gd	0.01
Ti	0.01
N	0.01
Co	0.01
S	<0.01
Ca	<0.01
P	<0.01
Hf	<0.01
V	<0.01
W	<0.01

material (see Table 7 for a listing of particles that contain Fe in the base material). The almost universal occurrence of structural material with prior molten fuel rod materials indicates that strong reactions took place between fuel and structural materials. These reactions have been observed by Hagen et al. in experiments with electrically heated fuel rods and Inconel grid spacers.[22]

Structural materials (Ni with small amounts of Fe) also were found in non-oxidized metallic form, mechanically bonded to fuel rod materials, as seen in Particle 11B. Ni alloyed with small amounts of Sn and occasionally fission products (Ru and Tc) was found scattered throughout many of the particles in small, round, metallic (non-oxidized) inclusions. It is possible for Ni to be separated from the other Inconel or stainless steel constituents through a membrane separation process, whereby the Fe and Cr preferentially diffuse into the solid $(U,Zr)O_2$. An example of this can be seen in Particle 7E, along an edge that contains many small regions of Ni surrounded by material high in Cr and Fe.

Control rod materials (Ag, In, and Cd) were not as commonly found as the structural materials. Ag was occasionally found, primarily in inclusions, and there were two minor occurrences of In and Cd. However, major portions of three particles (Particles 8H, 9D, and 9E) were metallic Ag containing Ni-Sn inclusions. Particle 9G was composed completely of the Ag material, and Particles 8H and 9D contained ceramic fuel rod material mechanically bonded to the Ag material. This lack of mixing with fuel rod materials is probably due to the early failure of the control rods, while the rest of the fuel rod bundle was still intact. In addition, eutectic interactions were probably inhibited by oxide layers.

The major source of Al in the core was from alumina-boron carbide (B_4C-Al_2O_3) burnable poison rods. Al also is a minor alloying element in Inconel, and there were other minor sources. However, Al was found with other structural materials in over half of the particles that contained structural materials. If the source of Al in these particles was Inconel, then there would have had to have been a segregation process at work concentrating the Al. However, if the source of Al was the poison rods, then there first would have had to have been eutectic interactions between Inconel grid spacers, zircaloy cladding, and alumina, causing liquefaction and flow, and then eventual interaction with fuel rods. Particle 6C contains exceptionally large amounts of Al, indicating a possible direct interaction with a poison rod. There are areas on this particle where positive elemental identification is not possible because of nonconductive properties, but there are indications that these areas are alumina.

3.3 Chemical Analyses

Elemental analysis was performed on the recombined bulk samples and particles and aliquots using ICP. The original elemental composition and total weights of principal components for the core and a control rod fuel assembly are presented in Table 11. The elements for which analysis was performed by ICP also are identified. The elements were selected for analysis to characterize the five groups of materials present in the core; uranium fuel and zircaloy cladding, Ag-In-Cd control rod materials, burnable poison rod materials(Al, Gd, and B), structural materials (stainless steel and Inconel), and Te.

The objectives of the elemental analysis include (a) characterizing the homogenity of the core debris bed, both axially (0 through 94 cm in depth) and radially [from the H8 (center) to the E9 (mid-radius) locations--a distance of ~70 cm], (b) determining the retention or release of highly volatile core materials (e.g., Ag-In-Cd), and (c) characterizing the relocation of core materials and Te.

Results of the chemical analysis as they relate to the present condition of the core and the accident scenario, are evaluated in Section 4.

TABLE 11. TMI-2 REACTOR CORE AND CONTROL ROD FUEL ASSEMBLY COMPOSITION[1]

Material (Weight)	Element	Weight Percent	Material	Element	Weight Percent
UO_2	U-235[a]	2.265	Inconel-718	Ni[a]	51.900
(93,050 kg)	U-238[a]	85.882	(1,211 kg)	Cr[a]	19.000
(526 kg)[b]	O	11.853	(6.8 kg)[b]	Fe[a]	18.000
				Nb	5.553
				Mo	3.000
Zircaloy-4	Zr[a]	97.907		Ti	0.800
(23,029 kg)	Sn[a]	1.60		Al[a]	0.600
(125 kg)[b]	Fe[a]	0.225		Co	0.470
	Cr[a]	0.125		Si[a]	0.200
	O	0.095		Mn[a]	0.200
	C	0.0120		N	0.130
	N	0.0080		Cu[a]	0.100
	Hf	0.0078		C	0.040
	S	0.0035		S	0.007
	Al[a]	0.0024			
	Ti	0.0020			
	V	0.0020	ZrO_2	Zr[a]	74.0
	Mn[a]	0.0020	(331 kg)	O	26.0
	Ni[a]	0.0020	(0 kg)		
	Cu[a]	0.0020			
	W	0.0020			
	H	0.0013	Ag-In-Cd	Ag[a]	80.0
	Co	0.0010	(2,749 kg)	In[a]	15.0
	B[a]	0.000033	(43.6 kg)[b]	Cd[a]	5.0
	Cd[a]	0.000025			
	U[a]	0.000020			
			$B_4C-Al_2O_3$	Al[a]	34.33
			(626 kg)	O	30.53
			(0 kg)[b]	B	27.50
Type 304	Fe[a]	68.635		C	7.64
stainless	Cr[a]	19.000			
steel	Ni[a]	9.000			
(676 kg) and	Mn[a]	2.000	$Gd_2O_3-UO_2$	Gd[a]	10.27
Unidentified	Si[a]	1.000	(131.5 kg)	U	77.72
stainless	N	0.130	(0 kg)[b]	O	12.01
steel	C	0.080			
(3,960 kg)	Co	0.080			
(16.8 kg)[b]	P	0.045			
	S	0.030			

---

a. Elements for which ICP analysis was performed.

b. Weight of material in a control rod fuel assembly.

3.3.1 Summary of Examinations

Results of the ICP elemental analysis for the recombined bulk samples are presented in Tables 12 and 13 . Results are presented in weight percent (wt%) of the dissolved material. Insoluble material weights are listed in Table E-12 (Appendix E). The insoluble material was less than 3% for any sample. The weight percents when added together do not equal 100%, because other elements expected to be present (e.g., oxygen) were not measurable by this method. The principal elemental components identified are U and Zr, with smaller amounts (generally <5 wt%) of other elements. The total uncertainty associated with the results of the elemental analysis of each recombined bulk sample is 10 to 15%. Factors contributing to the total uncertainty include (a) the presence of insoluble material, (b) ICP analysis uncertainty, (c) uncertainties associated with sample weight and volume measurements, and (d) presence of unmeasurable sample components.

Results of the elemental analysis of the particles and aliquots are contained Appendix D. The elements measured are the same as those shown in Tables 12 and 13 for the recombined bulk samples. The total uncertainty associated with the analysis of each particle and aliquot is generally 10 to 15%, because of the factors listed above. However, as noted in Appendix D, the total uncertainty for some particles and aliquots ranges from 30 to 50% because of the small (<10 mg) portions examined or sample losses incurred during the dissolution and analysis. Sample loss was determined by comparing the elemental U content obtained by ICP with results of the fissile/fertile material (^{235}U + ^{238}U) analysis performed on the intact particle or aliquot (Appendix E, Table E-11).

X-ray diffraction analysis was performed on some particles; however, due to problems associated with the technique (detailed in Appendix A), results were of limited value and, therefore, are not reported.

TABLE 12. ELEMENTAL CONTENT OF THE RECOMBINED BULK SAMPLES FROM THE H8 CORE LOCATION[a]
(wt%)

Element	Sample 1 (23.56 g)[b]	Sample 7 (44.62 g)[b]	Sample 3 (50.10 g)[b]	Samples 8 and 9[c] (94.6 g)[b]
Ag	1.6 E-1	1.9 E-1	1.5 E-1	1.6 E-1
Al	3.37	<4.6 E-2[d]	<4.8 E-2	<6.0 E-2
B	8.02 E-1	2.8 E-1	9.3 E-2	1.17
Cd	<5.9 E-3	<2.3 E-3	<2.4 E-3	<3.0 E-3
Cr	3.9 E-1	3.7 E-1	1.2 E-1	2.9 E-1
Cu	<1.5 E-2	5.7 E-3	1.2 E-2	7.6 E-3
Fe	1.19	1.17	5.0 E-1	9.9 E-1
Gd	8.2 E-2	5.7 E-2	5.8 E-2	5.7 E-2
In	<1.8 E-1	<6.9 E-2	<7.2 E-2	6.6 E-2
Mn	4.1 E-2	3.7 E-2	1.9 E-2	3.4 E-2
Mo	<5.9 E-2	<2.3 E-2	<2.4 E-2	<3.0 E-2
Ni	1.38	6.5 E-1	1.7 E-1	3.3 E-1
Nb	<1.8 E-1	1.6 E-1	1.7 E-1	1.7 E-1
Si[e]	3.84	3.63 E-1	1.39	2.8 E-1
Sn	<2.9 E-1	<1.1 E-1	<1.2 E-1	<1.1 E-1
Te	<1.2 E-1	<4.6 E-2	<4.8 E-2	<4.6 E-2
U	7.03 E+1	7.39 E+1	7.25 E+1	7.23 E+1
Zr	1.59 E+1	1.76 E+1	8.24	1.42 E+1

---

a. In order of depth into the debris bed.

b. Weight of sample material dissolved.

c. Samples 8 and 9 were combined, as they had been mixed during dissolution.

d. Less than (<) values are the lower limit of detection for the sample analyzed.

e. Silicon contamination from the glassware occurred during the dissolution process.

TABLE 13. ELEMENTAL CONTENT OF THE RECOMBINED BULK SAMPLES FROM THE E9 CORE LOCATION[a] (wt%)

Element	Sample 4 (5.11 g)[b]	Sample 5 (16.64 g)[b]	Sample 6 (45.97 g)[b]	Sample 10 (57.44 g)[b]	Sample 11 (42.54 g)[b]
Ag	1.5 E-1	5.4 E-2	1.4 E-1	1.3 E-1	1.9 E-1
Al	1.1	<6.7 E-2[c]	<7.7 E-2	<2.8 E-2	<7.2 E-2
B	3.00	1.4 E-1	1.6 E-1	1.70 E-1	<5.4 E-2
Cd	<2.1 E-2	<3.4 E-3	<3.9 E-3	<1.4 E-3	<3.6 E-3
Cr	<6.3 E-2	9.4 E-2	1.0 E-1	1.45 E-1	2.1 E-1
Cu	<5.3 E-2	<8.4 E-3	<9.7 E-3	5.6 E-3	<8.9 E-3
Fe	5.1 E-1	2.1 E-1	3.3 E-1	4.33 E-1	8.3 E-1
Gd	<1.5 E-1	4.7 E-2	5.4 E-2	5.6 E-2	<2.5 E-2
In	<6.3 E-1	<1.0 E-1	<1.2 E-1	<4.3 E-2	<1.1 E-1
Mn	2.1 E-1	1.4 E-2	1.6 E-2	1.4 E-2	2.1 E-2
Mo	<2.1 E-2	<3.4 E-2	<3.9 E-2	<1.4 E-2	<3.6 E-2
Ni	<1.1 E-1	2.7 E-1	2.4 E-1	2.55 E-1	3.9 E-1
Nb	<6.3 E-1	<1.0 E-1	2.7 E-1	9.8 E-2	<1.1 E-1
Si[d]	2.20 E+1	5.0 E-2	1.36	2.49 E-1	3.9 E-1
Sn	<1.1	<1.7 E-1	<1.9 E-1	1.4 E-1	<1.8 E-1
Te	<4.2 E-1	<6.7 E-2	<7.7 E-2	<2.8 E-2	<7.2 E-2
U	8.32 E+1	8.31 E+1	7.08 E+1	7.34 E+1	7.76 E+1
Zr	1.14 E+1	4.31	8.25	7.19	9.69

---

a. In order of depth into the debris bed.

b. Weight of sample material dissolved.

c. Less than (<) values are the lower limit of detection for the sample analyzed.

d. Silicon contamination from the glassware occurred during the dissolution process.

3.3.2 Chemical Composition of the Core Debris

Although individual particles of the core debris are quite heterogeneous on a microstructural scale, as discussed in Section 3.2, the composition of the debris bed is principally a mixture of U and Zr, with lesser amounts of other elements, similar to that listed in Table 11. The average elemental concentrations measured for the recombined bulk samples were used to characterize the homogeneity of the debris bed; results of the particle and aliquot analysis provide indications of the homogeneity of individual particles, or aliquots. Retention and release of volatile components (e.g., Ag-In-Cd) was estimated by comparing measured elemental concentrations with their original concentrations in the fuel assembly (see Table 11). Evidence of relocation of core components was determined by the wide distribution of less abundant constituents (e.g., Gd) in the debris bed.

Evaluation of the elemental analysis results is divided into characterization of the elemental constituents of the five principal groups of materials present in the core: (a) uranium fuel and zircaloy cladding, (b) Ag-In-Cd control rod materials, (c) burnable poison rod materials (B_4C-Al_2O_3 and Gd_2O_3-UO_2), (d) structural materials (stainless steel and Inconel), and (e) tellurium (the elemental analysis is used to evaluate the behavior of fission product Te).

3.3.2.1 Uranium and Zirconium. The reactor core is composed principally of U (82,000 kg) and Zr (22,500 kg). These elements account for approximately 84% of the total core weight. Table 14 lists the U and Zr concentrations (wt%) and Zr/U ratios for the ten recombined bulk samples. Relatively consistent U concentrations (±7%) and varying Zr/U ratios (i.e., varying Zr concentrations) are apparent. At the H8 location, the elemental concentrations and Zr/U ratios near the surface of the debris bed and at 36 cm into the debris bed are similar. Also, the Zr/U ratios are similar to those initially found in a control rod fuel assembly (i.e., 0.26). At 56 cm into the debris bed (Sample 3), the concentration of U is similar to the concentrations higher in the debris bed; however, the Zr/U

TABLE 14. URANIUM AND ZIRCONIUM CONCENTRATIONS AND ZR/U RATIOS FOR THE RECOMBINED BULK SAMPLES

Sample	Depth into Debris Bed (cm)	Uranium Concentration[a] (wt%)	Zirconium Concentration[b] (wt%)	Zr/U Ratio[c]
H8 Samples				
1	0	70	16	0.23
7	36	74	18	0.24
3	56	72	8.2	0.11
8 and 9	70 and 77	72	14	0.20
E9 Samples				
4	0	83	11	0.14
5	8	83	4.3	0.05
6	56	71	8.2	0.12
10	74	73	7.2	0.10
11	94	78	9.7	0.12

---

a. Initial U concentration in the core was 65 wt%, in a control rod fuel assembly 64 wt%, and in a fuel rod 71 wt%.

b. Initial Zr concentration in the core was 18 wt%, in a control rod fuel assembly 17 wt%, and in a fuel rod 18 wt%.

c. The Zr/U ratios for a control rod fuel assembly and the core are 0.26 and 0.27, respectively. A fuel rod has a ratio of 0.25.

ratio is approximately half of the ratios for the core and fuel rods, suggesting depletion (~58%) of Zr has occurred at this depth. The Zr depletion is probably caused by melting and relocation. The results are evaluated as they relate to the condition of the core in Section 4.3. The concentrations and ratios for the combined Samples 8 and 9 are similar to those obtained near the surface of the debris bed.

At the E9 location, U concentrations near the surface are approximately 18% higher than deeper into the debris bed. The higher concentration near the surface suggests that principally fuel material with lesser amounts of associated Zr are present. The Zr/U ratios at the E9 location range from 0.14 to 0.05, indicating depletion of Zr by 46 to 80%. There is significant depletion of Zr at all depths at the E9 location, whereas only one sample from H8 (Sample 3) showed significant Zr depletion. The data indicate that significant Zr depletion has occurred in the debris bed and that this depletion is greater at the mid-radius location than at the core center.

Tables 15 and 16 summarize from Appendix D the weight percent of U present in each particle and aliquot. Tables 17 and 18 list the Zr/U ratios for particles and aliquots obtained from the H8 and E9 samples, respectively. The results for the particles and aliquots show a much wider range of U concentrations (0 to ~100% U) than do the recombined bulk samples (70 to 80% U), partly because the particles were chosen for specific characteristics (e.g. cladding, fuel pellet, etc.). Observations concerning these results and their significance are as follows:

- o Few particles are completely U or Zr. The results indicate that little U is present without significant amounts of associated Zr. Little intact fuel material (88% U in UO_2 fuel or 71% U in a fuel rod) is present, and significant disruption of fuel rods is indicated.

- o Higher concentrations of Zr are present in the smaller particle size fractions, with a maximum Zr/U atom ratio of approximately 1:2.5 for the smallest ($\leq$30 μm) particle sizes. This

TABLE 15. URANIUM CONTENT OF PARTICLES AND ALIQUOTS FROM THE H8 CORE LOCATION[a] (wt%)

Particle Size Fraction (μm)	Particle/Aliquot	Sample 1	Sample 7	Sample 3	Sample 8	Sample 9
>4000	A	--[b]	59	38	72	40
>4000	B	83	--[b]	0	81	55
>4000	C	9.8	--[b]	--[b]	∿100[d]	78
>4000	D	26	--[b]	48	--[b]	11
>4000	E	17.8	--[b]	72	∿100[d]	72
1680-4000	F	57	72	∿100[d]	55	67
1680-4000	G	57	52	29	12	13
1680-4000	H	47	52	45	69	42
1000-1680	I	0	--[b]	56	22	14
1000-1680	J	64	40	11	63	45
1000-1680	K	57	68	48	81	--[b]
707-1000	Aliquot	52	37	58	28	51
297-707	Aliquot	53	35	42	42	--[b]
149-297	Aliquot	45	--[b]	37	32	67
74-149	Aliquot	41	52	35	48	34
30-74	Aliquot	36	--[b]	32	43	34
20-30	Aliquot	--[c]	19	--[b]	--[b]	17
<20	Aliquot	--[c]			49	50

---

a. In order of depth into the debris bed.

b. Not reported because of analysis problems.

c. Not analyzed.

d. The analysis results indicate the presence of other components. Also the uncertainty is large for these analyses indicating that this is oxidized uranium.

TABLE 16. URANIUM CONTENT OF PARTICLES AND ALIQUOTS FROM THE E9 CORE LOCATION[a] (wt%)

Particle Size Fraction (μm)	Particle/Aliquot	Sample 4	Sample 5	Sample 6	Sample 10	Sample 11
>4000	A	94	62	~100[b]	--[c]	~100[b]
>4000	B	58	85	0	88	--[c]
>4000	C	51	57	0	71	~100[b]
>4000	D	--[c]	90	8.1	61	~100[b]
>4000	E	88	--[c]	0	65	56
1680-4000	F	--	--[c]	0	63	82
1680-4000	G	--	--[c]	90	81	~100[b]
1680-4000	H	--	--[c]	71	68	--[c]
1000-1680	I	--	17	11	35	71
1000-1680	J	--	--[c]	13	54	63
1000-1680	K	--	--[c]	70	~100[b]	96
707-1000	Aliquot	--	31	55	64	14
297-707	Aliquot	--	--	44	38	--[d]
149-297	Aliquot	--	--	31	33	71
74-149	Aliquot	--	--	32	17	40
30-74	Aliquot	--	--	28	37	34
20-30	Aliquot	--	--	--	47	22
<20	Aliquot	--	--	--	--	~100[b]

---

a. In order of depth into the debris bed.

b. The analysis results indicate the presence of other components. Also, the uncertainty is large for these analyses, indicating that this is oxidized uranium.

c. Not reported because of analysis problems.

d. Not analyzed.

TABLE 17. ZR/U CONCENTRATION RATIOS OF PARTICLES AND ALIQUOTS FROM THE H8 CORE LOCATION[a]

Particle Size Fraction (µm)	Particle/Aliquot	Sample 1	Sample 7	Sample 3	Sample 8	Sample 9
>4000	A	--[b]	2.2 E-1	6.0 E-2	1.1 E-1	1.5 E-1
>4000	B	1.5 E-2	--[b]	--[c]	9.8 E-2	4.4 E-1
>4000	C	1.5 E-1	--[b]	--[b]	5.7 E-1	6.6 E-2
>4000	D	6.1 E-2	--[b]	2.0 E-2	--[b]	6.7 E-1
>4000	E	3.7	--[b]	3.2 E-2	5.1 E-1	8.7 E-1
1680-4000	F	2.4 E-1	4.3 E-2	5.1 E-2	5.4 E-1	2.9 E-1
1680-4000	G	2.4 E-1	2.6 E-1	1.4 E-1	8.0 E-1	4.3 E-2
1680-4000	H	7.8 E-1	7.4 E-3	2.2 E-1	1.2 E-1	1.2 E-1
1000-1680	I	--[c]	--[b]	1.5 E-1	2.2 E-1	2.0
1000-1680	J	2.3 E-1	6.2 E-2	2.4	7.9 E-1	1.2 E-1
1000-1680	K	2.3 E-1	2.1 E-1	1.9	2.5 E-1	--[b]
707-1000	Aliquot	2.3 E-1	2.3 E-1	3.4 E-1	1.1	1.18
297-707	Aliquot	1.9 E-1	7.2 E-1	1.9 E-1	9.3 E-2	--[b]
149-297	Aliquot	3.2 E-1	--[b]	4.7 E-2	5.8 E-1	5.4 E-1
74-149	Aliquot	7.3 E-1	8.4 E-1	9.2 E-1	5.4 E-1	4.4 E-1
30-74	Aliquot	7.9 E-1	--[b]	1.1	6.4 E-1	5.8 E-1
<30	Aliquot	9.3 E-1	--[d]	--[b]	--[d]	--[d]
20-30	Aliquot	--[d]	9.2 E-1	--[d]	--[b]	5.4 E-1
<20	Aliquot	--[d]	--[d]	2.7 E-1	--[d]	2.9 E-1

---

a. In order of depth into the debris bed.

b. Not reported because of analysis problems.

c. All zirconium or uranium; the other element was not detected.

d. No particle size analysis was performed for this size group.

TABLE 18. ZR/U CONCENTRATION RATIOS OF PARTICLES AND ALIQUOTS FROM THE E9 CORE LOCATION[a]

Particle Size Fraction (μm)	Particle/Aliquot	Sample 4	Sample 5	Sample 6	Sample 10	Sample 11
>4000	A	1.4 E-1	1.4 E-1	2.4 E-2	--[b]	8.5 E-2
>4000	B	3.1 E-2	4.9 E-2	--[c]	7.8 E-2	--[b]
>4000	C	2.4 E-2	6.8 E-2	--[b]	4.6 E-3	4.5 E-3
>4000	D	--[b]	4.6 E-3	1.0 E-2	4.4 E-3	1.8 E-2
>4000	E	3.0 E-2	--[b]	--[c]	1.2 E-1	5.4 E-3
1680-4000	F	--[a]	--[b]	--[c]	6.3 E-1	1.1 E-1
1680-4000	G	--	--[b]	5.5 E-3	4.6 E-3	3.0 E-3
1680-4000	H	--	--[b]	5.8 E-3	5.7 E-2	--[b]
1000-1680	I	--	4.9 E-1	2.0	6.8 E-2	3.0 E-1
1000-1680	J	--	--[b]	4.2	1.6 E-1	3.2 E-3
1000-1680	K	--	--[b]	1.1 E-1	5.8 E-3	3.1 E-3
<1000	Aliquot	--	9.2 E-2	--	--	--
707-1000	Aliquot	--	--	2.8 E-1	3.3 E-1	4.2
297-707	Aliquot	--	--	3.9 E-1	1.7 E-1	--[b]
149-297	Aliquot	--	--	2.1 E-1	6.8 E-1	1.8
74-149	Aliquot	--	--	1.0	7.4 E-1	9.7 E-1
30-74	Aliquot	--	--	1.0	4.4 E-1	1.4
<30	Aliquot	--	--	--[d]	--[d]	--
20-30	Aliquot	--	--	--	3.3 E-1	1.9

---

a. In order of depth into the debris bed.

b. Not reported because of analysis problems.

c. All zirconium; no uranium was detected.

d. No particle size analysis was performed for smaller sizes.

observation is consistent with previously reported results characterizing debris from fuel damage tests in the Power Burst Facility reactor of INEL.[23] The higher concentrations of Zr are probably due to fragmentation of the zircaloy cladding remnants and increasing oxygen content (oxidation) for the smaller particle sizes. The Zr/U atom ratios range from 1:7 to 1:2.5. An increase in Zr/U ratio with diminishing particle size is apparent in samples to a depth of 56 cm (Sample 3) at the H8 location (see Table 17). No measurable correlation between the Zr content and particle size is evident below this depth. The Zr content in the E9 samples (see Table 18) shows a particle size dependency which extends through 94 cm into the debris bed (Sample 11). The only exception is Sample 10 (E9, 74 cm), where the Zr content is about the same for all particle size fractions.

3.3.2.2 Control Rod Materials (Ag-In-Cd). The Ag-In-Cd control rod materials (2749 kg) account for approximately 2.2 wt% of the core weight. They are important because they are highly volatile and likely to vaporize and condense into aerosols, a principal mode for transport from the core to the reactor coolant system. The three constituents of the control rods, in their relative order of volatility (most volatile to least volatile), are Cd, In, and Ag.

Tables 12 and 13 summarize the elemental analysis results for Ag, In, and Cd in the recombined bulk samples. Of these elements, only Ag was measurable in the recombined bulk samples. The measured Ag concentrations are generally similar for both the H8 and E9 samples, ranging from 0.13 to 0.19 wt%. This suggests a relatively homogeneous distribution in the rubble bed. These concentrations are equivalent to 7.4 to 10% of the expected Ag concentration of the core. Therefore significant relocation of the Ag out of the debris bed has occurred.

The particle and aliquot data also indicate that Ag is relatively evenly distributed (0.1 to 0.2 wt%) at the sampled locations, with some localized areas of higher concentrations. The higher concentrations in the smaller particle sizes suggest Ag may be present primarily as relatively small nodules or localized accumulations.

Although Cd and In were not measurable in the recombined bulk samples, they were measurable in many of the particles and aliquots (see Appendix D) because of a lower detection limit associated with the sample size analyzed. Where measurable, Cd and In concentrations are generally higher (0.3 to 0.8 wt%) than Ag. The original concentration of In in a control rod fuel assembly is approximately 0.9 wt%. The data indicate that In is present in quantities similar to the original concentrations in some particles, suggesting it was retained as localized accumulations or nodules. The number of samples where In was not measurable may be due to the ICP detection limit for In, which is approximately a factor of four higher than the limit for Ag (up to 0.6 wt% for these samples).

Cd was measurable in a larger fraction of the total number of samples than In, but in fewer than was Ag. The samples with measurable amounts of Cd are principally particle size fractions less than 1000 μm. The smallest size fractions have the highest Cd concentrations (0.2 to 0.5 wt%). The concentration of Cd in a control rod fuel assembly is approximately 0.3 wt%. The data suggest Cd retention is similar to In.

No correlation between concentrations of the three control rod constituents is apparent for the particles and aliquots. The higher concentrations of In and Cd suggest that these elements are forming accumulations in the core. For the smaller (≤707 μm) particle size fractions, there is an increase in concentrations for control rod constituents with decreasing particle size. The relative surface areas of the individual particle size fractions were calculated (Appendix G) to determine if a correlation exists between elemental concentration and particle size. A comparison of the increases in concentration of the Ag-In-Cd with the increase in surface area was made for the different particle size fractions. No linear correlation with particle size was found, however, higher concentrations of the Ag-In-Cd materials appear to be associated with the smaller particles.

3.3.2.3. Burnable Poison Rod Materials. The two burnable poisons present in the core are $B_4C-Al_2O_3$ and $Gd_2O_3-UO_2$. Elemental constituents measured during analysis of the debris were Al, Gd, and B. Al and Gd were among the least abundant elements in the core, with original inventories of 214 and 13.5 kg, respectively. However, B was quite abundant, with approximately 172 kg from the poison rods and substantial amounts deposited from the borated reactor coolant.

The results presented in Tables 12 and 13 indicate that Gd was measurable in most of the recombined bulk samples at concentrations of 0.04 to 0.08 wt%, whereas Al was measurable only in the two surface samples (Samples 1 and 4) at concentrations of 3.37 and 1.1 wt%. The B concentrations in the recombined bulk samples indicate a concentration gradient, with the highest concentrations at the surface of the debris bed.

Observations concerning these results and their significance are as follows:

- Gd is relatively evenly distributed in the debris bed at approximately 0.056 wt%. Only four fuel assemblies in the core [at locations H4, H12, D8, and N8 (see Figure 2)] contained $Gd_2O_3-UO_2$ poison rods. The Gd concentrations at E9 are similar to H8, although the distances from E9 and H8 to the nearest Gd rod are approximately 30 and 87 cm, respectively. These data indicate Gd has been well distributed and evenly mixed with material present in the debris bed. The Gd concentration is 4 to 7 times higher than would be expected if the Gd was evenly distributed in the entire core ($\sim$0.011 wt%). The measured concentrations, if extrapolated to the estimated mass of the debris bed ($\sim$20% of the core mass) would account for almost 100% of the original Gd inventory. These data suggest, along with the Zr and Ag results, that the composition of the core below the debris bed may be significantly different.

- High concentrations of Al and B are present at the surface of the debris bed. This indicates the presence of a mechanism causing Al and B to accumulate at the surface rather than become evenly distributed within the debris bed. The B may have been deposited in the debris bed by the reactor coolant; however, the principal source of Al was the poison rods. The measured concentrations for Al at the surface are 7 to 20 times greater than if the Al were evenly distributed in the debris bed (∿1.7 mg Al/g debris). The probable mechanisms for deposition of Al at the surface is reduction of the Al_2O_3 and vaporization/deposition of the Al. The results of the particle and aliquot analysis indicate there is a relationship between particle size and Al concentration, with generally higher concentration in the smaller particle size fractions.

3.3.2.4 Structural Materials. The principal structural materials measurable in the core debris are Fe, Mn, Mo, Cr, Ni, Nb, and Sn. Table 19 lists average concentrations of these elements, ranges, and comparisons with average concentrations in the debris bed. No significant accumulations of any element were found in the debris, with the possible exception of Nb, which was expected because it has a high melting point (>2600 K). The results indicate that there has been significant depletion (50 to 75%) of structural materials from the debris bed.

3.3.2.5 Tellurium. Due to radioactive decay, no fission product Te radionuclides were measurable in the core debris grab samples. Therefore, elemental Te content was measured in an attempt to determine the concentration of fission product Te in the debris bed at the time of the accident.

Tables 12 and 13 indicate that Te concentrations were less than the ICP detection limit for the recombined bulk samples; however, Te was measurable in some particles and aliquots, but was near the ICP detection limit. Table 20 lists which particles and aliquots contain Te and summarizes the measured Te concentrations. The results indicate that most

TABLE 19. STRUCTURAL MATERIAL CONCENTRATIONS AND RANGES OF THE TMI-2 CORE DEBRIS GRAB SAMPLES

Element	Measured Average Concentration (wt%)	Range	Initial Core Average Concentration[a] (wt%)	Fraction of Core Inventory[b]
H8 Samples				
Fe	9.6 E-1	5 E-1 to 1.1	2.8	0.34
Mn	3.3 E-2	1.9 E-2 to 4.7 E-2	0.07	0.47
Cr	2.9 E-1	1.2 E-1 to 3.9 E-1	0.91	0.32
Mo	--[c]	--[c]	0.03	--[c]
Ni	3.8 E-1	1.7 E-1 to 6.5 E-1	0.84	0.45
Nb	1.7 E-1[d]	0 to 1.7 E-1	0.05	3.1
Sn	--[c]	--[c]	0.29	--[c]
E9 Samples				
Fe	4.6 E-1	2.1 E-1 to 8.3 E-1	2.8	0.16
Mn	1.7 E-2	1.4 E-2 to 2.1 E-1	0.07	0.24
Cr	1.2 E-1	6.3 E-1 to 2.1 E-1	0.91	0.13
Mo	--[c]	--[c]	0.03	--[c]
Ni	2.9 E-1[d]	2.4 to 39	0.84	0.35
Nb	1.8 E-1[d]	1.0 to 2.7	0.05	3.6
Sn	--[c]	--[c]	0.29	--[c]

---

[a] A total core mass of 1.25×10^{5} kg and an even distribution of the core inventory from Table 11 is assumed.

[b] Fraction of core inventory is calculated by dividing the measured concentration by the average core concentration.

[c] Not detected.

TABLE 20. TELLURIUM CONCENTRATIONS OF PARTICLES AND ALIQUOTS FROM THE TMI-2 CORE DEBRIS GRAB SAMPLES

Particles and Aliquots Containing Tellurium	Tellurium[a] Concentration (wt%)
H8 Samples	
Particle 1B	0.5
Particle 1E	0.3
Particle 1F	0.4
Particle 1H	0.3
74-149 μm aliquot (Sample 1)	0.8
30-74 μm aliquot (Sample 3)	0.8
>20 μm aliquot (Sample 8)	1.0
E9 Samples	
Particle 4A	0.5
Particle 4C	0.3
Particle 4E	0.5
Particle 5C	0.3
Particle 5I	9.0 E-2
Particle 6J	0.1
Particle 11A	0.8

---

a. The calculated average tellurium concentration for the original core is 3.6×10^{-3} wt%.

(75%) of the materials containing Te were located near the surface of the debris bed. The calculated original Te inventory in the core was approximately 4.45 kg, of which 800 g was estimated to be Te impurity in stainless steel and 3.65 kg was stable fission product Te. Assuming a total core mass of 1.25×10^5 kg, the average Te concentration was 3.6×10^{-3} wt%. The measured concentrations range from 25 to 277 times the average core concentration, suggesting significant relocation of Te to the surface of the debris bed. The source of the Te (i.e., either natural or fission product) is not known; however, no accumulations of other stainless steel constituents are present in the surface of the debris bed except Al.

3.4 Radiochemical Analysis

Radiochemical analyses were performed on the recombined bulk samples, particles and aliquots from all ten samples, and on the ferromagnetic component of Sample 6. Gamma spectroscopy, fissile material, and ^{90}Sr analyses were performed on the recombined bulk samples. These same analyses and ^{129}I and fertile material content analyses were performed on the particles and aliquots. Only gamma spectroscopy analysis was performed on the ferromagnetic component of Sample 6, because this portion had to be recombined with the bulk sample to allow measurement of the average radionuclide concentrations.

Radionuclides were chosen for analysis based on their importance to nuclear safety issues, because they would provide information on chemical behavior (volatility, leachability, etc.) and fission product behavior that will help define mechanisms by which radionuclides are released from the reactor core during severe fuel damage accidents. Evaluations of the radiochemical analysis results were performed to (a) determine the average radionuclide composition of the debris bed, (b) compare measured radionuclide concentrations with calculated radionuclide inventories (using the ORIGEN-2 code), (c) correlate fission product concentrations and material types (e.g., zircaloy and structural materials), (d) estimate relocation of core materials based on the enrichment of individual samples, and (e) study the Cs release and settling characteristics of the core debris materials.

3.4.1 Summary of Results

Tables 21 and 22 list the measured radionuclide concentrations for the recombined bulk samples from the H8 and H9 core locations, respectively. Results are reported in μCi/g sample. Weights of the recombined bulk samples also are listed. Radionuclide concentrations of the insoluble portion of each recombined bulk sample, as determined by gamma spectroscopy are listed in Appendix E. As discussed in Section 3.3, less than 3% of any sample was insoluble, therefore, the radionuclide concentration of the insoluble portion is relatively insignificant when compared with the dissolved portion. The total uncertainty associated with the radionuclide analysis of the recombined bulk samples is approximately 10%. Factors contributing to the total uncertainty include (a) the presence of insoluble material, (b) uncertainties associated with the analytical methods, and (c) uncertainties associated with sample weight and volume measurements.

Appendix E presents results of the radiochemical analyses of the particles and aliquots. The radionuclides measured are the same as those listed for the recombined bulk sample in Tables 21 and 22. Results of the ^{129}I and fissile/fertile material content analyses also are included in Appendix E. Uncertainties associated with analysis of the particles and aliquots are generally 10%. However, as noted in Appendix E, uncertainties for some particles and aliquots are as high as 30%, due to either mass attenuation corrections for radionuclides measured using low energy (<500 keV) gamma rays (^{155}Eu is 30%), small (<5 mg) sample weights, or sample losses during dissolution.

Table 23 lists the results of the gamma spectroscopy analysis performed to determine the radionuclide retention by the ferromagnetic constituent of Sample 6.

TABLE 21. AVERAGE RADIONUCLIDE CONCENTRATIONS OF THE RECOMBINED BULK SAMPLES FROM THE H8 CORE LOCATION (µCi/g sample)

Radionuclide	Sample 1 (23.56 g)[a]	Sample 7 (44.62 g)[a]	Sample 3 (50.10 g)[a]	Samples 8 and 9 (94.6 g)[a]
^{60}Co	4.99 ± 0.12 E+1	3.93 ± 0.11 E+1	6.44 ± 0.11	3.41 ± 0.06 E+1
^{90}Sr[b]	5.21 ± 0.23 E+3	5.49 ± 0.33 E+3	5.99 ± 0.24 E+3	5.52 ± 0.22 E+3
^{106}Ru	4.92 ± 0.13 E+2	3.61 ± 0.11 E+2	7.56 ± 0.17 E+2	3.80 ± 0.08 E+2
^{125}Sb	1.19 ± 0.03 E+2	6.52 ± 0.28 E+1	1.11 ± 0.04 E+2	7.27 ± 0.23 E+1
^{129}I[b]	5.6 E-4[c]	--[d]	3.8 E-4	--[d]
^{134}Cs	6.73 ± 0.14 E+1	6.47 ± 0.14 E+1	5.22 ± 0.12 E+1	5.53 ± 0.08 E+1
^{137}Cs	1.35 ± 0.01 E+3	1.38 ± 0.01 E+3	1.25 ± 0.01 E+3	1.30 ± 0.01 E+3
^{144}Ce	3.04 ± 0.21 E+3	3.02 ± 0.21 E+3	2.95 ± 0.20 E+3	2.78 ± 0.01 E+3
^{154}Eu	5.49 ± 0.21 E+1	5.30 ± 0.21 E+1	4.67 ± 0.19 E+1	4.65 ± 0.10 E+1
^{155}Eu	1.00 ± 0.30 E+2	9.4 ± 3.1 E+1	8.3 ± 2.6 E+1	8.4 ± 1.8 E+1
^{235}U[b]	1.64 ± 0.59 E+1	1.78 ± 0.09 E+1	1.94 ± 0.10 E+1	1.84 ± 0.02 E+1

---

a. Sample weight dissolved.

b. These analyses were performed by the methods discussed in Section 2.

c. Results calculated from analysis of the particles and aliquots.

d. Analyses were performed for ^{129}I, however, safety restrictions made it necessary to reduce the sample size, thereby reducing the number of measurable results below the quantity required to calculate bulk sample concentrations.

TABLE 22. AVERAGE RADIONUCLIDE CONCENTRATIONS OF THE RECOMBINED BULK SAMPLES FROM THE E9 CORE LOCATION (μCi/g sample)

Radionuclide	Sample 4 (5.11 g)[a]	Sample 5 (16.64 g)[a]	Sample 6 (45.97 g)[a]	Sample 10 (57.44 g)[a]	Sample 11 (42.54 g)[a]
^{60}Co	5.68 ± 0.11 E+1	4.68 ± 0.14 E+1	3.72 ± 0.12 E+1	3.25 ± 0.11 E+1	5.18 ± 0.14 E+1
^{90}Sr[b]	6.33 ± 0.21 E+3	6.73 ± 0.34 E+3	5.07 ± 0.27 E+3	5.99 ± 0.28 E+3	4.97 ± 0.25 E+3
^{106}Ru	7.12 ± 0.11 E+2	1.01 ± 0.02 E+3	5.46 ± 0.19 E+2	6.54 ± 0.17 E+2	5.65 ± 0.16 E+2
^{125}Sb	8.13 ± 0.19 E+1	1.45 ± 0.03 E+2	1.01 ± 0.04 E+2	9.72 ± 0.36 E+1	1.94 ± 0.04 E+2
^{129}I[b]	2.4 E-4[c]	5.9 E-4[c]	4.2 E-4[c]	--[d]	--[d]
^{134}Cs	2.43 ± 0.06 E+1	1.09 ± 0.02 E+2	8.56 ± 0.02 E+1	6.69 ± 0.14 E+1	7.57 ± 0.18 E+1
^{137}Cs	4.77 ± 0.02 E+2	2.44 ± 0.07 E+3	2.11 ± 0.01 E+3	1.56 ± 0.06 E+3	1.91 ± 0.01 E+3
^{144}Ce	3.64 ± 0.18 E+3	3.05 ± 0.02 E+3	2.15 ± 0.22 E+3	2.58 ± 0.22 E+3	2.59 ± 0.22 E+3
^{154}Eu	5.47 ± 0.17 E+1	4.88 ± 0.26 E+1	2.90 ± 0.19 E+1	4.14 ± 0.21 E+1	3.23 ± 0.18 E+1
^{155}Eu	1.14 ± 0.36 E+2	9.8 ± 3.2 E+1	7.8 ± 2.6 E+1	8.8 ± 2.9 E+1	8.0 ± 2.6 E+1
^{235}U[b]	2.11 ± 0.21 E+1	2.29 ± 0.10 E+1	1.94 ± 0.07 E+1	1.96 ± 0.09 E+1	2.11 ± 0.11 E+1

---

a. Sample weight dissolved.

b. These analyses were performed by the methods discussed in Section 2.

c. Results calculated from analysis of the particles and aliquots.

d. Analyses were performed for ^{129}I, however, safety restrictions made it necessary to reduce the sample size, thereby reducing the number of measurable results below the quantity required to calculate bulk sample concentrations.

TABLE 23. RADIONUCLIDE CONCENTRATIONS OF THE FERROMAGNETIC COMPONENT OF SAMPLE 6 (μCi/g)

	Particle Size Fraction (μm)			
Radionuclide	707-1000 (0.25 g)[a]	297-707 (0.19 g)[a]	149-297 (0.025 g)[a]	74-149 (0.024 g)[a]
^{54}Mn	7.4 ± 3.0 E-1	4.0 ± 1.2	3.4 ± 1.2	5.2 ± 1.2
^{60}Co	2.01 ± 0.02 E+2	7.31 ± 0.07 E+2	6.18 ± 0.07 E+2	5.48 ± 0.06 E+2
^{106}Ru	3.22 ± 0.54 E+2	1.39 ± 0.17 E+3	7.47 ± 0.20 E+2	6.46 ± 0.17 E+2
^{125}Sb	2.35 ± 0.03 E+2	3.34 ± 099 E+2	3.23 ± 0.10 E+2	3.46 ± 0.09 E+2
^{134}Cs	1.86 ± 0.35	8.79 ± 0.25 E+1	5.26 ± 0.22 E+1	6.72 ± 0.27 E+1
^{137}Cs	3.61 ± 0.06 E+1	1.58 ± 0.01 E+3	1.02 ± 0.01 E+3	1.24 ± 0.01 E+3
^{144}Ce	1.24 ± 0.22 E+2	7.4 ± 1.1 E+2	4.7 ± 1.0 E+2	4.31 ± 0.86 E+2
^{154}Eu	1.55 ± 0.53	1.35 ± 0.24 E+1	6.7 ± 2.0	7.4 ± 1.8
^{155}Eu	8.7 ± 2.9	3.3 ± 1.1 E+1	2.0 ± 0.6 E+1	2.3 ± 0.7 E+1

---

[a] Weight of the ferromagnetic component.

3.4.2 Radionuclide Composition of the Core Debris

The radionuclide composition of the core debris was determined based on the radionuclide concentrations of the recombined bulk samples (listed in Tables 21 and 22. Results are discussed in the order of expected fission product volatility.

Fission products are categorized in Table 24 by volatility of the chemical group and element. This grouping is consistent with the WASH-1400 characterization.[24,25] Some possible chemical compounds for each element are also summarized, and the boiling temperatures of elements and some compounds are listed. Radionuclides for which analysis of the core debris grab samples were performed also are indicated.

The high-volatility fission product groups (I, II, III, and IV.A) shown in Table 24 contain the noble gases, halogens, alkali metals, and heavy chalcogens, and are characterized by boiling points less than 1600 K for the elemental forms as well as for the listed oxide compounds.

The medium-volatility fission products are characterized by boiling points less than 3100 K (UO_2 melting). These materials include fission product elements from the Group VA metals, alkaline earths, some of the rare earths, and actinides. The volatility of elements in this classification is strongly dependent on chemical form. For example, BaO has a low volatility, BaH_2 has a medium volatility, and BaO_2 has a high volatility. The chemical form of Ba will depend primarily on fuel chemistry, the oxidizing potential in the reactor coolant system, and temperature.

The low-volatility materials include fission product elements from the noble metals, the remaining rare earths and actinides, tetravalents, and early transition elements. Generally the oxides of these elements also have low volatilities; however, LaO and some of the noble metal oxides are significantly more volatile than the element.

TABLE 24. CORE MATERIAL VOLATILITY GROUPS

WASH-1400 Group Number	Chemical Group	Element	Boiling[a] Temperature (K)	Volatility	Possible Compounds	Boiling[a] Temperature (K)	Volatility	Analysis Performed
Fission Products								
I	Noble gases	Kr[b]	121	High		--	--	--
		Xe[b]	166	High		--	--	
II	Halogens	Br	332	High	CsBr[b]	1573	High	X
		I	458	High	CsI[b]	1553	High	
					HI	238	High	
III	Alkali metals	Rb[b]	973	High	RbI[b]	1577	High	X
					Rb_2O	--	High	
					Rb_2O_2	1273	High	
		Cs[b]	963	High	CsI[b]	1553	High	
					CsOH	~1350[c]	High	
					Cs_2O	--	High	
					Cs_2O_2	923	High	
					Cs_2UO_4 [b]	--	--	
IV.a	Heavy chalcogens	Se[b]	958	High	SeO_3	453	High	X
					SeO_2	613	High	
		Te[b]	1215	High	TeO_2	~1450	High	
					Te_2O_2	--	--	
					silver-telluride	--	--	
					iron-telluride	--	--	
					zirconium telluride	--	--	
					tin-telluride	--	--	
					nickel-telluride	--	--	
					chrome-telluride	--	--	
Fission Products								
IV.b	Group VA metals	Sb[b]	2023	Medium	Sb_2O_3	1823	Medium	X
V	Alkaline earths	Sr	1657	Medium	SrO[b]	~3100[c]	Low	X
		Ba	1913	Medium	BaH_2	1673	Medium	
					BaO[b]	~3500[c]	Low	
					BaO_2	1073	High	
VII	Rare earths	Eu	1870	Medium	Eu_2O_3 [b]	--	--	
		Sm	2051	Medium	Sm_2O_3 [b]	--	--	
		Pm	2733	Medium	Rm_2O_3 [b]	--	--	
	Actinides	Am	2880	Medium	AmO_2 [b]	--	--	

TABLE 24. (continued)

WASH-1400 Group Number	Chemical Group	Element	Boiling Temperature (K)[a]	Volatility	Possible Compounds	Boiling Temperature (K)[a]	Volatility	Analysis Performed
VI	Noble metals	Pd[b]	3413	Low	PdO	--	--	X
		Rh[b]	4000	Low	RhO_2	--	--	
					Rh_2O_3	--	--	
		Ru[b]	4173	Low	RuO_2	--	--	
					RuO_4	--	--	
		Mo[b]	4885	Low	MoO_2 [b]	--	--	
					Mo_2O_3	~1300[c]	High	
					MoO_3	--	--	
		Tc[b]	5150	Low		--	--	
VII	Rare earths	Y	3611	Low	Y_2O_3 [b]	--	--	
		La	3730	Low	LaO	--	Medium-High	X
					La_2O_3 [b]	4473	Low	
		Ce	3530	Low	CeO_2	--	--	
					Ce_2O_3 [b]	--	--	
		Pr	3485	Low	PrO_2	--	--	
					Pr_2O_3 [b]	--	--	
		Nd	3400	Low	Nd_2O_3	--	--	
	Actinides	Np	4175	Low	NpO_2 [b]	--	--	
		Pu	3505	Low	PuO_2 [b]	~3570	Low	
		Cm	--	Low	CmO_2 [b]	--	--	
	Tetravalents	Zr[d]	4650	Low	ZrO_2 [b]	5273	Low	
	Early transition	Nb	5015	Low	NbO_2 [b]	--	Low	
					Nb_2O_5	--	--	

---

a. Boiling temperature at 1 atm., data primarily from CRC Handbook of Chemistry and Physics, 56th Edition.

b. Probable chemical form of the fission product within the fuel.

c. NAA-SR-132.

d. Zirconium is both a fission product and a structural material.

e. Probable form of oxide released because of MoO_2 decomposition.

3.4.2.1 Cesium and Iodine. ^{129}I and ^{134,137}Cs are the most volatile radionuclides measurable in the core debris grab samples and have been released to the reactor coolant system in significant quantities. The ^{129}I concentrations listed in Tables 21 and 22 were obtained by weighting the results of the particle and aliquot analyses. ^{129}I analysis was performed on recombined bulk samples (Samples 1, 3, 4, 5, and 6). Subsequent safety restrictions made it necessary to reduce the sample sizes for Samples 7 through 11, thereby reducing the number of measurable results below the number required to calculate average bulk sample concentrations. The ^{129}I results for the five measured samples are mutually consistent, suggesting relatively homogeneous ^{129}I concentrations in the debris bed. The estimated uncertainty for the calculated concentrations is at least 100%. Retention of ^{129}I in the fuel matrix and on structural materials is further evaluated in Section 3.4.3 and 3.4.4.

At the H8 sample locations, the concentrations of ^{137}Cs at all depths are relatively consistent (within 5% of the average concentration of 1.32 E+3 μCi/g sample). At the E9 sample locations, however, the ^{137}Cs concentrations vary more widely. The ^{137}Cs concentration for Sample 4 (E9, surface) is a factor of 5 lower than any other ^{137}Cs concentration within the debris bed. These data indicate a significant change in concentration at the surface of the debris bed. The concentration is highest for Sample 5 (E9, 8 cm) and generally decreases with increasing depth, suggesting the presence of a concentration gradient.

Comparing the measured ^{137}Cs concentrations at the H8 and E9 locations suggests significant differences in fission product behavior at the two locations:

- The ^{137}Cs concentrations are higher (from 18 to 85%) at E9 than at H8, suggesting radial differences in the radionuclide composition of the core. The data suggest that the H8 and E9 locations experienced different conditions during or after the accident.

- Although the ^{137}Cs concentrations at H8 are consistent, a gradient is indicated at the E9 location. A 22 to 36% decrease in ^{137}Cs concentration from Sample 5 (8 cm) to Samples 10 and 11 (74 to 94 cm in the debris bed) suggests that areas deeper in the core may have different radionuclide concentrations.

3.4.2.2 Strontium and Antimony. ^{90}Sr and ^{125}Sb have relatively moderate volatilities as elements. However, as compounds, Sb_2O_3 has a moderate volatility, but SrO has a low volatility. The concentrations of ^{90}Sr for all H8 samples are within 6% of the average concentration (5.55 E+3 μCi/g sample). These data indicate that the distribution of ^{90}Sr in the debris bed at the H8 location is relatively consistent. Also, comparison of the fissile material content with ^{90}Sr concentrations suggests that ^{90}Sr retention in the fuel is rather uniform. Other examinations (not part of this report) have determined that small amounts of ^{90}Sr have leaked into the reactor coolant.[26] Retention of ^{90}Sr in the fuel is discussed in Sections 3.4.3 and 3.4.4.

At the E9 location, the ^{90}Sr concentrations are more variable (within 15% of the average concentration of 5.82 E+3 μCi/g sample). However, the data indicate that ^{90}Sr is relatively evenly deposited in the debris bed.

At the H8 and E9 locations, the ^{125}Sb concentrations vary by about a factor of 2. The average concentration at E9 is approximately 23% higher than at H8, suggesting a radial gradient or variation in burnup between the two locations. No correlation with fissile material content is apparent for ^{125}Sb.

3.4.2.3 Ruthenium. Ru fission products are expected to be relatively nonvolatile as the metal but more volatile in the oxide forms (especially RuO_4). The ^{106}Ru concentrations listed in Tables 21 and 22 vary significantly (up to a factor of 2.8) at the H8 and E9 locations. The concentrations at E9 are generally higher than at H8. At H8, the concentrations range from 3.61 E+2 to 7.56 E+2 μCi/g, whereas at E9 the concentrations range from 5.46 E+2 to 1.01 E+3 μCi/g, indicating a radial concentration gradient. No correlation between concentration and depth is apparent. Comparison with fissile material (^{235}U) content indicates significant relocation of ^{106}Ru from the fuel. The ^{106}Ru/^{235}U ratios range from 20.6 to 39 at H8 and from 27 to 44 at E9, suggesting variations in ^{106}Ru retention in the fuel. Variations in burnup can affect this correlation, however, further evidence of ^{106}Ru relocation and evidence of a correlation between ^{106}Ru and structural material content is discussed in Section 3.4.4.

3.4.2.4 Cerium and Europium. ^{144}Ce and ^{154,155}Eu are refractory materials in the lanthanide group and were expected to have been retained significantly in the fuel. ^{144}Ce is discussed principally because comparison of the ^{144}Ce/^{154,155}Eu ratios indicates that the cerium and Eu behave similarly, with the exceptions of Samples 6 and 11 which have higher than expected ratios.

The ^{144}Ce concentrations at H8 are similar (within 9%) at all depths. Correlations with fissile material content indicates higher ratios (12 to 22%) near the surface of the debris bed.

There is an apparent gradient (∿29%) in the ^{144}Ce concentrations at the E9 locations, from high values at the surface to lower values at 94 cm into the debris bed. Correlation with fissile material content indicates higher ^{144}Ce/^{235}U ratios (∿28%) near the surface of the debris bed. An explanation for the variation in ratios is discussed in Section 4.3.

3.4.2.5 Cobalt. ^{60}Co is an activation product of Co present in stainless steel and Inconel. The data suggest variations in concentrations by factors of 1.8 and 7.7 at H8 and E9, respectively. ^{60}Co concentrations can provide some indication of the structural material content of the core debris grab samples.

3.4.3 Comparison with ORIGEN-2 Predicted Radionuclide Concentrations

The measured radionuclide concentrations of the recombined bulk samples were compared with concentrations predicted by the ORIGEN-2 computer code in order to assess retention of radionuclides in the core and fuel matrix. Appendix F presents the average radionuclide concentrations per gram of U, as predicted by a nodular ORIGEN-2 analysis.[27] Average predicted radionuclide concentrations are used because the quantities of fission products associated with each gram of U varies with ^{235}U enrichment and burnup (total neutron exposure). Figures F-1 through F-7 in Appendix F show the variations in burnup and enrichment before the accident as functions of radial position and depth in the core. Burnup of the reactor fuel and, consequently, fission product concentrations predicted by ORIGEN-2 vary from the average concentration by a factor of approximately 2 for the TMI-2 core. Therefore, comparing measured to predicted concentrations only provides indications of average fission product retention in the core. However, a measure of the accuracy of the comparison is obtained by comparing retention of the refractory materials (e.g., ^{144}Ce) with predicted concentrations to obtain an effective measure of burnup.

Two methods were used to estimate radionuclide retention in the core materials:

- The measured radionuclide concentrations in the core debris grab samples were extrapolated to the weight of all materials present in the core (1.25×10^5 kg) and ratioed to the total fission product inventories listed in Appendix F. This analysis assumes the debris bed is representative of the core as a whole.

- The radionuclide concentrations were normalized to the amount of U present in each bulk sample (see Tables 12 and 13) and ratioed to the average fission product concentration per gram of U. This analysis assumes that the U contains the radionuclide inventory and that the sample has an average burnup.

Table 25 summarizes the retention of radionuclides in the core, based on extrapolating the recombined bulk sample concentrations to the total core weight. With few exceptions, retention follows the order of volatility of the fission products discussed in Section 3.4.2. The ^{129}I, ^{134}Cs, and ^{137}Cs radionuclide concentrations indicate the lowest retention, ranging from 20 to 30% of the core inventory at both the H8 and E9 locations. This suggests significant (70 to 80%) release of these fission products from the debris bed. Measurements of ^{137}Cs released to other portions of the reactor account for approximately 40% of the core inventory of ^{137}Cs,[28] suggesting that the calculated retention of these radionuclides based on analysis of the core debris grab samples is relatively accurate.

Significant variations in retention of ^{106}Ru are indicated at the H8 and E9 locations. Although the ranges overlap for the two locations, average retention varies by approximately 25%, suggesting significantly more depletion at the H8 sample locations. Mechanisms accounting for this behavior are discussed in Section 4.

The measured retentions of ^{90}Sr and ^{125}Sb in the debris bed differ significantly, although both elements have similar volatilities (the expected compounds do not). The results indicate ^{90}Sr is significantly retained in the debris bed at both locations, as predicted. The listed retentions are greater than 100%; however, they are within the uncertainty of this analysis ($\sim$15%). For ^{125}Sb, however, the average measured retention is significantly less (21 to 31%) at both locations, indicating behavior similar to ^{137}Cs. No explanation is apparent for the low concentrations of ^{125}Sb; however, Sb appears to be scavenged in some cases by structural material (see Section 3.4.4.2) and may have been transported to other locations in the reactor core (see Section 4).

The refractory radionuclides (^{144}Ce, ^{154}Eu, and ^{155}Eu) were significantly retained in the core debris at both the H8 and E9 locations. The ^{144}Ce concentrations are significantly greater than 100% (i.e., $\sim$130%). Possible explanations may be that (a) the core debris grab

TABLE 25. RADIONUCLIDE RETENTION IN THE TMI-2 CORE[a]

		H8 Samples			E9 Samples		
Radionuclide	Total Core Inventory[b] (Ci)	Average Concentration[c]	Fraction of Inventory Retained[d] (%)	Range[e] (%)	Average Concentration[c]	Fraction of Core Inventory Retained[d] (%)	Range[e] (%)
^{90}Sr	6.62 E+5	5.55 E+3	105	98-113	5.82 E+3	110	94-127
^{106}Ru	1.15 E+5	4.97 E+2	54	39-82	6.97 E+2	76	59-110
^{125}Sb	3.70 E+4	9.20 E+1	31	22-40	6.23 E+1	21	4.9-34
^{129}I	2.29 E-1	4.70 E-4	26	21-31	4.17 E-4	23	13-32
^{134}Cs	3.70 E+4	5.99 E+1	20	18-23	7.23 E+1	24	8.2-37
^{137}Cs	7.60 E+5	1.32 E+3	22	21-23	1.70 E+3	28	7.8-40
^{144}Ce	2.75 E+5	2.95 E+3	134	126-138	2.80 E+3	127	98-165
^{154}Eu[f]	6.38 E+3	6.03 E+1	98	91-108	4.12 E+1	81	57-107
^{155}Eu[f]	1.61 E+4	9.02 E+1	70	64-78	9.16 E+1	71	60-88

---

a. Radionuclide retention is calculated assuming the core is homogeneous and the chemical composition is similar throughout the core.

b. The total core fission product inventories (in Ci), as calculated by ORIGEN-2, are listed in Appendix F.

c. Average concentration is listed in µCi/g debris.

d. Fraction of core inventory retained is calculated by extrapolating the average radionuclide concentration to the total core mass.

e. The range is for the miminum and maximum calculated fractions of core inventory retained for all H8 or E9 samples.

f. The predicted concentrations for ^{154}Eu and ^{155}Eu have relatively large associated uncertainties (20-30%) because of uncertainties in the production of these radionuclides as extrapolated to the entire core.

samples were obtained from locations with higher than average burnup or (b) ^{144}Ce behavior may have been perturbed by the dissolution of the UO_2 matrix, concentrating this radionuclide in the samples measured. These results are further discussed in Section 4. As illustrated in Table 25 uncertainties in the core inventory calculations may cause significant variations for ^{154}Eu and ^{155}Eu.[29]

To evaluate retention in the fuel and, as previously discussed, provide another estimate of radionuclide retention in the core debris, the measured radionuclide concentrations were normalized to the measured U content for each sample (see Section 3.3) and compared to the average fission product concentrations calculated by ORIGEN-2. Table 26 summarizes the retention of radionuclides in the core debris, based on fission product concentrations normalized to U content. Also included is the effective enrichment determined for each sample, based on the fissile material content from Tables 21 and 22 and U content from Tables 12 and 13. The enrichment results indicate significant variations from the original U enrichments at H8 (2.64%) and E9 (1.98%). At H8, some of the measured enrichments (i.e., Samples 7, 8, and 9) are similar to the original enrichments. However, at E9 the enrichments are significantly higher than the original 1.96% enrichment, indicating significant fuel mixing. Original burnup at E9 ranged from 1931 to 4485 MWd/MTU, whereas at H8 the burnup ranged from 2057 to 6213 MWd/MTU. Although H8 had a higher original burnup, the data indicate significant relocation. The fractions of the core inventory retained are similar to those listed in Table 25; however, normalization to U content indicates the presence of a ^{144}Ce concentration gradient at both H8 and E9, with the highest concentrations near the surface. These results are discussed further in Section 4.3.

Table 27 compares the fractions of core inventory retained, calculated by extrapolating the measured fission product concentrations to the weight of all core components and normalizing to the quantity of fission products present in a gram of U. Retention calculated by either method is similar; however, the calculated retention based on the quantity of fission products

TABLE 26. RADIONUCLIDE RETENTION NORMALIZED TO URANIUM CONTENT[a] (% of core inventory)

		H8 Samples[c]				E9 Samples[c]				
Radionuclide	Calculated Core Average Concentration[b] (Ci/g U)	1	2	3	8 and 9	4	5	6	10	11
^{90}Sr	8.12 E-3	91	91	102	94	94	100	88	101	79
^{106}Ru	1.41 E-3	50	35	74	37	61	86	55	63	52
^{125}Sb	4.53 E-4	37	19	34	22	22	3.8	32	29	1.8
^{129}I	2.81 E-9	28	--[d]	19	--[d]	10	25	21	--[d]	--[d]
^{134}Cs	4.53 E-4	21	19	16	17	6.4	29	27	20	22
^{137}Cs	9.32 E-3	21	20	18	19	6.2	32	32	23	26
^{144}Ce	3.37 E-3	128	121	121	114	130	110	90	104	99
^{154}Eu	7.82 E-5	100	92	82	82	84	75	52	72	53
^{155}Eu	1.98 E-4	72	64	58	59	69	60	56	61	52
^{235}U[e]/^{238}U (%)	--	2.3	2.4	2.7	2.5	2.5	2.8	2.7	2.7	2.7

---

a. Chemical analyses indicate there are no significant concentrations of structural components and, consequently, the calculated retention is representative of the debris bed without signficant structural contamination.

b. Calculated concentrations are from Appendix F.

c. Uranium content used for normalization from elemental content in Section 3.

d. Not reported.

e. ^{235}U values are from Table E-11, and total uranium from Tables 12 and 13.

TABLE 27. COMPARISON OF RADIONUCLIDE RETENTION CALCULATED BY DIFFERENT METHODS
(% of core inventory)

	H8 Samples		E9 Samples	
Radionuclide	Extrapolation to Core Weight[a]	Extrapolation to a Gram of Uranium[b]	Extrapolation to Core Weight[a]	Extrapolation to a Gram of Uranium[b]
^{90}Sr	105	95	110	92
^{106}Ru	54	49	76	63
^{125}Sb	31	28	21	18
^{129}I	26	23	23	19
^{134}Cs	20	18	24	21
^{137}Cs	22	20	28	24
^{144}Ce	134	121	127	107
^{154}Eu	98	89	81	67
^{155}Eu	70	63	71	60

---

a. Results taken from Table 25.

b. Average concentrations obtained from Table 26.

in a gram of U is lower (10 to 15%). This method probably is more accurate, because the quantity of structural material in the debris bed to which extrapolations using core weight are made is not well known.

3.4.4 Fission Product Association With Zr and Structural Materials

Fission product association with Zr and structural materials indicates release of fission products from the fuel and subsequent association (by vaporization/deposition, chemical reaction, etc.) with other materials in the core region. Data used in this evaluation are from the gamma spectroscopy analysis of the ferromagnetic components of Sample 6 and from analysis of particles and aliquots that are predominantly U, Zr, or structural material.

3.4.4.1 Ferromagnetic Material Analysis. Table 28 lists the gamma spectroscopy analysis results from the measurable ferromagnetic components of Sample 6. These data provide an indication of the fission product concentrations associated with structural materials. Table 28 compares radionuclide concentrations of the ferromagnetic components with those of the recombined bulk samples. The data can be divided into two distinct groups of radionuclides. The first group, including ^{60}Co, ^{106}Ru, and ^{125}Sb, generally show concentrations higher than those of the average recombined bulk samples, whereas the concentrations of the second group, ^{134}Cs, ^{137}Cs, ^{154}Eu, and ^{155}Eu, are lower than the average concentrations. The ^{54}Mn (not measurable in the recombined bulk samples) and ^{60}Co are neutron activation products of stainless steel and are expected to be measurable in the ferromagnetic material fraction. The ^{106}Ru and ^{125}Sb, however, are fission products, and the data suggest that these radionuclides tend to be released from the fuel and become associated with structural materials. These data are further evaluated in the discussion in Section 3.4.4.2.

The average or lower than average concentrations of ^{134}Cs, ^{137}Cs, ^{144}Ce, ^{154}Eu, and ^{155}Eu were expected. The ^{134}Cs and ^{137}Cs are lower than expected because they may have been significantly leached into

TABLE 28. COMPARISON OF THE FERROMAGNETIC/AVERAGE RADIONUCLIDE CONCENTRATIONS OF SAMPLE 6[a]

Radionuclide	Particle Size Fraction (μm) 707-1000 Aliquot	297-707 Aliquot	149-297 Aliquot	74-149 Aliquot
^{54}Mn	--[a]	--[a]	--[a]	--[a]
^{60}Co	5.4	19.6	16.6	14.7
^{106}Ru	0.59	2.6	1.4	1.2
^{125}Sb	2.3	3.3	3.2	3.4
^{134}Cs	0.02	1.0	0.6	0.79
^{137}Cs	0.02	0.75	0.48	0.59
^{144}Ce	0.06	0.34	0.22	0.20
^{154}Eu	0.06	0.47	0.23	0.26
^{155}Eu	0.30	1.1	0.69	0.79

---

a. This table lists the ratios of the radionuclide concentrations measured in the ferromagnetic component of Sample 6 to the recombined bulk sample average concentration. High ratios indicate accumulations of the radionuclide in the ferromagnetic component.

the coolant since the accident (see Reference 28) or were not strongly attracted to the structural materials. The low concentrations of ^{144}Ce, ^{154}Eu, and ^{155}Eu were expected because these materials tend to remain in the fuel.

3.4.4.2 Particle and Aliquot Analysis. The analysis results of the particles and aliquots provide further indications of the retention of fission products by U, Zr, and structural materials. Chemical and radiochemical analyses were performed on each particle and aliquot studied. Table 29 lists the fission product concentrations for those particles that were principally U or Zr.

As shown in Table 29, ^{129}I and ^{134,137}Cs appear to be retained in different amounts between the U and Zr particles. ^{137}Cs is associated more with U than with Zr, whereas ^{129}I is associated to a greater extent with the Zr particles.

Table 30 summarizes the correlations of the particle and aliquot results shown in Figures 32 through 41. No correlations were observed between ^{137}Cs or ^{129}I and uranium for the particles and aliquots (Figures 32 and 33). There is no apparent correlation between the ^{137}Cs and ^{129}I concentrations [i.e., no similarity in the ratios of these radionuclides (Figure 34 and Table 29)]; however, the data in Table 29 are for a limited number of particles with concentrations ranging by a factor of 100, which may bias the average concentrations.

Table 29 indicates that ^{106}Ru is retained in the fuel, with only small amounts (~3%) associated with Zr. No general correlation with structural materials (e.g., Ni) was observed, except for particles 9D and 9G which are metallic appearing and contain significant quantities of Ni. A comparison of the ^{106}Ru and ^{125}Sb radionuclide concentrations with the Ni concentration are listed in Table 31. The radionuclide concentrations are 10 to 100 times greater than would be expected for a UO_2 fuel pellet, even at high burnup (6200 MWd/MTU). This behavior

TABLE 29. COMPARISON OF FISSION PRODUCT CONCENTRATIONS ASSOCIATED WITH PARTICLES WHICH WERE PRINCIPALLY URANIUM OR ZIRCONIUM

Radionuclide	Principally Uranium Bearing Particles[a]		Principally Zirconium Bearing Particles[b]		Zr Rich (µCi/g) / U Rich (µCi/g)
	Average (µCi/g)	Range (µCi/g)	Average (µCi/g)	Range (µCi/g)	
^{60}Co	1.2 E+1	0 - 70.4	1.45 E+1	1.2 - 5.9 E+1	1.2
^{90}Sr	4.95 E+3	1.4 E+1 - 1.23 E+4	1.21 E+2	2.6 E+1 - 1.65 E+2	2.4 E-4
^{106}Ru	1.01 E+3	5.40 E+2 - 1.73 E+3	3.3 E+1	1.3 - 1.16 E+2	3.3 E-2
^{125}Sb	8.55 E+1	3.86 E+1 - 1.49 E+2	1.01 E+2	6.9 - 3.05 E+2	1.18
^{129}I	6.38 E-4	3.5 E-5 - 1.6 E-3	1.20 E-3	2.2 E-5 - 4.8 E-3	1.88
^{134}Cs	6.12 E+1	2.9 - 1.69 E+2	1.9 E+1	0.5 - 6.29 E+1	0.31
^{137}Cs	1.82 E+3	5.3 E+1 - 4.38 E+3	5.40 E+2	1.17 E+1 - 1.24 E+3	0.30
^{144}Ce	2.93 E+3	1.81 E+3 - 4.67 E+3	5.20 E+2[c]	1.9 - 2.84 E+3	0.18
^{154}Eu	3.79 E+1	1.58 E+1 - 7.87 E+1	7.7 E-1[c]	0 - 0.98	2.0 E-2
^{155}Eu	1.11 E+2	0 - 2.07 E+2	5.9[c]	0 - 2.21 E+1	5.3 E-2

a. Particles were principally zirconium with a few other contaminants. Particles 1B, 3F, 5D, 6A, 6G, 6H, and 7H were analyzed.

b. Particles were principally uranium with little contaminants from other components. Particles 1I, 3B, 6B, 6C, 6E, and 6F were analyzed.

c. Results were biased by Particle 6B.

ABLE 30. SUMMARY OF CORRELATIONS BETWEEN SELECTED RADIONUCLIDES, ELEMENTS, AND PARTICLE SURFACE AREA

igure	Correlated Materials or Result	Comment
32	^{137}Cs/U content	No apparent correlation was observed between ^{137}Cs and uranium content for particles or aliquots.
33	^{129}I/U content	No apparent correlation was found between ^{137}Cs and uranium content for particles or aliquots.
34	^{129}I/normalized particles surface area	There is a correlation between higher concentrations and smaller particle size, perhaps due to increased surface area. These results suggest vaporization/condensation on surfaces or possible reaction with nonfuel materials which have higher concentrations in the smaller particle size groups.
35	^{137}Cs/^{129}I	No apparent correlation between ^{137}Cs and ^{129}I was observed.
36	^{106}Ru/Ni content	No correlation was observed for most particles and aliquots.
37	^{125}Sb/Ni content	No apparent correlation was observed.
38	^{106}Ru/U content	No obvious correlation is apparent.
39	^{125}Sb/U content	No correlation is apparent.
40	^{125}Sb/^{129}I	No correlation is apparent.
41	^{144}Ce/U content	No correlation is apparent.

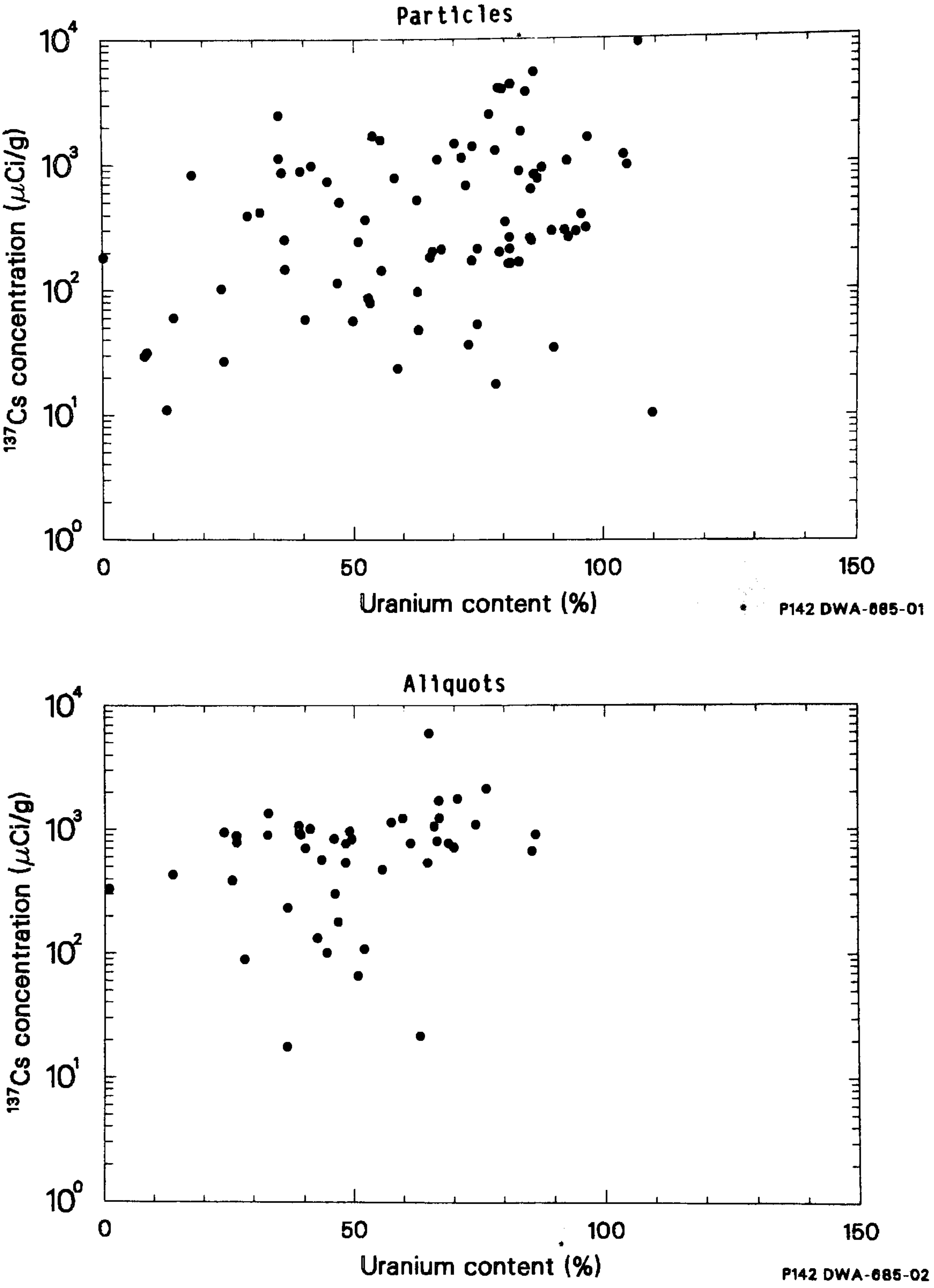

Figure 32. ^{137}Cs/U content correlation for all particles and aliquots analyzed.

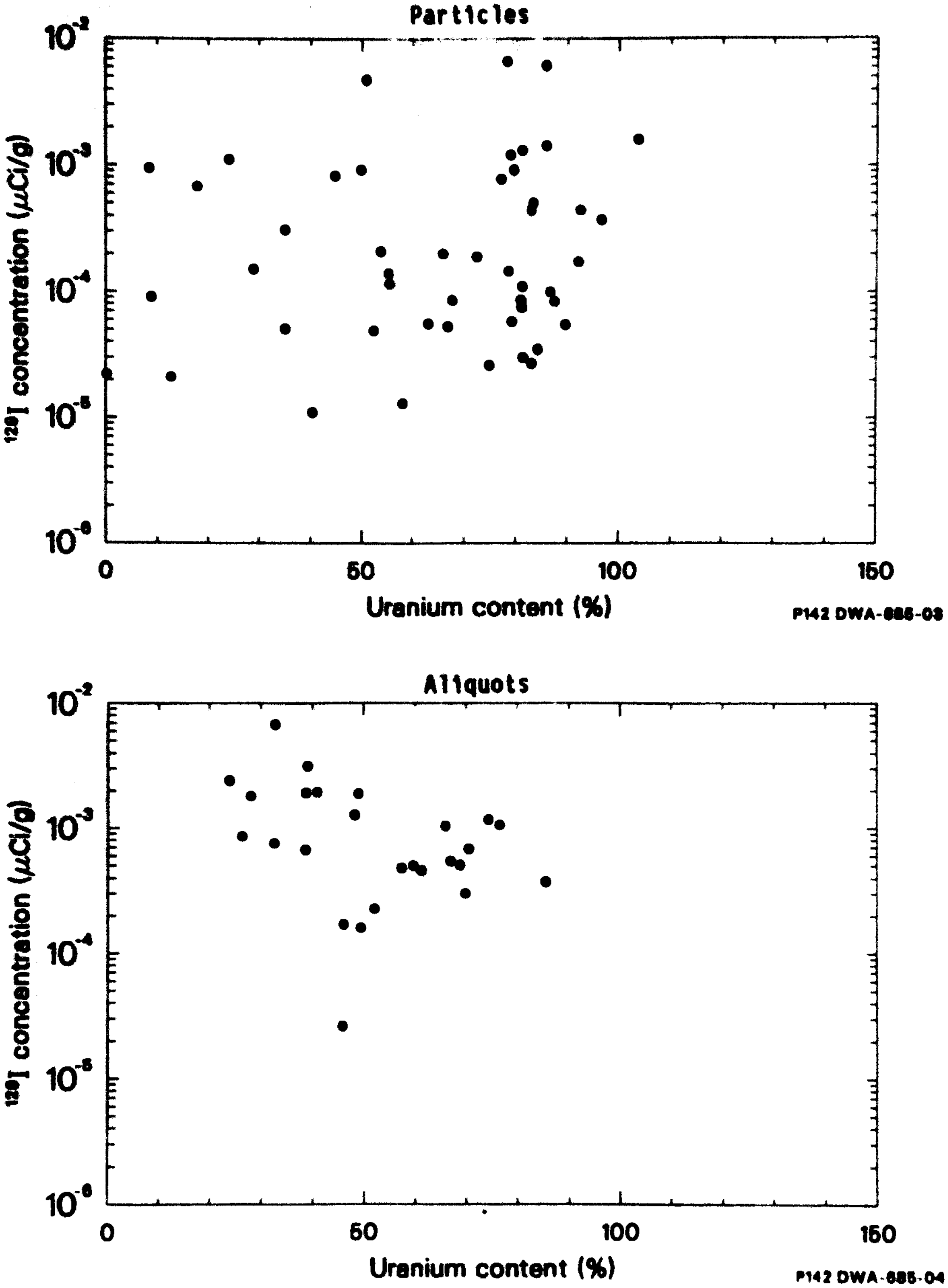

Figure 33. ^{129}I/U content correlation for all particles and aliquots analyzed.

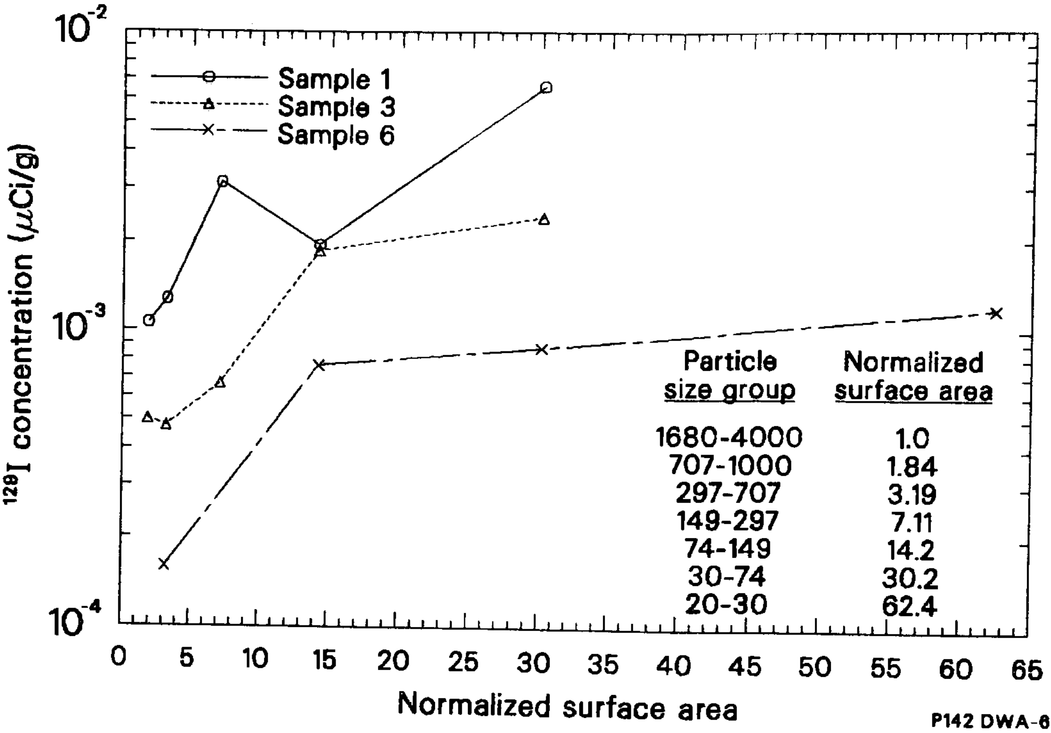

P142 DWA-685-26

Figure 34. Relationship between ^{129}I concentration and surface area for Samples 1, 3, and 6.

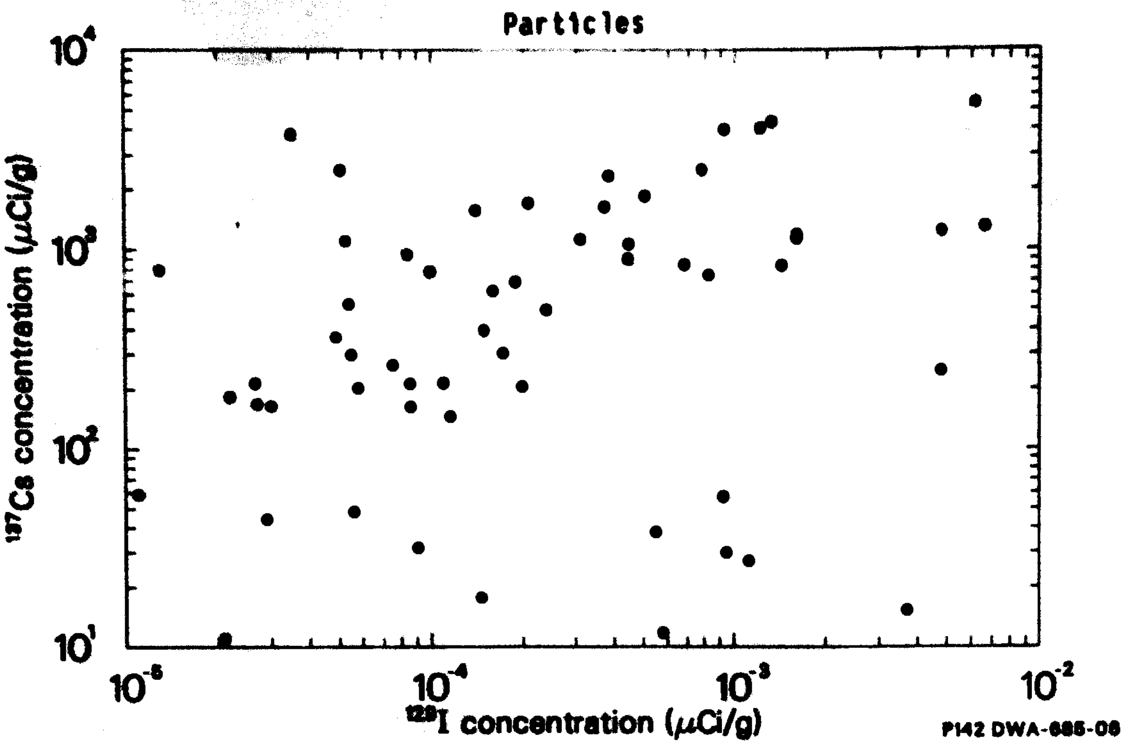

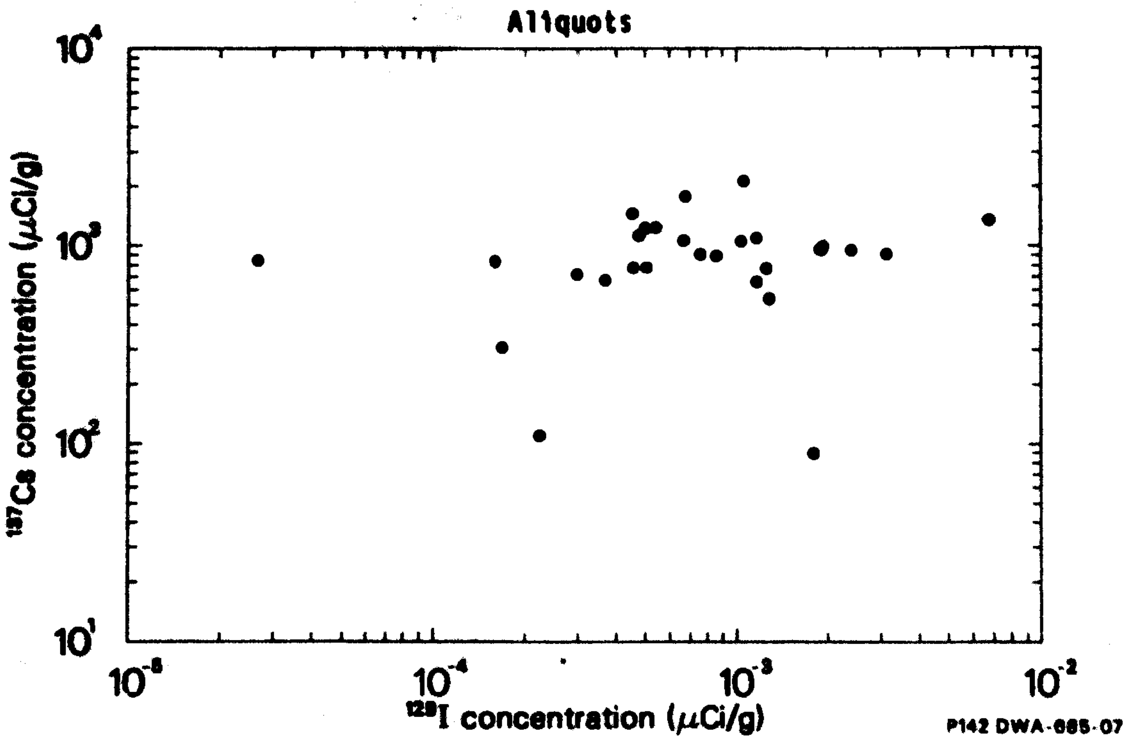

Figure 35. ^{137}Cs/^{129}I content correlation for all particles and aliquots analyzed.

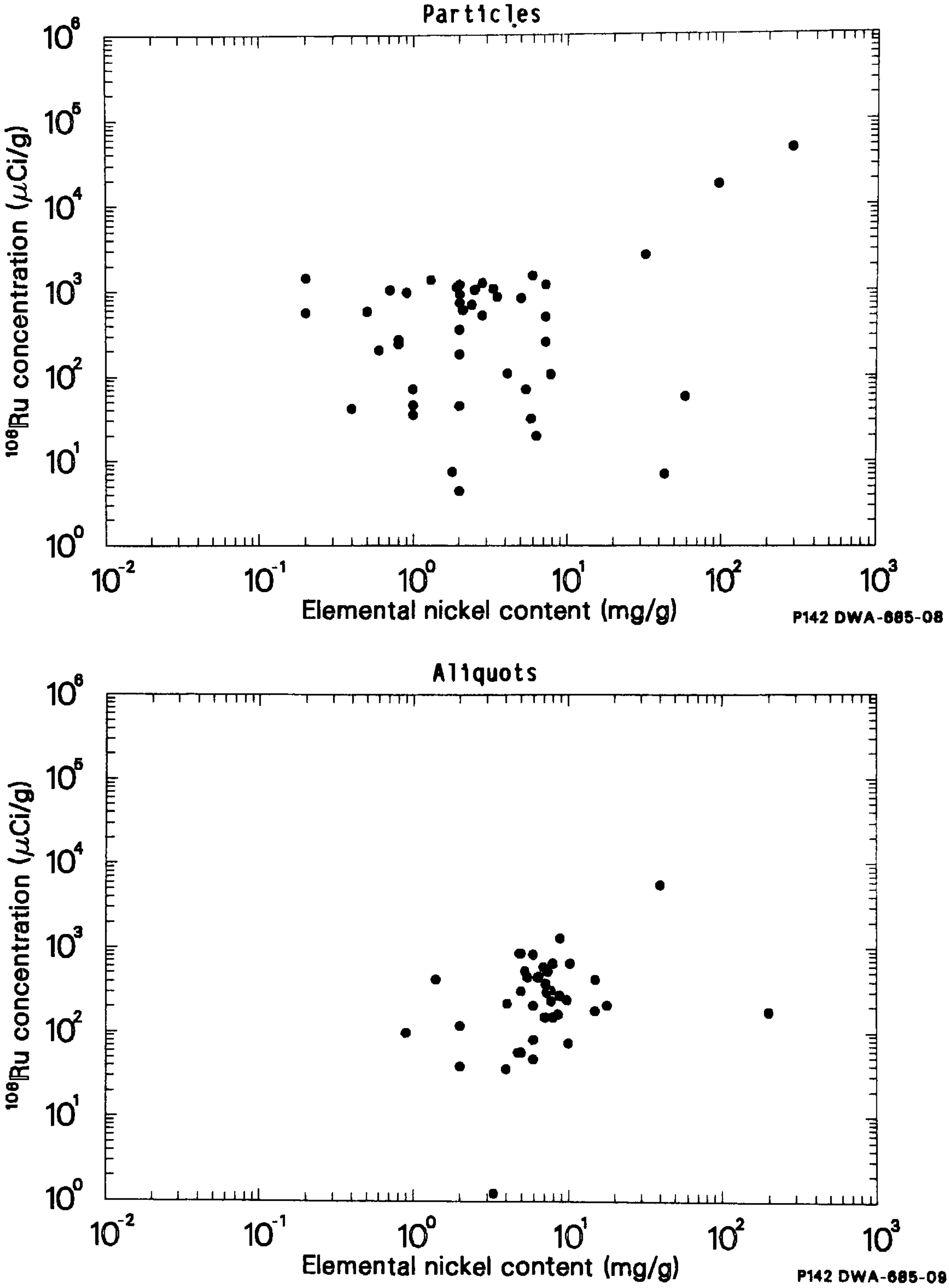

Figure 36. Correlation between Ni content and ^{106}Ru for all particles and aliquots analyzed.

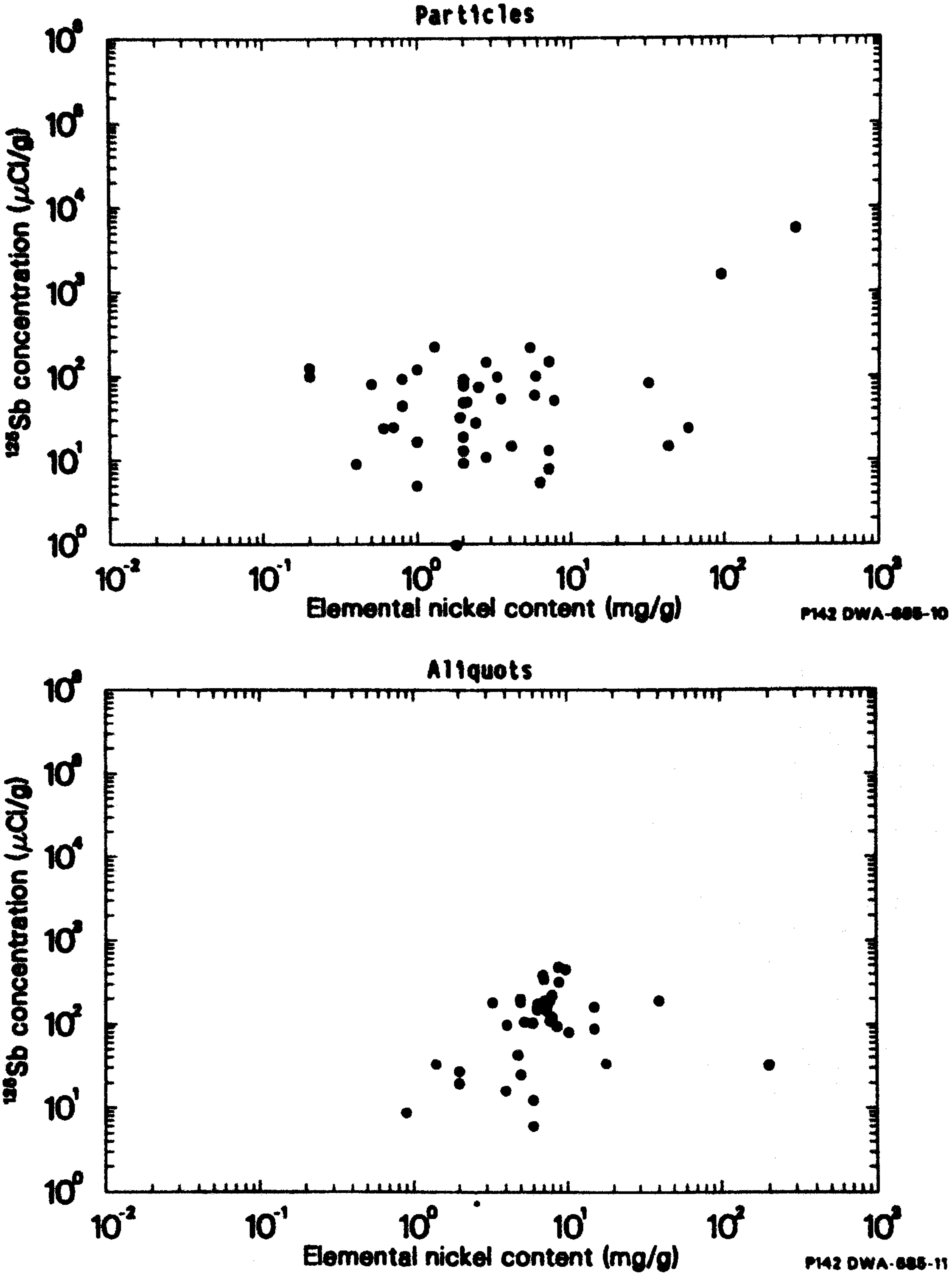

Figure 37. Correlation between Ni content and ^{125}Sb for all particles and aliquots analyzed.

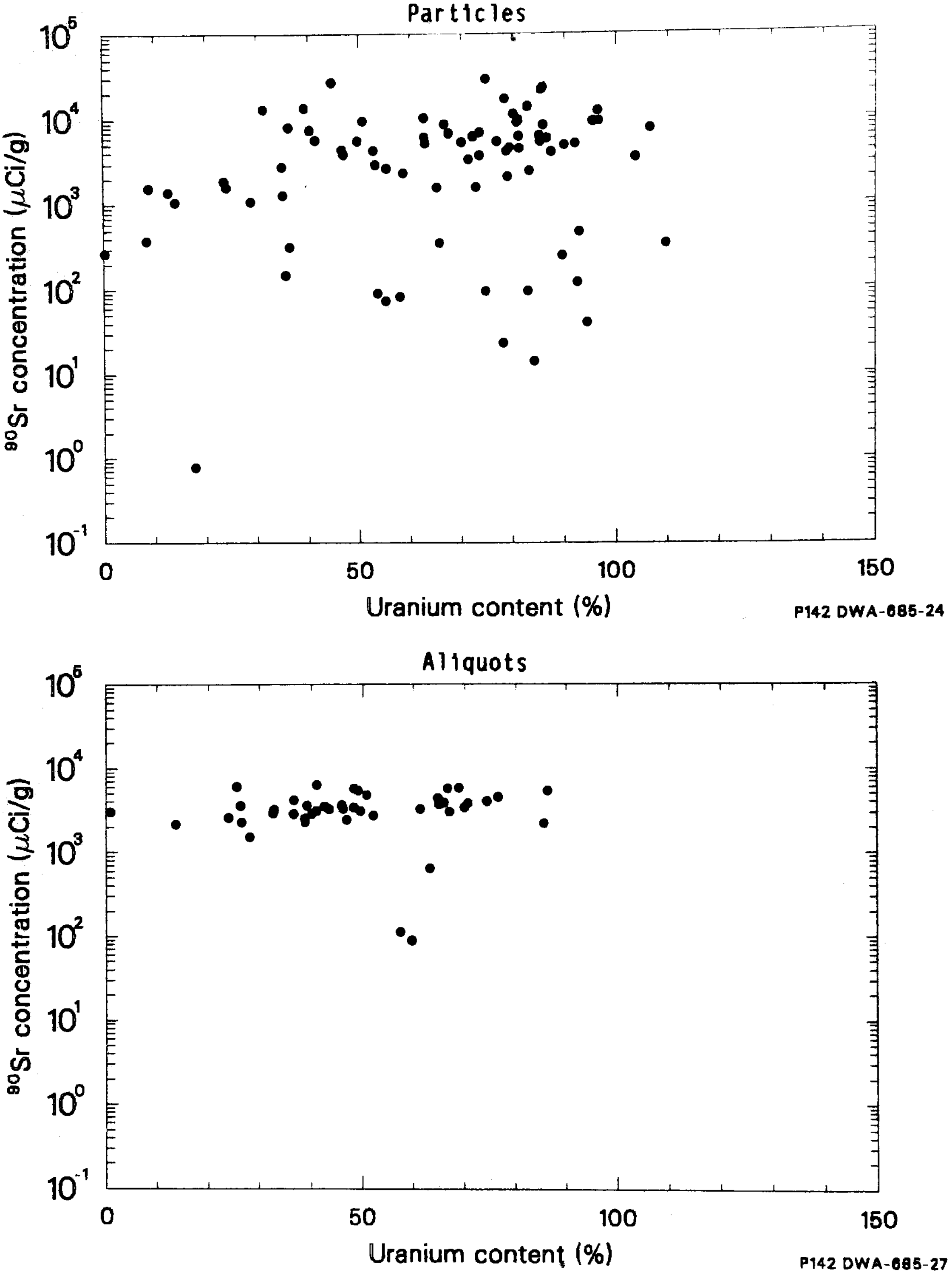

Figure 38. ^{90}Sr/U content correlation for all particles and aliquots analyzed.

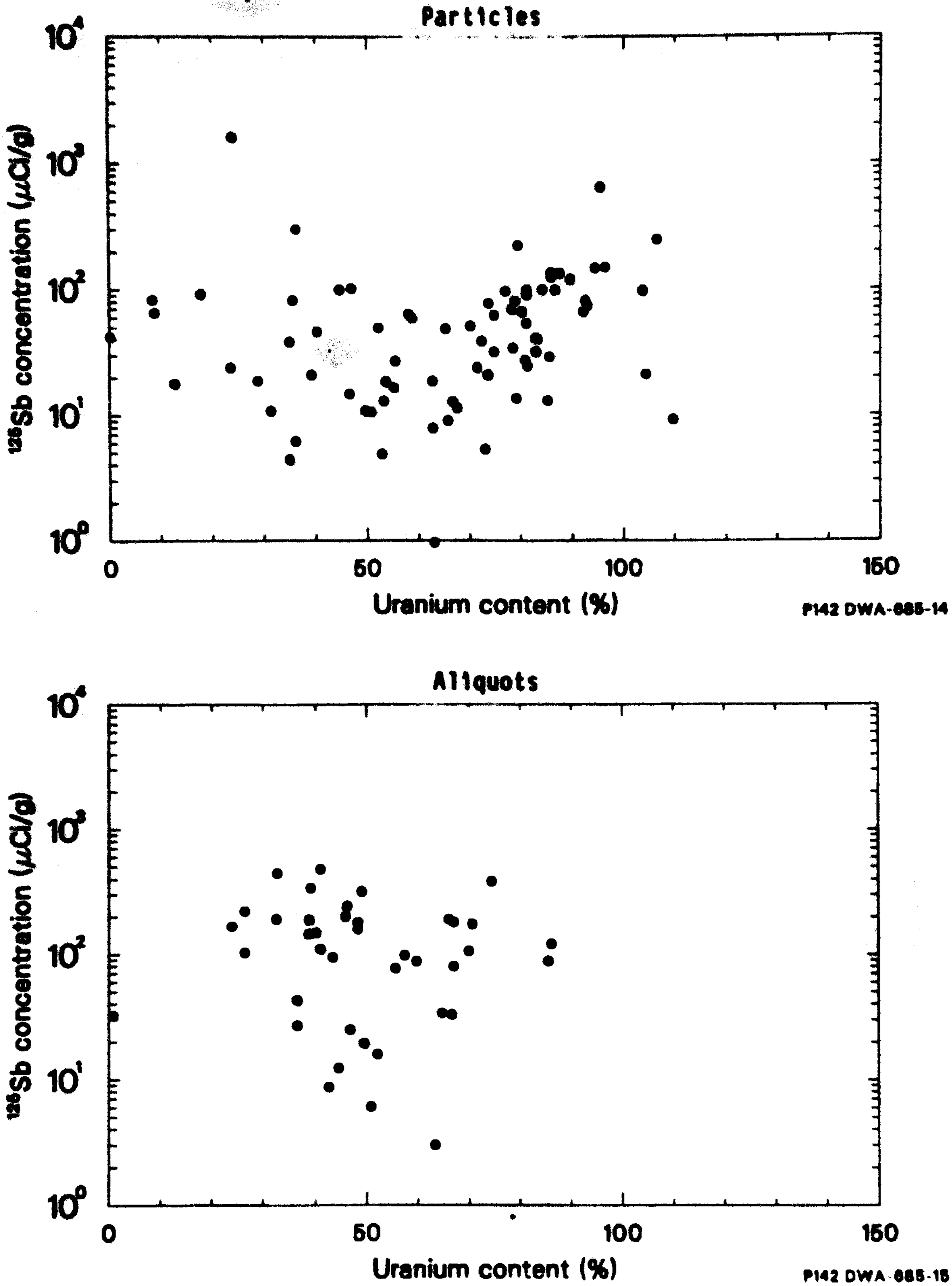

Figure 39. ^{125}Sb/U content correlation for all particles and aliquots analyzed.

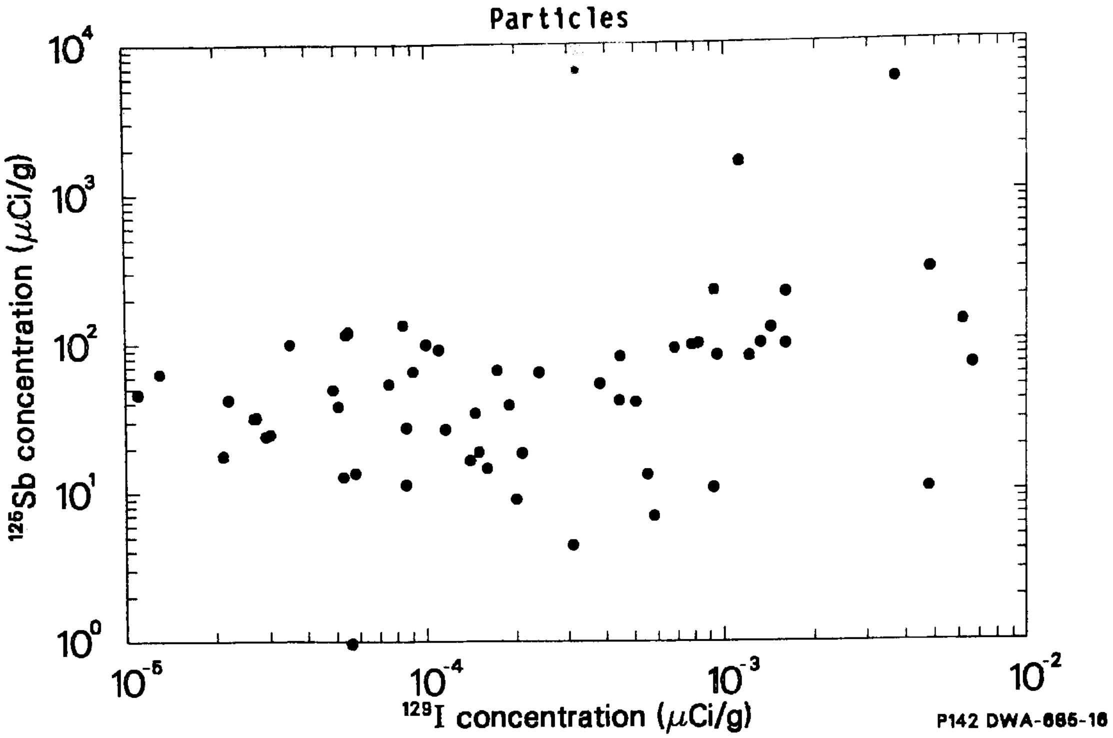

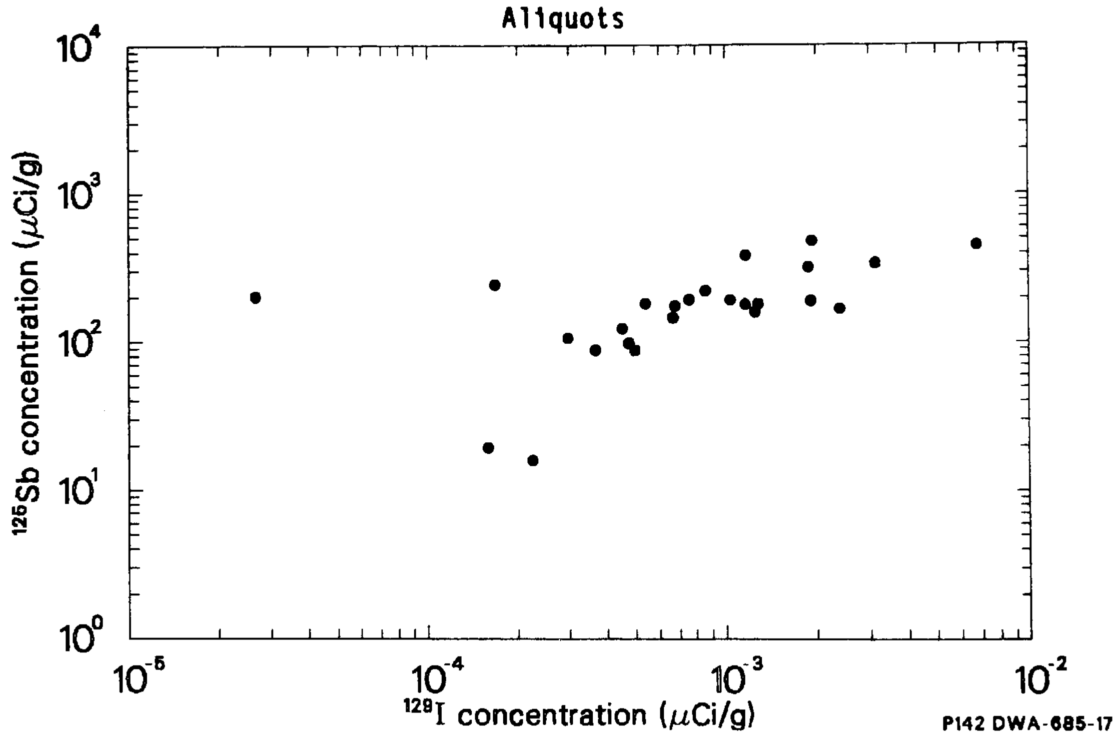

Figure 40. Correlation between ^{125}Sb and ^{129}I for all particles and aliquots analyzed.

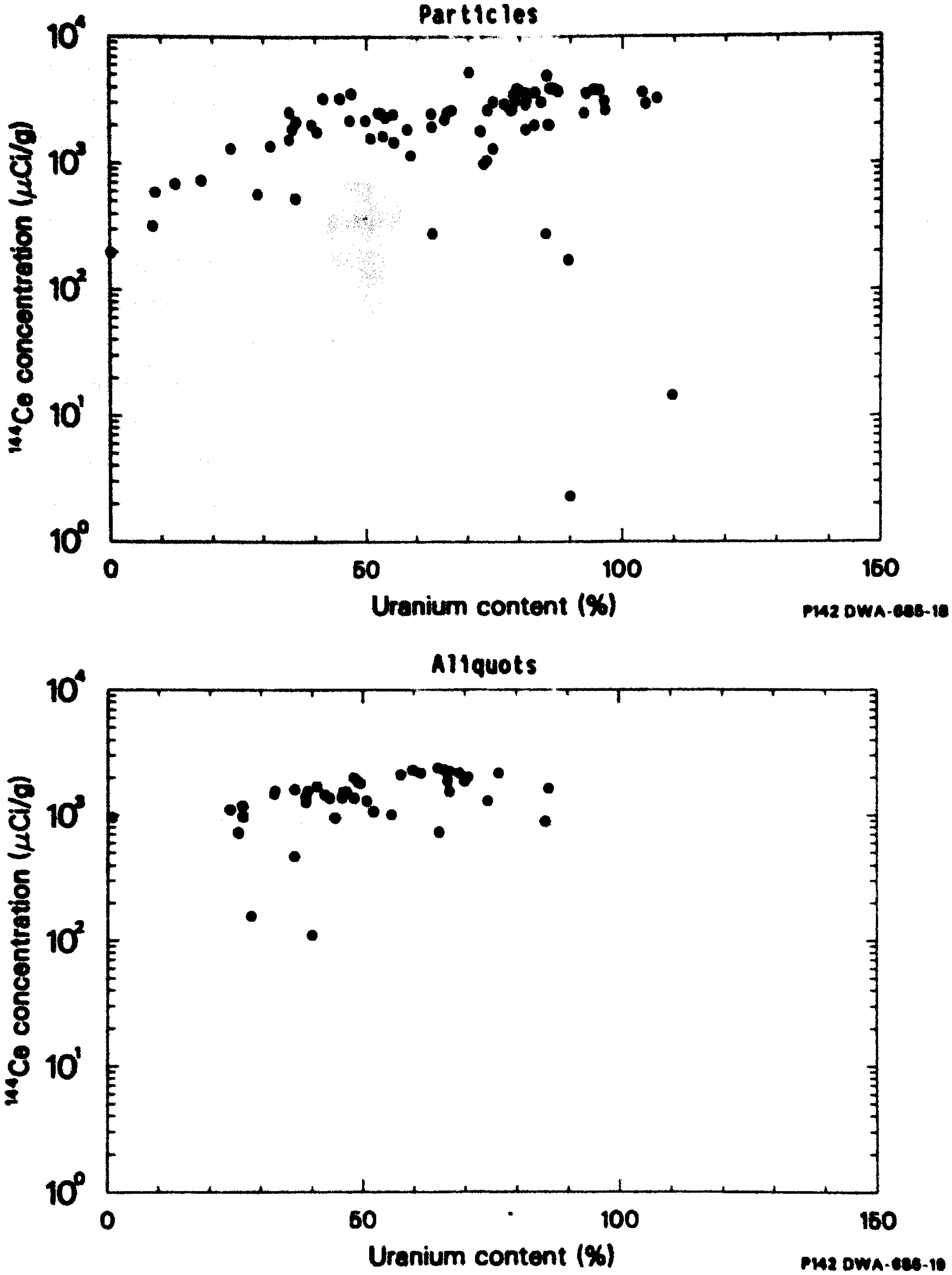

Figure 41. ^{144}Ce/U content correlation for all particles and aliquots analyzed.

TABLE 31. RETENTION OF ^{106}Ru AND ^{125}Sb BY PARTICLES 9D AND 9G

Concentration	Particle 9D	Particle 9G
Ni content (mg/g)	186	94.6
Ag content (mg/g)	16	18
^{106}Ru content (μCi/g)	4.65 E+4	1.77 E+4
Sample 9 ^{106}Ru average concentration[a] (μCi/g)	3.80 E+2	3.80 E+2
Particle/average concentration ratio[b]	1.22 E+2	4.66 E+1
^{125}Sb content (μCi/g)	5.64 E+3	1.61 E+3
Sample 9 average ^{125}Sb concentration[a] (μCi/g)	7.27 E+1	7.27 E+1
Particle/average concentration ratio[b]	77.6	22.1

---

a. Average concentration measured for the bulk sample.

b. Ratio of the concentration in the particle to that of the recombined bulk sample.

appears to be relatively specific to these particles. The retention for ^{106}Ru ranges from 163 to 187 μCi/mg Ni. For ^{125}Sb, the range is 17 to 20 μCi/mg Ni. The Ni to ^{106}Ru and Ni to ^{125}Sb atom ratios are 3.8 E+4 and 6.9 E+5, respectively. This indicates that the ^{106}Ru or ^{125}Sb are located inside the Ni matrix, with many atoms of Ni present for every atom of either radionuclide. Using the retention factors indicated, the core inventory of Ni (~1046 Kg) could retain 1.96 E+5 Ci of ^{106}Ru and 2.09 E+4 Ci of ^{125}Sb. This is equivalent to 170% of the ^{106}Ru core inventory and 56% of the ^{125}Sb core inventory. However, as noted, this is not a general trend and is specific to a few particles. Also it is unlikely that significant amounts of the structural materials would be in contact with the fuel to produce this behavior. Figures 36 and 37 show the correlation between Ni content and ^{106}Ru and ^{125}Sb concentrations.

^{125}Sb and ^{90}Sr exhibit significantly different retention characteristics as indicated in Table 29. The ^{125}Sb appears to be present in greater concentrations in the Zr-bearing than in the U-bearing particles, suggesting significant release from the fuel; whereas, ^{90}Sr appears to be principally retained in the fuel. Figure 38 shows the correlation between ^{90}Sr and U content. There is an apparent reduction in concentration at lesser U content. As shown in Table 30, the ^{125}Sb appears to be scavenged by structural material. Figure 39 shows the relationship between ^{125}Sb and U content. No apparent correlation is present. Figure 40 shows the correlation between ^{125}Sb and ^{129}I in order to determine if these radionuclides (^{129}I and ^{125}Sb) are exhibiting similar behavior. No obvious correlation is apparent.

The Ce and Eu appear to be retained principally in the fuel matrix, as shown in Table 29. However, retention of ^{144}Ce by the Zr material was found on a single particle (Particle 6B). Otherwise, little release from the fuel is indicated. Figure 41 shows the correlations between ^{144}Ce and U content for particles and aliquots. For particles, there is a wide diversity in concentration. Burnup may account for some variation, because the amount of ^{144}Ce produced is directly related to burnup and enrichment. The data indicate a range with relatively high Ce concentrations ($\sim 10^3 \mu Ci/g$) associated with particles of both high and low U content.

3.4.5 Evidence of Core Material Mixing

The effective enrichment calculations discussed in Section 3.4.3 provide evidence of substantial mixing of core materials (see Table 26). Effective enrichment is calculated by dividing the measured fissile material (^{235}U) content of each recombined bulk sample by the total U content obtained from the elemental analysis. There were three fuel assembly enrichments in the TMI-2 core. The peripheral fuel assemblies were 2.96% enriched, and the inner fuel assemblies alternated between 1.98% and 2.64% enriched. At the H8 and E9 locations the original enrichments in the fuel assemblies were 2.64% and 1.98%, respectively. The data indicate a variety of enrichments, suggesting significant mixing of the U from the fuel assemblies. The effect is pronounced at E9 where many of the samples indicate the presence of 2.7% enriched fuel material.

A comparison was performed of the measured enrichments for the particles and aliquots from the various samples. A wide range exists, indicating there is no correlation with the original enrichments at the sampled locations (see Table E-11). Chemical and radiochemical evidence of core relocation are further evaluated in Section 4.

3.4.6 Summary of the Cesium Release and Settling Tests

Cesium release, turbidity, and airborne release tests were conducted on 50 g of recombined bulk sample material from Sample 6. The tests were performed on both the as-received core debris materials and on debris which was crushed to alter the particle size distributions and create freshly fractured surfaces. Crushing was intended to simulate the breakup of TMI-2 core material during reactor defueling. Details of these examinations are reported in Reference 30, and the results are summarized below.

- Crushing the debris increased the concentration of ^{137}Cs in solution by a factor of approximately 10, due to the exposure of freshly created surfaces (by crushing) that allowed leaching into the coolant.

- Turbidity examinations indicate that crushing the debris causes little change in the rate of decrease in turbidity. Also, significant reductions in turbidity occur within 24 hours. These data indicate that crushing the debris during defueling will have little impact on turbidity during defueling operations.

- Airborne radioactivity measurements indicate that production of airborne radioactivity during defueling is expected to be significant only when wetted surfaces are near the point of drying out. Minimizing changes in the volume of reactor coolant in tanks or in the core cavity will reduce the exposure of nearly dry radioactive surfaces and consequently the production of airborne radioactivity in the reactor building.

4. CONTRIBUTIONS TO UNDERSTANDING THE TMI-2 ACCIDENT

The influence of the core debris examinations on understanding the TMI-2 accident scenario, the current condition of the core, and radionuclide retention/release from the fuel and core region is discussed in this section. A brief summary of the current understanding of the accident is presented, followed by sections describing (a) the temperature estimates and fuel behavior, (b) evaluation of core relocation, and (c) radionuclide behavior analyses.

4.1 Current Best Estimate of the TMI Accident

The current state of the TMI-2 core and support structure is based on the following examinations and calculations: (a) closed circuit (CCTV) inspections of the upper and lower plenum and core regions; (b) topography measurements of the core cavity; (c) examinations of leadscrews and leadscrew support tubes; (d) mechanical probing of the debris bed to determine the debris depth at 17 locations; (e) measurements from online instrumentation; (f) probing of selected instrument guide tubes with small diameter (piano) wire to determine penetrability of the core from below the reactor vessel; (g) gamma scans of the lower vessel region and reactor coolant system to identify potential fuel deposits outside the active core region; (h) visual examination of the plenum assembly; and (i) computer code calculations and hypotheses.[31]

The known physical condition of the reactor core is summarized in Figure 42. A void is present in the upper region of the core, with a volume of approximately 25% of the total core volume.[32] Examinations of the microstructure of two control rod drive leadscrews (central and mid-radius) indicate that structural temperatures in the upper plenum ranged from 700 K in the upper regions to 1350 K in the lower regions just above the core.[33] CCTV inspections show nonuniform damage to the bottom of the plenum assembly, ranging from areas with no damage to areas where extensive melting and oxidation of the stainless steel occurred. The damage zones appear to be limited to the lower few centimeters of the plenum assembly.

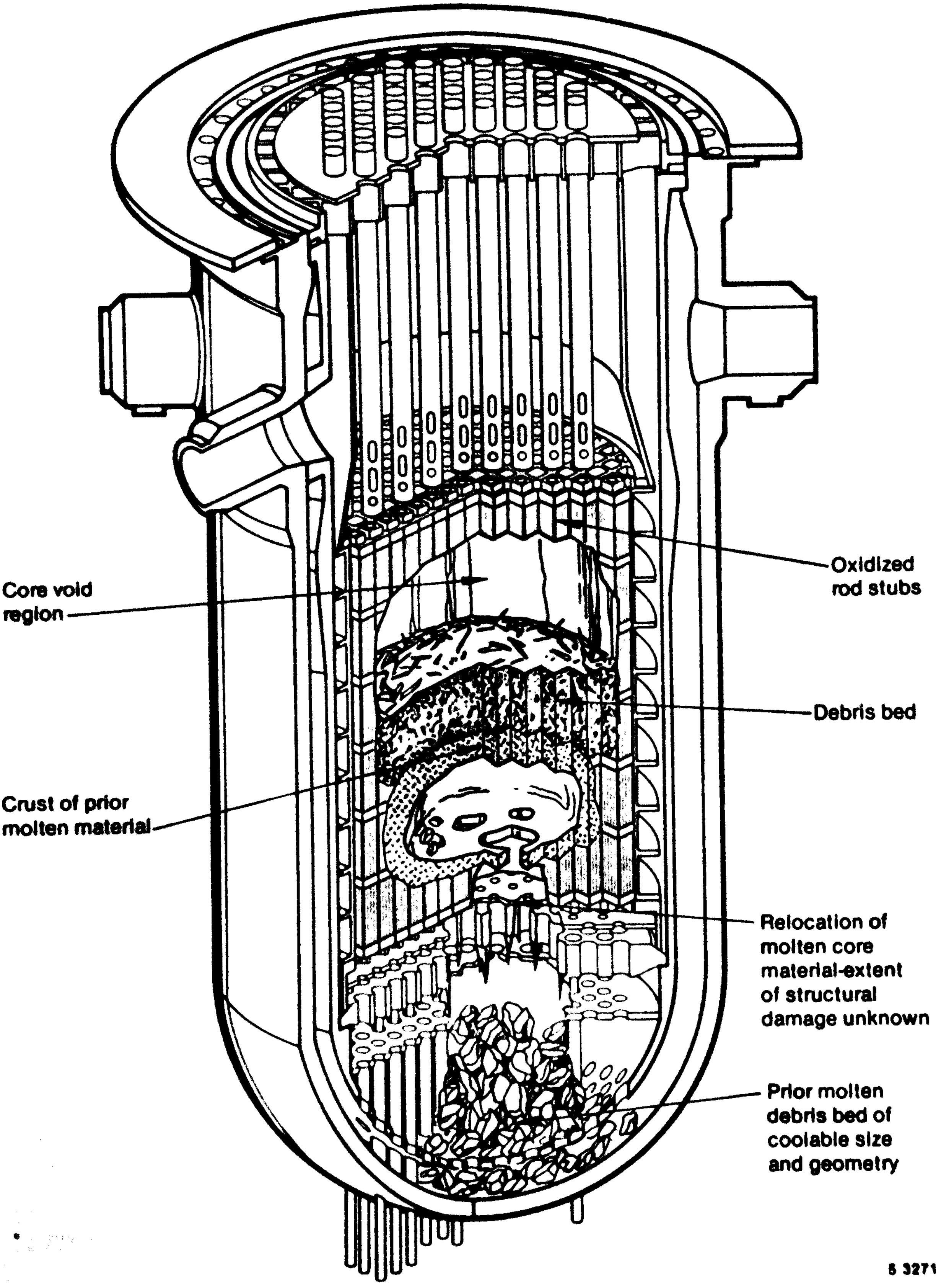
Core void region
Oxidized rod stubs
Debris bed
Crust of prior molten material
Relocation of molten core material-extent of structural damage unknown
Prior molten debris bed of coolable size and geometry
5 3271

Figure 42. Schematic showing the known and best estimated end-state condition of the TMI-2 core.

A debris bed ranging from 0.8 to 1.0-m thick exists at the bottom of the void. The debris bed is resting on a layer of hard (impenetrable) material at about the mid-core elevation. The condition of the lower core is not known.

CCTV inspections of the lower regions of the reactor vessel indicate that 10 to 20% of the fuel and/or structural materials of the core now reside on the reactor vessel lower head, approximately 2.2 m below the bottom of the original core region. The particle size and texture of the material in the lower plenum appears to vary significantly, ranging from pea-like gravel near the center of the vessel to larger pieces of lava-like material up to about 13 cm in diameter near the periphery. Possible damage to the core support assembly is not known because the central regions of the lower plenum were not visible in the video scans. There is no evidence that the lower reactor vessel head has been damaged.

A scenario for the first four hours of the TMI-2 accident was developed based on (a) end-state conditions of the core and reactor vessel (as described above), (b) measurements of the plant response recorded during the accident, (c) the results of best-estimate calculations of the accident,[34] and (d) severe fuel damage experiments conducted in the Power Burst Facility at INEL.[35] Important events and features of the accident are summarized here for later comparison with the information obtained from examining the core debris grab samples. Details of the accident before core uncovery are discussed elsewhere.[36]

Core uncovery began about 100 min after reactor scram. Superheated steam in the hot legs was initially measured at about 113 min. Best-estimate predictions indicate that core temperatures probably increased sufficiently to result in fuel rod ballooning, rupture, and release of gaseous fission products by about 140 min. Radiation measurements indicated a significant release of fission products into the containment at about 142 min. By 150 min, the predictions indicate that peak cladding temperatures rapidly increased due to cladding oxidation and fuel rod temperatures exceeded the melting temperature of zircaloy. The molten zircaloy would have dissolved a portion of the UO_2 fuel pellets. The dissolved fuel and molten zircaloy flowed downward along the fuel rods and eventually froze in lower, cooler regions of the core. The lower level of the previously molten materials was probably coincident with the coolant liquid level which was estimated to be in the lower third of the core. The predictions indicate that a significant portion of the core (1/4 to 1/2) reached temperatures sufficient to melt the cladding and that the core maximum temperature was sufficient to melt the UO_2 fuel.

One of the reactor coolant pumps was turned on from about 175 to about 180 min resulting in some coolant flow into the core. Thermal and mechanical shock in the upper regions of the core which consisted primarily of highly oxidized and embrittled rod remenants caused extensive fragmentation and collapse of the rods. The core continued to heat up after the pump transient (as indicated by the incore thermocouples). The relatively solid mass in the bottom of the core eventually melted through the bottom supporting crust, and molten material flowed into the lower plenum at about 227 min. A coolable geometry was attained in the lower plenum, and long term cooling was reestablished at about 16 h into the accident.

Three concepts are unique to this accident scenario. First, based on an understanding of cladding melting and fuel liquefaction, significant portions of the core probably flowed downward into lower portions of the core and solidified within the confines of the lower core boundary prior to the pump transient. This region of liquefied core materials and intact fuel rods could have been of substantial size, from 1 to 2 m in height and from 80 to 90% of the core diameter. Second, because of the thermal properties of the core materials, these large zones containing metallic Zr and ceramic materials probably were not coolable (using reasonable decay heating assumptions), even when surrounded by water. Third, the large solid mass continued to heat up and eventually a significant fraction of the core relocated through the core support assembly into the lower plenum, where a coolable configuration was attained.

4.2 Impact of Metallurgical Findings on Understanding the Accident Scenario

The metallurgical analysis of 29 particles from the core debris grab samples provided information in several areas that relate to the accident scenario. Estimates were made of core peak temperatures achieved during the accident, some indiction of the temperature history was obtained, information on the chemical interactions of the fuel rod material with other core materials on a microscopic scale was obtained, and details of the relocation phenomena were investigated. This section compares results of the metallurgical examinations to the scenario described in Section 4.1. The comparison is presented in two sections: temperature estimates and fuel behavior.

4.2.1 Temperature Estimates

The peak temperature or temperature range achieved during the transient was determined by detailed analysis of the microstructure and elemental composition of the particles. The selection of particles for examination was biased in that particles showing some indication of melting were usually selected. Although most of the 29 particles showed evidence of high temperatures, examination of the bulk samples indicated that a large fraction of the material contained fuel particles probably exposed to peak temperatures of about 2200 K for a short time. Many of the fuel pellet fragments within the melt-bearing particles display little or no equiaxed grain growth, which confirms that the entire core did not experience prolonged times at extremely high temperatures. However, there are particles that show microstructures indicating peak temperatures up to the melting point of the UO_2 fuel. In addition, the evolution of other particles involved oxidation and mixing processes that cannot be readily explained except by lengthy durations under very severe conditions. Both sets of observations are consistent with the postulated accident scenario.

Evidence was found of molten Zr which had flowed down interior cladding surfaces, within the fuel-cladding gap. This phenomenon is important in calculating peak temperatures, as well as in estimating fuel liquefaction and fission product release. The longer the molten metallic zircaloy cladding remains in place, the more heat is generated by the exothermic Zr-steam reaction. Containment of molten Zr between UO_2 fuel and an exterior ZrO_2 crust therefore tends to increase peak fuel rod temperatures. Cladding ballooning occurred during the transient, as evidenced by the pieces of deformed cladding found in the debris. The ballooning may have enhanced retention of the molten, unoxidized Zr, thereby driving the temperatures even higher.

4.2.2 Fuel Behavior

Significant interaction (i.e., formation of eutectic mixtures) of the fuel rod materials with structural materials was observed on a microscopic scale, with the eutectic material frequently located in the grain boundaries. Interaction with the Inconel spacer grids seemed to be common, with appreciable amounts of Ni, Fe, and Cr often detected within prior molten regions. This correlates with the CCTV inspection of the upper void, which shows many of the fuel rod assemblies severed at a grid spacer. It is expected that closer inspection will show chemical interaction of the fuel rods with the grid spacer material. Current severe accident analysis computer codes do not adequately model the interaction of the fuel rods with all of the reactor structural components. Nevertheless, these observations on fuel-structural interactions are consistent with results of in-pile and out-of-pile research on severe core damage accidents which are presently being conducted (see Reference 35).

Many particles exhibit distinct prior molten layers of significantly different compositions, where typically one molten mixture solidified (and often oxidized) before being contacted by a second fuel-bearing melt. Interactions between such layers were found to vary from moderate-temperature diffusion bonding to thermo-chemical dissolution at much higher temperatures. These particles indicate either multiple temperature excursions, separated by oxidation and solidification periods or a prolonged candling sequence during the TMI-2 accident, where droplets of liquefied fuel had sufficient time to relocate down fuel rod exteriors, chemically react, solidify, and oxidize before other droplets arrived. On certain particles, structural material content differs markedly between layers such that limited lateral movement of the molten material may also have occurred. In any case, these layered particles are not typical of in-pile and out-of-pile experiments that confine fuel liquefaction and solidification to a brief continuous process. Consequently, melt relocation during the high temperature portion of the TMI-2 accident should not be viewed as a single core-wide event, but rather as a complex sequence of interrelated and possibly intermittent phenomena. The short "B" coolant pump operation and the occasional Emergency Core Cooling System flows may have locally rekindled or temporarily accelerated Zr-steam oxidation, thereby creating this particle type.

The occurrence of hyperstoichiometric fuel (independently measured on TMI-2 particles at three laboratories) is another major difference from in-pile and out-of-pile research efforts to date. These experiments uniformly involve reducing environments, with Zr oxidation creating strong competition for the oxygen from available steam and from UO_2 dissolution. However, the current understanding of fuel oxidation requires a surplus of oxygen in order to produce oxides above $UO_{2.1}$. Moreover, the extent of the fuel oxidation on certain particles ($\geq UO_{2.4}$) presumes that the free oxygen supply was maintained for an extended period at elevated temperatures (approximately 2000 K). Candidate mechanisms for producing free oxygen within the TMI-2 primary coolant system have not yet been identified.

4.3 Evaluation of Core Relocation

Knowing the extent of core materials relocation is important to understanding the current condition of the core and postulating a viable scenario for the accident. The metallurgical, chemical, and radiochemical data provide evidence of extensive mixing, bulk material relocation, and segregation of core materials during the accident. Each of these three types of relocation is evaluated, and their impacts on understanding the condition of the core and accident scenario are addressed.

4.3.1 Mixing of core materials

Evidence of mixing of core materials has been obtained principally from the metallurgical and chemical analyses results (Sections 3.2 and 3.3). The metallurgical data (SEM/EDS and SAS) indicate the presence of structural (Cr, Fe, Ni), poison rod (Gd, Al), and control rod (Ag, In, Cd) materials in regions of ternary U-Zr-O mixtures, at grain boundaries or on surfaces within the voids of many particles. These data suggest that the structural materials and Al were incorporated into the particles as a result of fuel rod melting and dissolution, or the formation of low melting temperature eutectics.

Elemental analysis of the particles and aliquots indicates the presence of most structural materials in each sample at relatively low concentrations ($\leq$1.0 wt%). The uniformity of the structural material concentrations in most particles and aliquots indicates that structural and control rod materials were probably mixed into the debris when the material was molten. These data also suggest that the debris bed was thoroughly mixed for a substantial period of time during the accident to achieve the degree of homogeneity observed for the core constituents.

The distribution of the Gd from the burnable poison rods (Gd_2O_3-UO_2) provides additional evidence of significant mixing of core materials. Only about 13.5 kg of Gd was originally contained in the core, at four widely separated locations (H4, H12, D8, and N8). Gadolinium, however, was measurable in similar concentrations in most of the recombined bulk samples from the H8 and E9 locations. The distances from the H8 and E9 locations to the center of the nearest Gd fuel assembly are 87 cm and 30 cm, respectively. The homogeneity of the Gd concentrations in the samples supports the hypothesis that the core materials were subjected to significant turbulent mixing during the accident but after high temperatures had existed because the Gd (either as Gd_2O_3 or as reduced Gd) was transported to the H8 location and mixed to a concentration similar to what was measured in debris taken from the E9 position. The relocation of the Gd in the core could have occurred via several mechanisms. Gadolinia (melting point ~3000 K) may have been either melted or reduced by molten Zr to Gd and subsequently distributed throughout the debris bed.

Analysis of the mixing of core materials contributes to understanding of core condition as follows:

- Based on the distribution of core structural materials and their presence in the ternary U-Zr-O structures, the debris bed was at one time probably subjected to significant turbulent mixing when the material was partially or completely liquefied.

- The turbulent mixing of core materials probably occurred during the B-2 pump transient between 175 and 180 min. The relatively uniform concentrations of Gd suggest that the mixing was very vigorous and extensive.

4.3.2 Bulk Relocation of Fuel

Bulk relocation of fuel is suggested from the previous discussion on mixing and from the average enrichment (^{235}U/total U x 100%) of the recombined bulk samples (see Table 26). The previous discussion concludes that turbulent mixing of core materials probably occurred in order to achieve the observed uniform distribution of core constituents. The ^{235}U enrichments were also determined for the recombined bulk samples for comparison with the original core enrichments at H8 (2.64 wt%) and E9 (1.98 wt%). The measured enrichments of samples from the H8 location ranged from 2.3 to 2.7 wt% ^{235}U and at E9 the measured enrichments ranged from 2.5 to 2.8 wt% ^{235}U. There is no appreciable correlation between the original enrichments, particularly at E9, and measured sample enrichments. These results indicate that fuel from low enrichment has been thoroughly mixed with higher enrichment fuel from other assemblies. For example, the 2.98 wt%-enriched fuel was originally only at the core periphery. Materials with this enrichment are now found in most of the samples examined. The results indicate that significant degradation and mixing of bulk fuel assembly components has occurred.

4.3.3 Segregation of Core Materials

The elements for which segregation or accumulation was indicated, primarily by the chemical analysis results, are Zr, Ag, In, Cd, Gd, and Al. Less than 50% of the anticipated Zr was present in the debris bed at some H8 and E9 locations. Fuel rod temperatures were probably high enough after approximately 150 min for zircaloy cladding to melt, dissolve some UO_2, and flow downward along the rods into lower cooler regions of the core. The chemical analysis results support this scenario and suggest that depletion of materials was significant from the upper portion of the fuel rods in the region of the debris bed. Based upon this result, there may be zones lower in the core which contain significant accumulations of the U-Zr-O ternary mixture. The debris bed contains approximately 20% of the core mass and based upon the indicated depletion of Zr, approximately 500 to 2200 kg of Zr with dissolved U may have been deposited near the bottom of the core prior to the B-2 pump transient at 175 min.

The control rod constituents (Ag-In-Cd) are relatively volatile, and based on thermodynamic calculations for conditions similar to TMI,[37] significant amounts of Ag (24%), In (47%), and Cd (100%) could vaporize, condense into aerosols, and be transported out of the core region. The results of the recombined bulk sample analysis indicate the presence of only 7.4 to 10.1% of the initial core concentration of Ag in the core debris grab samples. [Cd and In were not measurable in the recombined bulk samples, probably because the concentrations were below the detection limit.] Evidently, approximately 90% of the Ag has been transported from the debris bed (~400 kg Ag). Less than 3% of the core inventory of Ag left the reactor vessel based upon analyses of components outside the core [leadscrew surfaces, (see Reference 33) reactor coolant drain tank and reactor building basement,[38]] where the Ag would tend to accumulate if transported as a vapor or aerosol out of the core. The silver probably melted and flowed into lower regions of the core or reactor vessel where it probably remains.

The concentration of Ag tends to be higher for the smaller (<1000 μm) particle size fractions possibly because of the increased surface area for condensation on the particles with decreasing particle size. The Ag could also react chemically with the particles and a similar trend would be indicated. The data indicating whether the interaction is physical or chemical do not yet exist. Cd and In, the other principal control rod constituants, were measurable in the particles and aliquots; but in fewer samples than was Ag. These elements exhibit essentially the same behavior as Ag, with higher concentrations associated with the smaller particle size fractions.

Gadolinium, a poison material, was present in most recombined bulk samples. It was distributed relatively evenly, with measured concentrations ranging from 4.7 to 8.2 E-2 wt%. This is surprising as gadolinium constitutes less than 1.1 E-2 wt% of the core and the measured concentrations are significantly higher than the initial core average concentration. No correlation with particle size is apparent. Extrapolation of the measured concentrations to the weight of the debris bed indicates that the core inventory of Gd could be contained in the debris bed. It is possible that Gd was concentrated in the debris bed at the sample locations and that large areas with little or no Gd present exist at other locations in the core.

Aluminium, the other primary constituent of the poison rods (excluding O), appears to have behaved differently than gadolinium. Aluminum was measurable only in the two recombined bulk samples of surface material, at 7 to 20 times the concentration expected if the Al were evenly distributed in the debris bed. Tellurium also was concentrated at the surface the debris bed. In general, the concentration of Al increases with decreasing particle size as indicated in Figure 43. This figure is a comparison

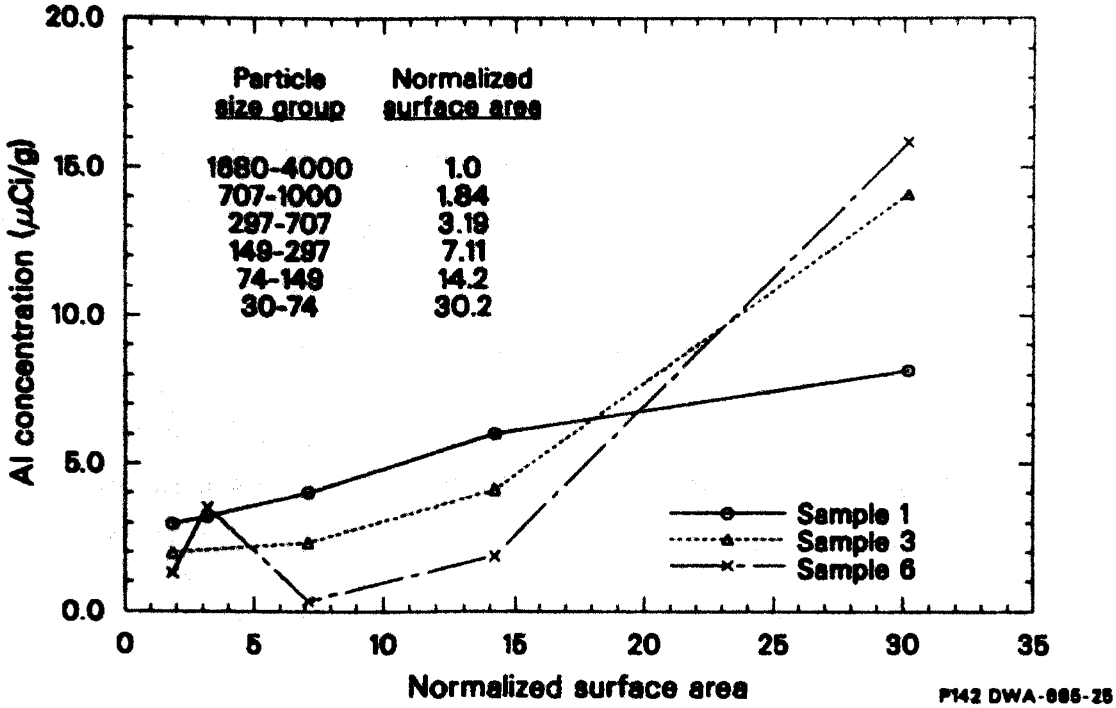

Figure 43. Comparison of Al concentrations with normalized surface area.

between the normalized particle surface area and the concentrations of Al for Samples 1, 3, and 6. The deviations in the general increase in concentration with decreasing particle size may be due to differences between the actual and calculated surface areas of the particles. These data suggest that the transport mechanism may have been vaporization within the high temperature zone and condensation at the top of the cooler rubble bed.

These results contribute to an enhanced understanding of the core condition and accident scenario as follows:

- The distribution of Zr, Ag, Al, and Gd within the debris bed indicates that the unexamined regions in the lower half of the core and lower plenum probably have significantly different compositions than does the debris bed. For instance, most of the Zr and Ag which is missing from the core material in the debris bed is probably in the bottom of the core and lower plenum. The core material in these lower regions is probably depleted in Al and Gd.

- Concentration of Al and Te in the surface material of the debris bed suggest that the surface of the debris bed functioned as a trap for some of the materials which were vaporized within the high temperature zone of the core.

- The concentration of Al, Ag, Cd, and In with the smaller particle size fractions suggests that the mechanism was strongly dependent upon particle surface area. The most likely mechanisms are probably condensation or chemical reaction of vapors.

4.4 Behavior of Fission Products in the Core

Fission product behavior is defined as the retention/release from the fuel and transport/retention of radionuclides within the reactor pressure vessel and primary cooling system. A block diagram which summarizes the fission product behavior, as determined from analysis of the core debris grab samples, is shown in Figure 44. The only measurable radionuclides significantly released from the reactor vessel are ^{137}Cs and ^{129}I. Other radionuclides were retained within the vessel, either in the fuel or associated with the cladding and structural materials. The release of ^{106}Ru and ^{125}Sb from the fuel is significant. Behavior of each of the radionuclides and their impacts on the current understanding of the core condition and accident scenario is evaluated in this section. The chemistry associated with the observed behavior is evaluated in References 39, 40, and 41.

4.4.1 Cesium and Iodine

^{137}Cs and ^{129}I were expected to be the most volatile radionuclides (except for the noble gases) and, hence, the most mobile of the measurable radionuclides. Estimates of radionuclide retention in the core debris, as shown in Figure 44, indicate that the maximum retention in the debris bed for ^{137}Cs and ^{129}I is 28 and 32%, respectively. Significant fractions of the core inventory of both radionuclides have been relocated by the reactor coolant to the remainder of the reactor system (see Reference 28). Also, the radiochemical analyses (see Section 3.4) indicate that both radionuclides have become associated with cladding and structural materials at concentrations similar to fuel material (i.e., the structural materials have ^{129}I and ^{137}Cs concentrations similar to fuel material).

Comparing the ^{137}Cs/^{129}I ratios for high fuel content (>50%) samples indicates no correlation between ^{137}Cs and ^{129}I. This suggests that the radionuclides were removed from the fuel material to different extents or subsequent leaching has affected the distribution. Under highly oxidizing conditions as were indicated at TMI by the degree of cladding oxidation, I^2 would probably preferentially be formed rather than CsI indicating different transport methods. The core debris data tend to support this hypothesis. There appears to be a general increase in ^{129}I associated with the smaller particle size fractions (see Section 3.4); however, no similar relationship exists for ^{137}Cs. If the correlation with the particles size fraction (i.e., surface area) is evidence of

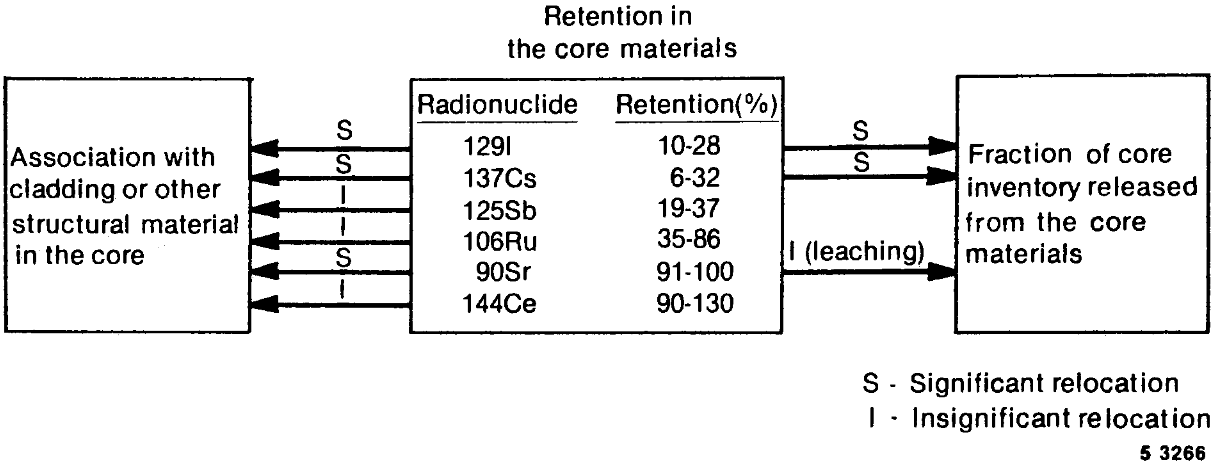
Retention in
the core materials
Association with
cladding or other
structural material
in the core
Radionuclide
Retention(%)
129I
10-28
137Cs
6-32
125Sb
19-37
106Ru
35-86
90Sr
91-100
144Ce
90-130
S
S
I
I
S
I
S
S
I (leaching)
Fraction of core
inventory released
from the core
materials
S - Significant relocation
I - Insignificant relocation
5 3266

Figure 44. Schematic showing the behavior (retention/relocation) of various radionuclides in the TMI-2 core.

vaporization/condensation, these data suggest that ^{129}I vaporized and subsequently condensed on the surfaces of the smaller particles, whereas ^{137}Cs did not deposit as a vapor or was selectively removed by leaching or other mechanisms.

The contributions of the ^{137}Cs and ^{129}I results on understanding the core condition and accident scenario are as follows:

- ^{134,137}Cs and ^{129}I have been significantly removed from the fuel and have become associated with cladding and structural materials or transported outside the vessel, with no correlation between the two.
- The data suggest that ^{129}I may have deposited as a condensed vapor on surfaces or reacted with components of the smaller particles size fractions to form an insoluble material not removed by leaching.
- Previous experiments have indicated that release of Cs and I from the fuel occurs after fuel fracture and quenching.[42] The most significant release probably occurred at 175 min into the accident during the B-2 pump transient.

4.4.2 Ruthenium

^{106}Ru release from the debris was quite significant (14 to 64%). However, ^{106}Ru is measurable to a minor extent in cladding and structural material samples, suggesting some retention by other core constituents. Significant retention of ^{106}Ru in the debris was observed for several isolated particles. For particles 9D and 9G, the Ni to ^{106}Ru retention was much greater (10 - 100 times) than would be found in a comparable particle of U, indicating that Ni scavenges ^{106}Ru and incorporates it into the Ni matrix. Extrapolation of the measured retention factors for ^{106}Ru to the core inventory of Ni indicates the potential retention of the total core inventory of ^{106}Ru by the Ni present in the core. It is unlikely, however, that all ^{106}Ru present in the core would be contacted by structural Ni, indicating that this is a less significant potential retention mechanism.

The low retention of ^{106}Ru in some samples indicates that significant ^{106}Ru depletion has occurred from the debris bed. No significant amount of this radionuclide has been measured outside the reactor vessel, suggesting that the ^{106}Ru in the debris bed may have been transported to lower in the core. A possible transport mechanism is that the ^{106}Ru reacted with Zr or structural material and was transported to lower regions of the core with those materials. Although Ru metal has a high boiling point with very low volatity, it has ∿10 oxidation states which are highly volatile, unstable chemical compounds (see Reference 40). Formation of those chemical compounds may account for the ^{106}Ru depletion in the debris bed.

Contributions of the ^{106}Ru results to understanding the core condition and accident scenario are as follows:

o ^{106}Ru is significantly retained in the fuel; however, what has been released probably reacted with structural materials and has been retained within the reactor vessel or near vicinity

o ^{106}Ru depletion in some samples indicates that a portion of the core inventory of this radionuclide may have been transported to lower in the reactor vessel.

4.4.3 Antimony

The ^{125}Sb results indicate significant release of this radionuclide (63 to 81%) occurred from the debris bed. The release was similar to ^{137}Cs; however, no significant fraction of the core inventory of ^{125}Sb has been measured outside the reactor vessel. This radionuclide also behaves similarly to ^{106}Ru in that it leaves the fuel and associates with cladding and structural materials. The Ni to ^{125}Sb atom ratio is $\leq$6.9 E+5:1, suggesting that ^{125}Sb also is incorporated into the Ni matrix. Extrapolation of the measured retention factors of Ni for ^{125}Sb indicates that as much as 56% of the core inventory of ^{125}Sb could have been retained by structural materials containing Ni.

The data suggest that the missing portions of the core inventory may have reacted with Zr or structural material and have been transported to lower regions of the core when these materials were relocated.

The contribution of the ^{125}Sb results to understanding the core condition and accident scenario is that a large fraction of the ^{125}Sb inventory of the debris bed (60 to 80%) has not been accounted for. The data indicate that the ^{125}Sb reacted significantly with structural materials and may have been deposited on those materials within the core region or has been transported to lower in the reactor vessel with the relocated cladding and structural materials.

4.4.4 Strontium

^{90}Sr has been significantly (> 90%) retained in the fuel and has not become associated with cladding or structural materials, as determined from the analyses in Section 3.4. However, a continuous addition of ^{90}Sr to the reactor coolant has been measured (see Reference 26), suggesting that this material leaches directly into solution and does not react with Zr or cladding significantly. No significant accumulations of ^{90}Sr have been measured outside the core. The oxidizing conditions at TMI would tend to form SrO (see Reference 40), which has very low volatity. Formation of this compound with no subsequent reduction with Sr may be the reason for the low volatility of the ^{90}Sr at TMI.

The contribution of the ^{90}Sr results to understanding the core condition and accident scenario is that ^{90}Sr was retained in the fuel and was not released during the accident. The data suggest that ^{90}Sr is not an immediate hazard during a severe core damage accident similar to TMI-2 and is only slowly leached from the fuel into the coolant.

4.4.5 Cerium

^{144}Ce appears to have been completely retained (90 to 130%) in the reactor vessel. The results indicating retentions of greater than 100% may be due to localized variations in burnup or possible relocation of ^{144}Ce from the fuel. An evaluation of ^{144}Ce relocation was performed in Section 3.4, indicating that ^{144}Ce was released from the fuel and has become associated with cladding and structural materials in the core. ^{144}Ce probably formed CeO a relatively high volatity compound (see Reference 37) from Ce_2O_3. CeO would probably be produced by the reduction of Ce_2O_3, a very stable, low volatility compound. The oxidation of the cladding and core materials would indicate there was a generally oxidizing environment; however, the ^{144}Ce data suggest the presence of a time during the accident when a reducing atmosphere was present in the debris bed to produce the observed ^{144}Ce mobility.

Contributions of the ^{144}Ce results to understanding the core condition and accident scenario are that no significant release of ^{144}Ce from the core occurred. What little did escape from the fuel matrix reacted with nearby cladding and structural material and was retained in the reactor vessel. The higher concentrations of ^{144}Ce in the debris bed may indicate the presence of periods of time during the accident when a reducing atmosphere was present.

5. OBSERVATIONS/CONCLUSIONS

Principal observations and conclusions that have been obtained from examining the core debris grab samples include results of the physical, metallurgical, chemical, and radiochemical analyses and correlation of these results with current information on the known core condition and accident scenario. The principal observations/conclusions include the following:

- Approximately 80 wt% of the debris material is greater than 1000 µm in size. The largest particles were up to 20 mm in size.

- Five types of particles were identified based on visual appearance: (a) obvious fuel pieces; (b) cladding chunks; (c) foamy/porous, prior molten material; (d) particles that are a composite of fuel and prior molten material; and (e) metallic appearing, prior molten particles.

- Many of the particles examined contain regions of prior molten $(U\text{-}Zr)O_2$, indicating peak temperatures greater than 2800 K. Also, there are a few examples of prior molten material that are almost pure UO_2, indicating temperatures up to 3100 K.

- Several independently analyzed fuel-bearing particles contain oxygen concentrations in excess of 70 at.%. Such extensive fuel oxidation cannot readily be explained by fuel-steam reactions, and this evidence points strongly toward generation of free oxygen within the reactor vessel at some phase of the TMI-2 accident.

- The estimated average peak temperature for the debris bed is about 2200 K.

- Regions of prior molten U-Zr-O usually contain at least some trace of non-fuel rod material (Al, Cr, Fe, Ni). These elements often were found at grain boundaries or in voids. This indicates significant interaction between fuel rods and grid spacers, and possibly other stainless steel components.

- Control rod materials (Ag, In, Cd) were not as commonly found as structural materials. Ag, apparently had less of a tendency to mix or interact with fuel rod materials than did the structural materials.

- The presence of layered, prior molten particles indicates either a prolonged candling sequence or multiple temperature ramps occurred during the fuel liquefaction/relocation period of the accident.

- Evidence that molten metallic U and Zr flowed inside ballooned cladding was observed, as well as candling on the cladding outside surface.

- Significant Zr depletion (≤50%) has occurred in the majority of the debris samples analyzed, indicating significant relocation of Zr from the rubble bed.

- The majority of particles and aliquots examined contained a mixture of most core constitutents, indicating significant mixing and disruption of the original core.

- Concentrations of Ag-In-Cd (volatile core materials) generally show increases for the smaller particle size fractions and suggest that a vaporization/condensation transport mechanism may have been operable for these materials.

- Significant depletion of Ag (∿90%) from the core debris bed has occurred, suggesting possible transport to regions lower in the reactor vessel.

- wide distribution of the poison material, Gd, indicates that significant relocation of core materials has occurred.

- Al, a volatile core component, and Te are concentrated at the surface of the debris bed, suggesting that this portion of the bed may have functioned as a retention zone or trap for some vaporized material.

- Structural materials are well mixed in the debris bed at concentrations 30 to 50% of their original concentrations in the fueled region of a fuel assembly. The data indicate that both significant mixing of core constituents and little contamination of the debris with other structural components (end boxes, etc.) occurred.

- Significant amounts (70 to 80%) of all ^{137}Cs and ^{129}I has relocated from the debris bed.

- The ^{106}Ru, ^{125}Sb, ^{137}Cs, and ^{144}Ce at the E9 core location generally are at higher concentrations than at H8. The ^{137}Cs concentrations are 18 to 85% higher at E9.

- Portions of ^{106}Ru have left the fuel and have been retained in other materials (i.e., structural materials).

- ^{125}Sb has been significantly released from the fuel and has associated with non-fuel debris.

- ^{106}Ru and ^{125}Sb appear to have associated with Ni-containing materials, suggesting a retention mechanism for these radionuclides.

- ^{90}Sr appears to be almost completely retained in the fuel, with some leaching into the reactor coolant.

o Radionuclides were released from the fuel in the approximate order of volatility of the elemental constituents, except for ^{106}Ru and ^{90}Sr. ^{106}Ru release is higher and ^{90}Sr release is lower than expected, probably due to the formation of higher or lower volatile oxide forms.

o ^{144}Ce concentrations in the samples are higher than expected, based on the average core burnup. Some particles with little or no U content contain ^{144}Ce. These data suggest relocation of ^{144}Ce in the debris bed, possibly by formation of a volatile oxide.

o ^{129}I content in the debris tends to correlate with surface area in the small particle size fractions and, therefore, may suggest vaporization/condensation behavior for this radionuclide.

o Evidence of significant turbulent mixing of the liquefied core material has been observed.

o Segregation of Zr, Al, Ag, and Gd has been observed, suggesting that lower areas of the core may have different compositions than observed in the debris bed.

o ^{106}Ru and ^{125}Sb may have been transported to lower in the core and associated with liquefied Zr and structural material.

o There is no correlation between the enrichment of materials examined and the original (H8 and E9) fuel assembly enrichments, indicating significant physical relocation of the bulk core materials (fuel assemblies) has occurred.

6. REFERENCES

1. Quick Look Inspection: Report on the Insertion of a Camera into the TMI-2 Reactor Vessel Through a Leadscrew Opening, GEND-030, Vol. 1, March 1983.

2. Quick Look Inspection: Results, GEND-030, Vol. 2, April 1983.

3. G. O. Hayner, TMI-2 H8A Core Debris Sample Examination, GEND-INF-060, Vol. II, May 1985.

4. R. S. Wisner ltr to B. A. Cook, "HFEF Data Transmittal for S/A TMI-2," January 23, 1985.

5. J. Sanecki ltr to E. R. Carlson, "Shipment of Data Books Containing Results of SEM/EDX/Auger Examination of Particles of TMI Debris," February 22, 1985.

6. J. O. Carlson, TMI-2 Core Examination Plan, EGG-TMI-6169, July 1984.

7. V. F. Baston, TMI-2 Pyrophoricity Studies, GEND-043, November 1984.

8. J. R. Jewett, Thermal Analysis of TMI-2 Core Debris Samples, SD-WM-TRP-009, Rev. 0, Rockwell Handford Operations, October 10, 1984.

9. D. L. Hagrman et al., MATPRO-Version II (Revision 2) Handbook of Materials Properties for Use in the Analysis of Light Water Reactor Fuel Rod Behavior, NUREG/CR-0479, August 1981, p. 136.

10. R. Ruh and H. J. Garrett, "Non-Stoichiometry of ZrO_2 and Its Relation to Tetragonal-Cubic Inversion in ZrO_2," Journal of the American Ceramic Society, 50, 1966, pp. 257-261.

11. P. Hofmann and D. K. Kerwin-Peck, "Chemical Interactions of Solid and Liquid Zircaloy with UO_2 under Transient Nonoxidizing Conditions," International Meeting on LWR Severe Accident Evaluation, Cambridge, MA, August 28-September 1, 1983.

12. P. Hofmann and D. K. Kerwin-Peck, UO_2/Zry-4 Chemical Ineractions and Reaction Kinetics from 1000 to 1700°C Under Isothermal Conditions, KfK-3552, 1983.

13. P. Hofmann and D. K. Kerwin-Peck, "UO_2/Zry-4 Chemical Interactions from 1000 to 1700°C under Isothermal and Transient Temperature Conditions," Journal of Nuclear Materials, 124, 1984, pp. 80-105.

14. P. Hofmann and H. J. Neitzel, "External and Internal Reaction of Zry Tubing with Oxygen and UO_2 and Its Modeling," 5th International Meeting on Thermal Nuclear Reactor Safety, Karlsruhe, Germany, September 9-13, 1984.

15. W. Dienst, P. Hofmann, D. K. Kerwin-Peck, "Chemical Interactions between UO_2 and Zry-4 from 1000 to 2000°C," *Nuclear Technology, 65*, 1984, pp. 109-124.

16. P. Hofmann and C. Politis, "The Kinetics of the UO_2-Zry Reactions at High Temperatures," *Journal of Nuclear Materials, 87*, 1979, pp. 375-397.

17. P. Hofmann, "Transient Temperature UO_2/Zry-4 Interaction Experiments under Oxidizing Conditions up to about 2000°C," *The Annual Report of the Nuclear Safety Project (1984)*, KfK-3550, 1985, (to be published).

18. P. Hofmann et al., "Liquid Zry/Liquid UO_2 Interaction Experiments," *The Annual Report of the Nuclear Safety Project (1983)*, KfK-3450, 1984, pp. 4200/126-4200/154.

19. P. Hofmann, private communciation, KfK, Federal Repiblic of Germany, SFD Program Meeting, Idaho Falls, ID, April 16-19, 1985.

20. A. Skokan, "High Temperature Phase Relations in the U-Zr-O System," *Fifth International Meeting on Thermal Nuclear Reactor Safety, Karlsruhe, German Federal Republic*, August 1984.

21. R. S. Roth, T. Negas, and L. P. Cook, *Phase Diagrams for Ceramists, Volume IV*, The American Ceramic Society, 1981.

22. S. Hagen et al., "Phenomena and Material Behavior during Meltdown of PWR Fuel Rods," *Behavior of LWR Fuel Elements under Accident Conditions*, Spatind, Norway, September 1976.

23. R. R. Hobbins et al., "Light Water Reactor Debris from Severe In-Pile Transient Tests," *Nuclear Technology, Vol. 65*, April 1984.

24. N. Rasmussen et al., *Reactor Safety Study--An Assessment of Accident Risk in U.S. Commercial Nuclear Power Plants*, WASH-1400, NUREG-75/014, October 1975.

25. J. M. Broughton, private communication, EG&G Idaho, Inc..

26. K. J. Hofstetter and V. F. Baston, "TMI-2 Water Chemistry," *American Chemical Society Symposium--The TMI Accident Fission Product Release and Cleanup, April 28, 1985*.

27. B. G. Schnitzler and J. B. Briggs, *TMI-2 Isotopic Inventory Calculations*, EGG-PBS-6798, (to be published).

28. R. J. Davis et al., *Radionuclide Mass Balance for the TMI-2 Accident: Data through 1979 and Preliminary Assessment of Uncertainties*, GEND-INF-047, November 1984.

29. B. G. Schnitzler, private communication, EG&G Idaho, Inc.

30. D. W. Akers and D. A. Johnson, *TMI-2 Core Debris-Cesium Release/Settling Test*, GEND-INF-060, Vol. 3, December 1984.

31. B. Tolman, "Thermal Hydraulic Features of the TMI Accident," *American Chemical Society Symposium--The TMI Accident: Fission Product Release and Cleanup, April 28, 1985*.

32. L. S. Beller and H. L. Brown, *Design and Operation of the Core Topography Data Acquisition System for TMI-2*, GEND-INF-012, May 1984.

33. K. Vinjamuri et al., *Preliminary Report: Examination of H8 and B8 Leadscrew from TMI-2*, EGG-TMI-6685, April 1985.

34. C. Allison et al., *SCDAP/MOD1 Analysis of the Progression of Core Damage During the TMI-2 Accident*, SE-CMD-84-009, EG&G Idaho, Inc., June 1984.

35. D. J. Osetek et al., "Fission Product Behavior During the First Two PBF Severe Fuel Damage Tests," *Fission Product Behavior and Source Term Research Topical Meeting, July 15-19, 1984*.

36. *Analysis of Three Mile Island Unit 2 Accident*, NSAC-80-1 (NSAC-1 revised), March 1980.

37. R. P. Wichner and R. D. Spence, *Quantity and Nature of LWR Aerosols Produced in the Pressure Vessel during Core Heatup Accidents--A Chemical Equilibrium Estimate*, NUREG/CR-3181, March 1984.

38. C. V. McIsaac, *Surface Activity and Radiation Field Measurements of the TMI-2 Reactor Building Gross Decontamination Experiment*, GEND-037, October 1983.

39. D. Cubicciotti and B. Rajseghal "Vapor Transport of Fission Products in Postulated Severe Light Water Reactor Accidents," *Nuclear Technology, Vol. 65*, May 1984.

40. *Nuclear Power Plant Response to Severe Accidents*, Technology for Energy Corporation, November 1984.

41. *Technical Bases for Estimating Fission Product Behavior during LWR Accidents*, NUREG-0772, 1981.

42. A. W. Cronenberg, "An Assessment of Liquefaction-Induced I, Cs, and Te Release from Low and High Burnup Fuel," *1983 Meeting on Light-Water Reactor Severe Accident Evaluation, Cambridge Massachusetts, September 1983*.